Excited Beauty at L3

Een wetenschappelijke proeve op het gebied
van de Natuurwetenschappen, Wiskunde en Informatica.

Proefschrift

ter verkrijging van de graad van doctor
aan de Katholieke Universiteit Nijmegen,
volgens besluit van het College van Decanen
in het openbaar te verdedigen op
woensdag 29 september 1999,
des namiddags om 1.30 uur precies
door

Wilhelmina Cornelia van Hoek

geboren op 25 maart 1971 te Den Helder.

Promotor: Prof. Dr. E. W. Kittel

Co-promotor: Dr. Ir. D. J. Schotanus

Manuscripcomissie: Prof. Dr. P. Duinker (FOM Instituut SAF/NIKHEF)
Dr. W. J. Metzger
Dr. S. Goldfarb (University of Michigan)

The work described in this thesis is part of the research programme of the 'Nationaal Instituut voor Kernfysica en Hoge-Energie Fysica (NIKHEF)'. The author was financially supported by the 'Stichting voor Fundamenteel Onderzoek der Materie (FOM)'.

ISBN 90-9012890-5

Contents

Introduction

From the beginning of history, many people have wondered what everything that is observed in the world around us is made of. In the early days, the Greeks thought everything existed of only four elements: water, air, fire and earth. Throughout the centuries, the answer to the question changed in consequence of new discoveries and ideas in fields like chemistry and physics. Not only does the answer change through time, but it also depends on whom you are asking. Medical doctors like to believe it is all about strings of DNA and genes. For chemistry students it all boils down to atoms and electrons and nuclear physicists are only interested in protons and neutrons. And they all are right in their own way. Dissect DNA and genes and no life is possible; the atom (molecule) is the smallest piece of material that still carries the properties of that material and nuclear reactions take place by neutrons and protons. Who needs to know more? We (high energy physicists) do! We go to even smaller dimensions and believe everything is ultimately made of quarks, leptons and the forces acting between them.

As simple as this answer may seem, there is a lot more to particle physics. These elementary particles, as we call them, for instance, come in several flavours; 'up', 'down', 'charm', 'strange', 'top' and 'bottom' (or 'beauty') quarks, electrons, muons, taus and their neutrinos. All particles have anti-particles which are the same as the corresponding particles but have opposite charge (and other additive quantum numbers). There are four standard forces that act on these particles: the gravitational, strong, weak and electromagnetic forces. Interactions between particles take place through 'messengers': bosons. Each force is characterised by its own boson(s): the graviton, gluon, $W^{\pm}$ and Z^0, photon, respectively.

Quarks are confined and cannot be detected separately. They form hadrons, which can be classified as mesons and baryons (anti-baryons). Mesons are combinations of a quark and an anti-quark, baryons (anti-baryons) consist of three quarks (anti-quarks).

Quark and lepton physics is described in the so-called 'Standard' Model. However, there are quite a number of free parameters and gravitation is not included. Furthermore, although there is no need for any of the particles to have mass, we very well know from every-day experience that (most) particles are massive. There is a theory to overcome this problem. It is widely believed that the particle's interaction with the so-called Higgs field causes a particle to be massive. The Higgs particle corresponding to this field has not (yet) been discovered and its mass is one of the free parameters of the Standard Model.

High energy physicists 'have a dream' : All forces unite! Such a theory is called Grand Unification, describing the energy region where all forces act as one single force. The idea is that high-energy phenomena can be described in a simple way, but that symmetry breaking hides the simplicity of nature and makes it as complicated (and thus challenging) as it is now.

As difficult as some phenomena can get, they can sometimes be simplified by the use of (approximate) symmetries. One well-known symmetry is that of the u and d quarks (isospin symmetry), which arises since the mass difference is much smaller than the masses m_{u} and

m_d associated with quark confinement, set by the QCD scale Λ_QCD. Predictions based on this symmetry can be made by applying a so-called effective theory where the mass difference is set to zero. Corrections then come from an expansion in the (small) parameter $(m_\mathrm{u} - m_\mathrm{d})/\Lambda_\mathrm{QCD}$.

Another symmetry is that of the heavy quarks. This arises because the mass of a heavy quark Q is much larger than Λ_QCD. Predictions come from a heavy-quark effective theory where the mass of the heavy quark is set to infinity. Corrections are obtained from an expansion in terms of $\Lambda_\mathrm{QCD}/m_\mathrm{Q}$. Light quarks interacting with such a heavy quark are blind to the heavy-quark flavour/mass and spin. Therefore, the excitation spectrum for any system containing a heavy quark and light quarks will be the same. This fact can be used to derive predictions for a heavy-quark system by extrapolating results obtained for another heavy-quark system. Each spectral level can be characterised by the light-quark quantum numbers: $\vec{j}_\mathrm{q} = \vec{s}_\mathrm{q} + \vec{L}$, were $\vec{s}_\mathrm{q}$ is the spin of the light quark, $\vec{L}$ is the orbital momentum of the system and $\vec{j}_\mathrm{q}$ is the total angular momentum of the light quark. Each level is a degenerate doublet in total angular momentum: $J_\pm = j_\mathrm{q} \pm s_\mathrm{Q}$, where $J_\pm$ is the total spin of the system and s_Q is the spin of the heavy quark. The orbitally excited (L=1) beauty mesons ($\mathrm{B}^{**}_{\mathrm{u,d}}$), the main subject of this thesis, can thus be indicated by $j_\mathrm{q} = 1/2$ (J_+ = 1 and J_- = 0) and $j_\mathrm{q} = 3/2$ (J_+ = 2 and J_- = 1). They decay strongly into a $\mathrm{B}_{\mathrm{u,d}}$ or B^* meson and a pion. The pion can be either charged or neutral. Since both channels are measured in this analysis, the isospin symmetry can be checked.

First, the heavy-quark symmetry and effective theory will be discussed in chapter 1. This will be followed by a description of the theoretical predictions and existing experimental results on excited B mesons. In chapter 2, the experimental setup is described. Special attention is paid to the Silicon Microvertex Detector, which is of great importance for the analysis described in this thesis. In the third chapter, the tools for obtaining the direction and the energy of the B meson and the criteria for the selection of charged and neutral pions are described. In the fourth chapter, the $\mathrm{B}\pi^\pm$ and $\mathrm{B}\pi^0$ mass distributions are obtained and fitted, and the relative production rates are compared. As a completion of the excited beauty states, the analysis is repeated for B^* decays to $\mathrm{B}\gamma$ at the end of the chapter. The systematic errors are described in chapter 5. Chapter 6 follows with the conclusions and a comparison to the results of other experiments.

Chapter 1

Theory

All present knowledge of the fundamental world of particles is, except for gravity, incorporated in the so-called Standard Model. Due to symmetries for particles consisting of a heavy quark and a light quark, which are exact in the limit of infinite mass of the heavy quark, an effective theory exists within the Standard Model: The Heavy-Quark Effective Theory (HQET) [1] with which this thesis is concerned. This chapter begins with a short outline of the Standard Model. This is followed by a description of the symmetry and the effective theory of heavy-quark physics. After that, the theoretical predictions and existing experimental results on the $\mathrm{B}^{**}_{\mathrm{u,d}}$ will be discussed. In the last section, the theoretical predictions and experimental results on the B^* are summarised.

1.1 The Standard Model

According to the Standard Model of particle physics, all the matter our world is made of consists of quarks and leptons. Both types of particles have spin-$\frac{1}{2}$ and are called fermions. They can be divided into three groups or families. The first family consists of the 'up' and 'down' quarks, the electron and the electron neutrino; the second family of the 'charm' and 'strange' quarks and the muon and muon neutrino; and the last family consists of the 'top' and 'bottom' (or 'beauty') quarks and the tau and tau neutrino.

The six quarks and at least three of the leptons carry mass[1]. The six quark masses and the three lepton masses are parameters in the Standard Model. The masses of the electron, muon and tau are well measured. The quark masses are not well known since quarks are confined, i.e., they can not be detected as single particles, but always combine to form mesons ($\mathrm{q\overline{q}}$) or baryons (qqq). The masses are assumed to be in the range of 1.5-5 MeV for a u quark, 3-9 MeV for a d quark and 60-170 MeV for an s quark. From the mass of the mesons that contain a c or b quark one estimates a mass of 1.1-1.4 GeV for a c quark and 4.1-4.4 GeV for a b quark [4]. In recent measurements at Fermilab [5, 6], the mass of the top quark was found to be (173.8 ± 5.2) GeV, compatible with predictions using LEP precision electroweak data [7].

The particles which intermediate the forces of interaction between fermions are spin-1 particles, called bosons. There are four known forces, but only three of them are incorporated

[1] The masses of the other three leptons (neutrinos) were always assumed to be zero, but recent results from the Super-Kamiokande collaboration [2, 3] indicate an atmospheric neutrino flux ratio which is not one and depends on the zenith angle. This hints to neutrino oscillations, which are possible only if at least one of the neutrinos is not massless.

into the Standard Model. These are the strong, weak and electromagnetic interactions. Each interaction has its own mediator boson(s): gluon, Z^0 and $W^{\pm}$, and photon respectively. Each force interacts with its own strength and these so-called coupling constants are parameters of the Standard Model.

The so-called Higgs mechanism accounts for the masses of particles via spontaneous symmetry breaking, i.e., all massive particles obtain their mass by interaction with the Higgs field. The Higgs mass and the vacuum expectation value of the Higgs boson are further parameters.

The property distinguishing the six quarks is called flavour. The weak interaction does not conserve flavour. Therefore, the weak eigenstates of quarks are not the individual flavour states, but a mixture of those. By convention, the d, s, and b quarks, rather than the u, c and t quarks, are chosen to be mixed. The mixing is described in the Cabibbo-Kobayashi-Maskawa (CKM) matrix [8]:

$$\begin{pmatrix} d' \\ s' \\ b' \end{pmatrix} = \begin{pmatrix} V_{\mathrm{ud}} & V_{\mathrm{us}} & V_{\mathrm{ub}} \\ V_{\mathrm{cd}} & V_{\mathrm{cs}} & V_{\mathrm{cb}} \\ V_{\mathrm{td}} & V_{\mathrm{ts}} & V_{\mathrm{tb}} \end{pmatrix} \begin{pmatrix} d \\ s \\ b \end{pmatrix}$$
$$= \begin{pmatrix} c_1 & -s_1c_3 & -s_1s_3 \\ s_1c_2 & c_1c_2c_3 - s_2s_3e^{i\delta} & c_1c_2s_3 + s_2c_3e^{i\delta} \\ s_1s_2 & c_1s_2c_3 + c_2s_3e^{i\delta} & c_1s_2s_3 - c_2s_3e^{i\delta} \end{pmatrix} \begin{pmatrix} d \\ s \\ b \end{pmatrix}.$$

Here, c_i and s_i are abbreviations of $\cos\theta_i$ and $\sin\theta_i$, respectively. The three mixing angles θ_i and the overall phase δ are again parameters of the Standard Model.

The Lagrangian formalism describes the dynamics of the interactions. From the Lagrangian, so-called Feynman rules are derived. These are used to calculate measurable quantities like interaction cross sections, particle lifetimes and other quantities in perturbation theory. In figure 1.1 a few of these rules are indicated, particularly those of importance for heavy quarks (see section 1.3 below).

The quark of interest for this thesis is the beauty or bottom quark. This is one of the so-called heavy-flavour quarks. The symmetry and the effective theory that describe heavy-quark physics is described in the next sections.

1.2 Symmetries in QCD and heavy quark symmetry

There are several review articles written about HQS (Heavy Quark Symmetry), as references [9–13] testify. A summary is given here. It is very difficult to make predictions in the theory of the strong interactions called Quantum Chromo Dynamics (QCD) based on analytical calculations. However, the existence of symmetries makes it possible to approximate certain physical quantities. A well-known symmetry is isospin symmetry. It arises since the mass difference of the light quarks $m_{\mathrm{d}} - m_{\mathrm{u}}$ is much smaller than the masses associated with confinement, set by the QCD scale Λ_{QCD}. Predictions based on isospin symmetry would be exact in the limit $m_{\mathrm{d}} - m_{\mathrm{u}} \to 0$. In the real world this mass difference is not zero. To correct for this fact, an expansion in the small parameter $(m_{\mathrm{d}} - m_{\mathrm{u}})/\Lambda_{\mathrm{QCD}}$ and the electromagnetic coupling constant α can be made. When the s quark is included, the SU(3) flavour symmetry is obtained, but the corrections are larger since $(m_{\mathrm{s}} - m_{\mathrm{d}})/\Lambda_{\mathrm{QCD}}$ is not as small.

Another well known symmetry is chiral symmetry $\mathrm{SU}(2)_{\mathrm{L}} \times \mathrm{SU}(2)_{\mathrm{R}}$ which arises in QCD because the masses of the u and d quark m_{d} and m_{u}, themselves, are small compared to Λ_{QCD}.

Due to chiral symmetry, the vector and axial vector currents are separately conserved. The chiral symmetry group can be enlarged to $SU(3)_L \times SU(3)_R$ if also the mass of the s quark is treated as small compared with the QCD scale.

In the case of a light quark q, the complicated equations of motion can be simplified by applying an effective theory where the quark mass is set to zero. This works well as long as the real light-quark mass is small enough in comparison to the QCD scale that it scarcely influences the dynamics of the strong interactions. The small quark mass can be considered as a perturbation and the expansion in the perturbation term m_q/Λ_{QCD} gives corrections on the predictions of the effective theory.

A new symmetry has come into the picture with the discovery of heavy quarks Q. In contrast to the symmetries of the light quarks mentioned above, this symmetry arises when the mass of a quark m_Q is much larger than the scale Λ_{QCD}. A heavy quark is surrounded by a hadronic 'sea' of light quarks and gluons often referred to as the light constituents or light degrees of freedom of the hadronic system, but the heavy quark will hardly notice this. Its motion will fluctuate only slightly about that of a free heavy quark and the heavy quark therefore defines its own centre of mass. On the other hand, the light quarks and gluons around it will not notice anything if the heavy quark is replaced by another sufficiently heavy quark with a different mass.

We can feel this intuitively, but what is the theory behind it? The size of the hadronic system is determined by the hadron radius, $R_{had} \sim \frac{1}{\Lambda_{QCD}} \sim 1$ fm. The exchange of momentum between the heavy and light quarks is of order Λ_{QCD}. The soft gluons exchanged can only probe distances larger than the Compton wavelength λ_Q ($\lambda_Q << R_{had}$). So the quantum numbers of the heavy quark (flavour (mass) and spin) remain hidden for the light quark. For example, the excitation spectra will be the same for any heavy-quark hadron.

The fact that the mass of the heavy quark m_Q is irrelevant can be seen as follows. The hadron and the heavy quark have (approximately) the same velocity, so in the rest frame of the hadron the heavy quark is also at rest. The wave function of the light quark is a solution of the QCD equation of motion with the boundary condition that a static source of colour has been placed at the position of the heavy quark. Since the mass does not enter the boundary condition, also the solutions do not depend on the heavy quark mass[2]. This leads to an SU(N) symmetry, with N the number of heavy quarks.

The fact that the heavy-quark spin is decoupled leads to an SU($2N$) symmetry. This means, for instance, that every spectral level consists of a degenerate doublet with total spin $J_\pm = j_q \pm s_Q$, where j_q is the total angular momentum of the light quark and s_Q is the spin of the heavy quark[3]. From the above, it follows that in the limit $m_Q \rightarrow \infty$ the configuration of the spectral levels is the same for heavy quarks that only differ in spin or flavour. This provides us with relations between the properties of the heavy mesons and baryons containing a c quark, D, D^*, D^{**} and Λ_c, on the one hand, and the corresponding ones containing a b quark, B,B^*, B^{**} and Λ_b, on the other. Here the single asterisk indicates the excited state with $L = 0$ ($J_+ = 1$) and the double asterisk indicates the orbitally excited states with $L = 1$ ($J_\pm = 0, 1, 2$).

As in the case of the light-quark system mentioned above, one can adopt an effective theory: Heavy Quark Effective Theory (HQET). However, here the quark mass is not set to zero, but it approaches infinity. This effective theory and its implications will be further

[2]The heavy-quark flavour symmetry is analogous to the fact that the different isotopes of the same element have the same chemistry

[3]The spin symmetry is analogous to the fact that the hyperfine levels in atoms are (nearly) degenerate

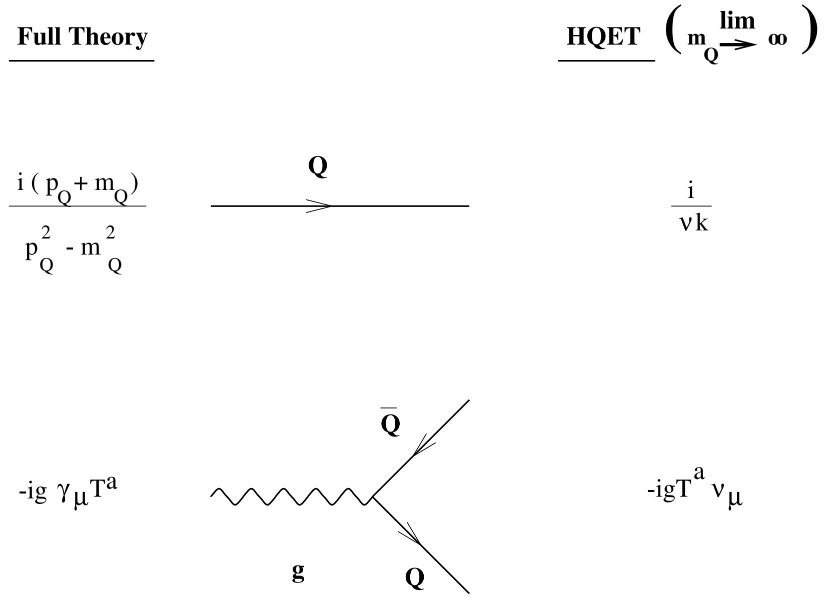

Figure 1.1: *Feynman rules that play a role for heavy quark physics: the quark propagator and the quark-gluon interaction, at the left for the full theory and at the right for HQET.*

discussed in the next section.

One should note that the $\mathrm{SU}(2N)$ spin-flavour symmetry of HQET is not manifest in the full theory of QCD. The HQET is a good approximation of QCD in a certain kinematic region and then only for systems in which the heavy quark interacts predominantly by the exchange of soft gluons.

As in the case of chiral symmetry, it is possible for approximate heavy-quark spin-flavour symmetry to treat the perturbation terms in $\Lambda_{\mathrm{QCD}}/m_{\mathrm{Q}}$ as corrections to the predictions based on the effective heavy-quark theory.

1.3 Heavy-Quark Effective Theory (HQET)

The HQET is treated in [1] and several lectures [10, 14–18] in great detail. I will summarise it briefly in this section. The Feynman rules for HQET can be derived in two ways. One can derive them from the Feynman rules of the full theory by taking the quark mass to infinity while keeping the velocity ν^μ fixed. The rules for the full QCD propagator and quark-gluon interaction are given in figure 1.1. The momentum of the heavy quark can be written as: $P_{\mathrm{Q}}^\mu = m_{\mathrm{Q}}\nu^\mu + k^\mu$, with k^μ being a residual momentum small compared to m_{Q}. The propagator in the effective theory is then given by: $\frac{i}{\nu \cdot k}$ and the vertex of the heavy-quark gluon interaction by $-igT^a\nu_\mu$ [1].

The same result can be obtained from that part of the Lagrangian density that describes the heavy-quark field:

$$\mathcal{L} = \bar{Q}(i\not{D} - m_{\mathrm{Q}})Q \tag{1.1}$$

with $Q = e^{-im_Q v\cdot x}h_v^{(Q)}$, where $h_v^{(Q)}$ is the heavy-quark field which satisfies $\not{v}h_v^{(Q)} = h_v^{(Q)}$ and $\not{D} = \gamma^\mu \delta_\mu + igT^a A_\mu^a$. For a quark with velocity v, in the limit $m_Q \to \infty$ the Lagrangian density becomes [1]:

$$\mathcal{L}_\infty = \bar{h}_v^{(Q)} iv \cdot Dh_v^{(Q)}. \tag{1.2}$$

This effective Lagrangian density also reproduces the Feynman rules of the HQET. The equation of motion is then given by: $v \cdot Dh_v^{(Q)} = 0$.

The field $h_v^{(Q)}$ destroys a heavy quark of four-velocity v, but it does not create an antiquark. So, since pair production is not present in the effective theory, the field of the antiquark is an independent degree of freedom. This is a U(1) symmetry of the effective Lagrangian that results in the conservation of the heavy quarks and is not present in the Lagrangian of the full theory.

Since no Dirac matrices appear in the Lagrangian density, interactions of a heavy quark with gluons leave its spin unchanged. Also the mass of the heavy quark is not in the Lagrangian density. So, for N heavy-quark flavours with corresponding fields $h_v^{(j)}$ for the j^{th} heavy quark, the Lagrangian density becomes:

$$\mathcal{L}_\infty = \sum_{j=1}^{N} \bar{h}_v^{(j)} iv \cdot Dh_v^{(j)}. \tag{1.3}$$

This Lagrangian density is invariant under rotations in flavour space. This is an $\mathrm{SU}(2N)$ spin-flavour symmetry.

Only effects that survive in the limit $m_Q \to \infty$ are illustrated here. First order corrections can be expressed in terms of $\Lambda_{\mathrm{QCD}}/m_Q$. Furthermore, a field $H_v^{(Q)}$ creating a heavy quark of velocity v can be added to the description. This occurs since the heavy quark is not precisely on shell as it propagates. It is approximately on shell, however, so that $H_v^{(Q)}$ is small compared to $h_v^{(Q)}$. The field $H_v^{(Q)}$ can be written in terms of $h_v^{(Q)}$ and the effective Lagrangian density is thus given by [1]:

$$\mathcal{L}_{\text{eff}} = \bar{h}_v^{(Q)} iv \cdot Dh_v^{(Q)} + \frac{\bar{h}_v^{(Q)}}{2m_Q}[(iD)^2 - \frac{1}{2}g\sigma_{\mu\nu}G^{a\mu\nu}T^a]h_v^{(Q)} \tag{1.4}$$

with $G^{a\mu\nu}$ the gluon field strength tensor. The last term describes the coupling of the heavy-quark spin to the gluon field. It is the last term in the above equation that violates the heavy-quark spin symmetry and it is the matrix element of this term that gives rise to the $P_Q^* - P_Q$ mass difference, where P_Q^* and P_Q are of the same degenerate doublet, with P_Q^* being the J_+ state and P_Q the J_- state.

1.4 Examples of HQET in spectroscopy

In spectroscopy, the spin-flavour symmetry leads to relations between the properties of hadrons that contain a heavy quark that differs only in spin or flavour. As described in the previous sections, the dynamics of hadronic states is independent of the spin and mass of the heavy quark and can thus be classified by the quantum numbers (for example the total spin) of the light degrees of freedom. For fixed $j_q \neq 0$, there is a doublet of degenerate states with total spin $J_\pm = j_q \pm \frac{1}{2}$.

The mass of a hadron containing a heavy quark Q can be written as:

$$m_H = m_Q + \bar{\Lambda} + \frac{\Delta m^2}{2m_Q} + O(1/m_Q^2), \tag{1.5}$$

where the parameter $\bar{\Lambda}$ arises from the part of the Lagrangian that is independent of the heavy quark mass [19] and the quantity Δm^2 can be parametrised as follows [20] :

$$\Delta m^2 = -\lambda_1 + 2\left[J(J+1) - \frac{3}{2}\right]\lambda_2, \tag{1.6}$$

where J is the total spin of the meson. The first term divided by $2m_Q$ arises from the kinetic energy of the heavy quark inside the meson. The second term describes the interaction of the heavy-quark spin with the gluon field. The hadronic parameters $\bar{\Lambda}$, λ_1 and λ_2 are independent of m_Q.

First, we give an example where HQET provides a accurate prediction with no need for corrections. The theory predicts for the mass splittings between the two members of the spin doublet with $j_q = 1/2$:

$$\begin{aligned} \Delta_B &= m_{B^*}^2 - m_B^2 = 4\lambda_2 + O(1/m_b), \\ \Delta_D &= m_{D^*}^2 - m_D^2 = 4\lambda_2 + O(1/m_c), \end{aligned} \tag{1.7}$$

so that $m_{B^*}^2 - m_B^2 \simeq m_{D^*}^2 - m_D^2$. The values obtained from the data [4] of (0.49 $\pm$ 0.03) GeV^2 and (0.545 $\pm$ 0.003) GeV^2 for Δ_B and Δ_D, respectively, are compatible with this prediction.

On the other hand, the mass splitting between the ground-state mesons and baryons containing a heavy quark serves as an example where corrections can no longer be ignored. The HQET predicts:

$$\begin{aligned} \Delta_b &= m_{\Lambda_b} - m_B = \bar{\Lambda}_{baryon} - \bar{\Lambda}_{meson} + O(1/m_b), \\ \Delta_c &= m_{\Lambda_c} - m_D = \bar{\Lambda}_{baryon} - \bar{\Lambda}_{meson} + O(1/m_c), \end{aligned} \tag{1.8}$$

and that these two mass splittings should be similar. The values obtained from the data [4] of (345 $\pm$ 9) MeV and (415.6 $\pm$ 0.6) MeV for Δ_b and Δ_c, respectively, are not compatible with the theoretical predictions. In this case, sizable corrections are needed by a term $3\lambda_2/2m_Q$ on the right hand side [10]. After this term is included, a value of (311 $\pm$ 9) MeV and (320 $\pm$ 1) MeV is obtained for Δ_b and Δ_c, respectively. So both mass splittings are indeed the same after these corrections .

After introducing the spin-averaged meson masses $\bar{m}_B = \frac{1}{4}(m_B + 3m_{B^*}) \simeq 5.31$ GeV and $\bar{m}_D = \frac{1}{4}(m_D + 3m_{D^*}) \simeq 1.97$ GeV, the difference between the two heavy b and c quarks, can be calculated with the use of equation (1.5):

$$m_b - m_c = (\bar{m}_B - \bar{m}_D)\left\{1 - \frac{\lambda_1}{2\bar{m}_B}\bar{m}_D + O(1/m_Q^3)\right\}, \tag{1.9}$$

where $O(1/m_Q^3)$ is used as a generic notation representing terms suppressed by three powers of the b or c quark masses. A theoretical estimate for the parameter λ_1 is: $\lambda_1 = 0.3 \pm 0.2$ [21–23]. This leads to

$$m_b - m_c = (3.39 \pm 0.03 \pm 0.03)\ \text{GeV}, \tag{1.10}$$

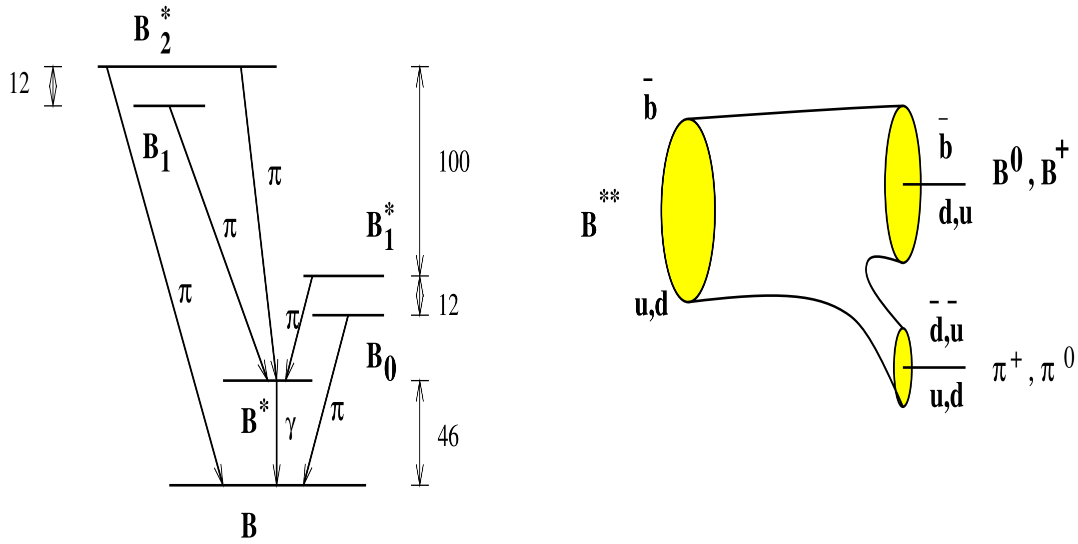

Figure 1.2: *Modes of the decay of B^{**}_{ud} to $B\pi$ and $B^*\pi$, where the mass splittings indicated are given in MeV (a) and the diagram of the corresponding strong interaction (b).*

where the first error is due to the uncertainty in the value of λ_1, and the second one estimates the unknown higher-order corrections. So, although, the separate quark masses are not well known, it is possible to calculate the quark mass difference very accurately with the help of HQET.

1.5 The orbitally excited *L*=1 beauty states

Identification of the charge of the pion (or kaon) resulting from the strong decay of an excited beauty meson could possibly serve as a tag of the initial flavour of the neutral B meson in CP-violation studies [24]. The statistics of data taken by the LEP experiments, however, is not high enough for such studies. Future experiments at Fermilab and LHC will be able to possibly make these measurements.

This thesis is concerned rather with the study of the spectroscopy of the orbitally excited states, a source of valuable information on the quark model and as a means to distinguish between different theoretical predictions.

1.5.1 Predictions for orbitally excited heavy-quark states and $\mathrm{B}^{**}_{\mathrm{u,d}}$

The flavour symmetry of HQET can be used to make predictions for the excited beauty system from results already obtained in the excited charm and even strange systems. For heavy mesons, the degenerate pairs of states are characterised by the total angular momentum of the light degrees of freedom, $j_\mathrm{q} = L \pm \frac{1}{2}$, and each state of a degenerate pair is indicated by the total spin of the meson, $\vec{J} = \vec{j}_\mathrm{q} + \vec{s}_\mathrm{Q}$. In the case of excited (*L*=1) heavy mesons these are $j_\mathrm{q} = \frac{1}{2}$ (with total spin *J*=0,1, respectively) and $j_\mathrm{q} = \frac{3}{2}$ (with total spin *J*=1,2, respectively).

The different excited L=1 states in the beauty system are labelled B_0 and B_1^* for the $j_\mathrm{q} = \frac{1}{2}$ states and B_1 and B_2^* for $j_\mathrm{q} = \frac{3}{2}$, where the state indicated by a asterisk is always the higher lying one of the doublet and the subscript is the total spin of the excited meson (see figure 1.2). $\mathrm{B}_{\mathrm{u,d}}^{**}$ is the generic name for those four excited states.

The mass of a heavy-light quark meson can be written as [25, 26]:

$$M(L(j_\mathrm{q})) = M(1\mathrm{S}) + E(L(j_\mathrm{q})) + \frac{C(L(j_\mathrm{q}))}{m_\mathrm{Q}}, \tag{1.11}$$

with $M(1\mathrm{S})$ the spin-averaged mass of the ground state as described in the previous section, $E(L(j_\mathrm{q}))$ the excitation energy and $C(L(j_\mathrm{q}))$ incorporates the higher-order contributions. For the $j_\mathrm{q} = \frac{3}{2}$ states, the above equation gives for the excited strange and charmed mesons:

$$\mathrm{K}^{**}: \qquad \begin{cases} M(\mathrm{P}_2)_\mathrm{K} - M(1\mathrm{S})_\mathrm{K} = & E(\mathrm{P})_\mathrm{K} + \frac{C(\mathrm{P}_2)}{m_\mathrm{s}} \\ M(\mathrm{P}_1)_\mathrm{K} - M(1\mathrm{S})_\mathrm{K} = & E(\mathrm{P})_\mathrm{K} + \frac{C(\mathrm{P}_1)}{m_\mathrm{s}} \end{cases}$$

$$\mathrm{D}^{**}: \qquad \begin{cases} M(\mathrm{P}_2)_\mathrm{D} - M(1\mathrm{S})_\mathrm{D} = & E(\mathrm{P})_\mathrm{D} + \frac{C(\mathrm{P}_2)}{m_\mathrm{c}} \\ M(\mathrm{P}_1)_\mathrm{D} - M(1\mathrm{S})_\mathrm{D} = & E(\mathrm{P})_\mathrm{D} + \frac{C(\mathrm{P}_1)}{m_\mathrm{c}} \end{cases}$$

with $E(\mathrm{P})_\mathrm{D} = E(\mathrm{P})_\mathrm{K} - \delta$ and $\delta = 32$ MeV [25,26]. Using the experimental results for observed P-wave charm and strange mesons, one can extrapolate to obtain predictions for the P-wave beauty mesons for the $j_\mathrm{q} = \frac{3}{2}$ states of 5.767 GeV and 5.755 GeV for the B_2^* and B_1 states, respectively.

Since $\mathrm{P}(\frac{1}{2})_\mathrm{D}$ mesons have not yet been observed, this method cannot be used (yet) to predict the masses of the $j_\mathrm{q} = \frac{1}{2}$ $\mathrm{B}_{\mathrm{u,d}}^{**}$ states. In reference [27] the mass difference between the two doublets is estimated to be of the order of 100 MeV. The mass splittings predicted between the $\mathrm{B}_{\mathrm{u,d}}^{**}$ states are indicated in figure 1.2(a) [4].

The decays of $\mathrm{B}_{\mathrm{u,d}}^{**}$ are given in figure 1.2 (b). Combining chiral and heavy-quark symmetry suggests that $j_\mathrm{q} = \frac{1}{2}$ P-wave states should have large widths for pionic decay to the ground states since they can decay via S-waves. Mixing of the narrow $\mathrm{P}(\frac{3}{2})$ level with the broader $\mathrm{P}(\frac{1}{2})$ state is predicted to be negligible. This is suggested by the fact that the narrow width observed for the $D_{\mathrm{s}1}$ is consistent with the prediction from HQET [13]. This should also hold for $\mathrm{B_s}$ and B. The B_2^* and B_1 states can only decay via a D-wave and are therefore narrow. The predicted width for $\mathrm{B}^{**} \to \mathrm{B}^{(*)}\pi$ is 11 MeV for the B_2^* state to $\mathrm{B}^*\pi$, 11 MeV for the B_2^* state to $\mathrm{B}\pi$ and 17 MeV for the B_1^* state to $\mathrm{B}^*\pi$. The total decay width amounts to 25 MeV for the $J^P = 2^+$ state and 21 MeV for the 1^+ state [25].

The relative production rates of the four $\mathrm{B}_{\mathrm{u,d}}^{**}$ states are not predicted by HQET, but a reasonable assumption is spin counting , $2J+1$ with J the total spin of the heavy hadron. This method results in the ratio 5:3:3:1 for $\mathrm{B}_2^* : \mathrm{B}_1 : \mathrm{B}_1^* : \mathrm{B}_0$. The measured production ratio $\frac{BR(b \to B^*)}{BR(b \to B^{(*)})}$ of about 0.75 supports this assumption.

[4] There are recent theoretical predictions [28, 29] that argue that the $j_\mathrm{q} = 1/2$ multiplet should lie above the $j_\mathrm{q} = 3/2$ multiplet due to mass and relativistic corrections. Unfortunately, at present no experimental results exist that can single out one of these different alternatives.

1.5.2 Experimental results on the $B^{**}_{u,d}$ meson

Evidence of P-wave charm mesons has been found by CLEO [30, 31] and ARGUS [32–34] and more recently DELPHI [35] and ALEPH [36] have shown their results. From consistency arguments, it was expected that resonances like those in the D system would also exist in the beauty system. DELPHI [37] and OPAL [38], and later ALEPH [39, 40], have shown that a resonance does indeed occur in the charged-pion channel, although broader than expected. The experimental results of the three LEP experiments are summarised in table 1.1. The most recent result from ALEPH [40] is obtained by using fully reconstructed B decays. In that paper the mass of the B^*_2 resonance state is obtained by performing a fit to the mass spectrum which fixes the mass differences, widths and relative rates of all spin states according to one particular model. The masses of all other states can be calculated via their mass splittings.

With the installation of the L3 Silicon Microvertex Detector and subsequently better impact parameter resolution and enhanced b-tagging capability, an analysis of $B^{**}_{u,d}$ has also become possible in L3. Firstly, the charged-pion decay of the $B^{**}_{u,d}$ is analysed. The L3 detector, which has a high resolution electromagnetic calorimeter, allows in addition for the first time the analysis of the neutral-pion decay channel. This provides the important check of the assumed isospin symmetry.

experiment	$\overline{M}$(GeV)	$M_{B^*_2}$ (GeV)	Γ(MeV)	Br (%)	σ(MeV)	$N_{B^{**}_{u,d}}$
DELPHI [37]	5.732 $\pm$ 0.005 $\pm$ 0.020		145 $\pm$ 28	27 $\pm$ 6 $\pm$ 6	79 $\pm$ 8 $\pm$ 8	2157 $\pm$ 120 $\pm$ 323
OPAL [38]	5.681 $\pm$ 0.011		116 $\pm$ 24	18 $\pm$ 4		738 $\pm$ 121
ALEPH [39]	5.703 $\pm$ 0.004 $\pm$ 0.010			27.9 $\pm$ 1.6 $\pm$ 5.9	53 $\pm$ 3 $\pm$ 9	1944 $\pm$ 108 $\pm$ 161
ALEPH [40]		5.739 +8 -11 +6 -4		31 $\pm$ 9 +6 -5		
CDF [41]	5.71 $\pm$ 0.02			28 $\pm$ 0.06 $\pm$ 0.03		

Table 1.1: *Experimental results on $B^{**}_{u,d}$. $\overline{M}$ is the average $B^{**}_{u,d}$ mass, $M_{B^*_2}$ is the mass of the B^*_2 orbitally excited state, Γ the Breit-Wigner width of the signal, Br the production rate, σ the Gaussian width of the signal and $N_{B^{**}_{u,d}}$ the number of $B^{**}_{u,d}$ in the signal*

1.5.3 Experimental results on the B^* meson

The B^* is the well-established vector partner of the pseudoscalar $\mathrm{B_{ud}}$. Due to the small mass difference all strong decays of B^* are forbidden, implying a branching ratio for the electromagnetic $\mathrm{B}^* \to \mathrm{B}\gamma$ decay close to 100 %. The relative production rate, $N_{\mathrm{B}^*}/(N_{\mathrm{B}^*} + N_{\mathrm{B}})$, is a measurement of: $V/(V+P)$, the fraction of vector meson production to the sum of vector and pseudoscalar production. Spin counting predicts: $V/(V+P) \sim 0.75$. The production and decay of orbitally excited B mesons ($\mathrm{B}^{**}_{\mathrm{u,d}}$) to B or B^* mesons may modify the measurements somewhat. Also phase-space effects arising from the mass difference between the vector and pseudoscalar states can alter the prediction. In the charm sector a value much lower than 0.75 of about 0.5 [42] is found. This low value is not well understood. The experimental results for the B^* signal are summarised in table 1.2.

experiment	Br (%)	Q(MeV)	N_{B^*}
CUSB [43]	- - -	45.4 $\pm$ 1.0 -	- - -
CLEO [44]	- - -	46.2 $\pm$ 0.3 $\pm$ 0.8	- - -
DELPHI [45]	72 $\pm$ 3 $\pm$ 6	45.5 $\pm$ 0.3 $\pm$ 0.8	3009 $\pm$ 108 $\pm$ 65
OPAL [46]	76.0 $\pm$ 3.6 $\pm$ 8.3	46.2 $\pm$ 0.3 $\pm$ 0.8	1894 $\pm$ 89 -
ALEPH [47]	77.1 $\pm$ 2.6 $\pm$ 7.0	45.30 $\pm$ 0.35 $\pm$ 0.87	4227 $\pm$ 140 $\pm$ 252
L3 [48,49]	76 $\pm$ 4 $\pm$ 6	46.3 $\pm$ 1.9 -	1378 $\pm$ 145 -

Table 1.2: *Experimental results on* B^*. *Br is the production rate, Q is the* $\mathrm{B}^* - B$ *mass difference and* N_{B^*} *is the number of* B^* *in the signal.*

Chapter 2

The Detector

Near Geneva (Switzerland) is situated one of the world largest accelerator centres: CERN. Several accelerators were built here, the largest of which is the Large Electron Positron collider LEP. It was decided that LEP would operate in two phases. In the first phase (LEP-I) it accelerated electrons and positrons up to about 46 GeV in opposite direction, providing the centre-of-mass energies needed to cover the Z resonance region. During the LEP-I phase the Standard Model parameters connected to the Z boson were measured with high accuracy. In the second phase (LEP-II) it accelerates electrons and positrons up to about 100 GeV, providing a centre-of-mass energy of about 200 GeV. During the LEP-II phase measurements are being performed at the W pair production and a possibility exists to discover the Higgs particle.

LEP is installed in a 26.7 km long tunnel down to about 100 m under the surface near the French-Swiss border. It consists of eight straight sections and eight curved ones. Four of the straight sections are housing large particle detectors: ALEPH, OPAL, DELPHI and L3, of which the L3 detector is the one used for this analysis. This detector is briefly described in the next section with the exception of the Silicon Micro-vertex Detector (SMD), which is described in greater detail in section 2.2. The simulation of the behaviour of particles in the L3 detector is briefly described in section 2.3.

2.1 The L3 detector

In figure 2.2 a perspective view of the L3 detector is shown. The origin, i.e., the point where the particles collide, is at the centre of the detector. The x-axis is towards the centre of the LEP ring, the y-axis is directed upwards and the z-axis is directed parallel to the beam pipe pointing in the direction of flight of the electron beam. In this analysis often the spherical coordinates r, θ, ϕ, will be used, were r is the distance to the centre of the detector, θ the angle between the z-axis and the $\vec{r}$ vector and ϕ the angle between the x-axis and the projection $\vec{s}$ of $\vec{r}$ on the xy-plane.

The L3 detector consists of several subdetectors each having its special characteristics and particular purpose. The whole detector is placed inside a large ($12 \times 12 \times 12$ m^3) magnet which provides a uniform magnetic field of 0.5 T.

The innermost part of the detector takes care of the tracking of charged particles. It is also

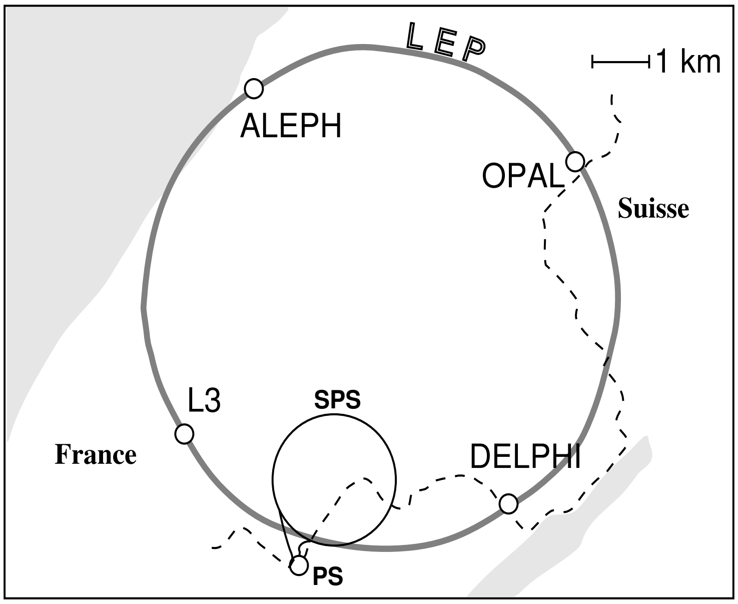

Figure 2.1: *The* LEP *ring.*

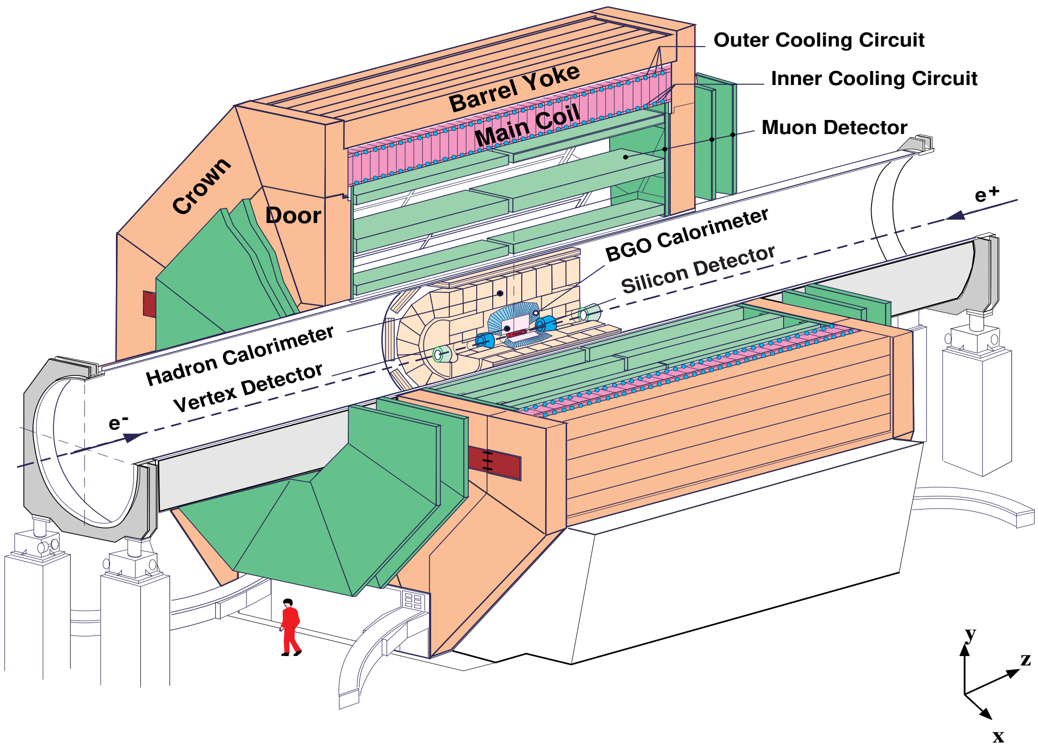

Figure 2.2: *A schematic view of the* L3 *detector.*

used to reconstruct the primary e^+e^- interaction point and possible decay (i.e. secondary) vertices of (long) lived particles, such as the B meson. It consists of :

- A Time Expansion wire Chamber (TEC) to measure the direction and curvature (i.e. the momentum) of charged particles. It comprises two concentric cylindrical chambers. The inner chamber is divided into 12 symmetrical ϕ sectors, the outer chamber into 24 ϕ sectors. A single wire precision of 60 μm [50] results in a transverse momentum resolution of $\sigma(p_T)/p_T = 0.0182 \cdot p_T$ % [1].

- Z chambers situated on the outside of TEC, proportional wire chambers with a field shaped by two rings of anode wires. The proportional signals are collected in the chamber by four layers of cathode strips. Two of the layers surround the inner anode ring, two the outer anode ring. One of the two layers measures the z coordinate, the other is rotated about 20 degrees with respect to the first layer and thus provides a correlated xy and sz measurement, where $\vec{s}$ is the projection of $\vec{r}$ on the xy-plane. The z coordinate is measured with a resolution of 320 μm for Bhabha and dimuon events.

- A Silicon Micro-Vertex Detector (SMD), situated between the beam pipe and TEC. It was installed in 1993 and gives two additional high-precision space points. (More detailed information will be given in the next section).

- The Forward Tracking Chambers (FTC) situated at the forward and backward ends of TEC giving up to 4 additional space points.

The middle part of the detector is dedicated to the energy measurement of the different particles and can be divided into two parts:

- The first part is the Electromagnetic CALorimeter (ECAL) containing Bismuth Germanium Oxide ($Bi_4Ge_3O_{12}$, BGO) crystals. It has a polar angular coverage of $42° - 138°$ (barrel region) and 10°-35° and 145°-170° (end cap region). The energy resolution can be parametrised as [51]:

$$\frac{\sigma(E)}{E} = \sqrt{\left(\sqrt{\frac{2.37}{E}} + 0.38\right)^2 + (1.18)^2 + \left(\frac{0.25}{E}\right)^2}\ \% \tag{2.1}$$

  Besides measuring the energy, it is used for identification of photons and electrons (see section 3.6).

- The second part is the Hadronic CALorimeter (HCAL). It consists of depleted uranium absorber plates, interspersed with proportional wire chambers. The polar angular coverage is 35°-145° (barrel region) and 6°-35° and 145°-174° (end cap region). The energy resolution is given by [52]:

$$\frac{\sigma(E)}{E} = \left(\frac{55}{\sqrt{E}} + 5\right)\ \% \tag{2.2}$$

[1] This is achieved by a TEC only calibration. The use of the SMD in the TEC calibration improves the result by 6 %, see section 2.2.4

The outer part of the detector is dedicated to the measurement of muons: the MUon CHambers (MUCH). Also these are placed within the magnetic field, so they can not only be used to tag muons, but also to measure their momenta. In the MUCH a 50 GeV muon track deviates from a straight line by a sagitta of 3.4 mm over a track length of 3 m [53]. The relative precision of the muon momentum measured in the chambers is given by:

$$\frac{\sigma(p)}{p} = \frac{\sigma(t)}{t} = \left(\frac{800}{0.3}\cdot\frac{\sigma(t)}{BL^2}\cdot p\right)\% \tag{2.3}$$

where p is the momentum of the muon (in GeV), $\sigma(p)$ its error, δt the error on the sagitta t (in meters), B the magnetic field (in Tesla) and L the effective length of the track (in meters). The resolution obtained for a 50 GeV muon is $\sigma(p)/p = (2.5 \pm 0.2)\%$.

A more detailed description of all detector components can be found in [53–55]

2.2 SMD

In 1991 the radius of the beam pipe at the L3 interaction point was reduced from 8.0 cm to 5.5 cm. This allowed to enhance the tracking performance of the TEC by placing a Silicon Microvertex Detector (SMD) in the space that came free. It would, during the LEP-II period, improve the impact parameter resolution, therefore enhance the b quark tagging capability and improve the Higgs discovery potential. It was decided to install the SMD already during the LEP-I phase, so that there would be enough time for debugging in order that it run smoothly by the time LEP-II would start. Thanks to that decision it became possible to do the analysis presented in this thesis. The SMD became fully operational in 1994. The first year's (1994) running experience is described in [56]. Since the SMD is crucial for the analysis of this thesis, only data from 1994 and 1995 are used (up to the point where the LEP energy was increased to 130 GeV at the end of 1995).

2.2.1 Hardware

The SMD consists of two rings (layers) each made of 12 ladders (see figure 2.3). The inner ring is positioned at 60.7 mm from the L3 interaction point, the outer ring at 77.5 mm. Each ladder covers an azimuthal angle of ~ 30 degrees and a polar range $|\cos\theta| < 0.9$. Adjacent ladders in the inner ring have a small (5%) overlap region (see figure 2.4). Each ladder is made of 4 double-sided silicon strip detectors (called wafers). The inner side of each silicon sensor measures the z coordinate, the outer side $r\phi$. The readout strips of the outer ladders are tilted 2 degrees with respect to the inner ones, in order to minimise wrong associations of SMD hits to tracks in high multiplicity environments (see figure 2.5). The grouping of strips in the SMD readout is optimised as to reduce the number of readout channels without deteriorating the intrinsic performance. When the angle under which a track crosses a wafer changes, also the distribution of charge over neighbouring strips changes. As a consequence the accuracy of the determination of the centre-of-gravity changes. The number of strips read out is therefore reduced in the low-angle regions. The SMD also contains a radiation-monitoring system for detector safety, a cooling system, a displacement monitoring system and, of course, a mechanical support.

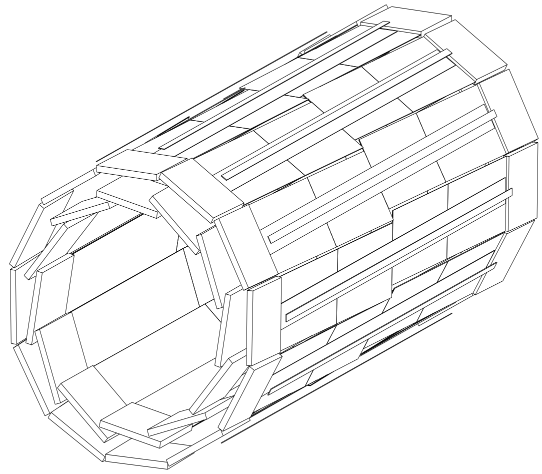

Figure 2.3: *Side view of the* SMD.

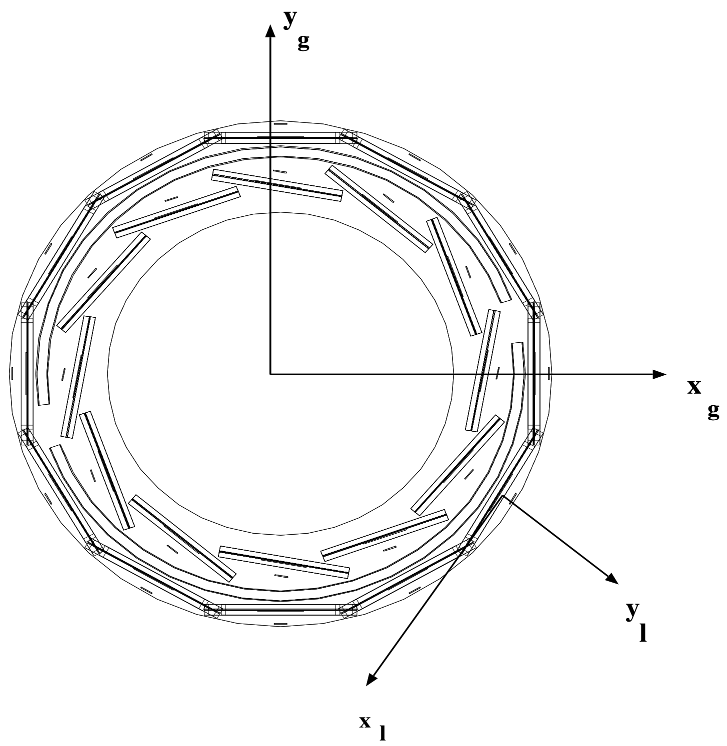

Figure 2.4: *Top view of the* SMD. *The inner ladders have a 5% overlap. Also indicated are the global (*L3*) coordinate system (x_g,y_g) and the local coordinate system of a wafer (x_l,y_l).*

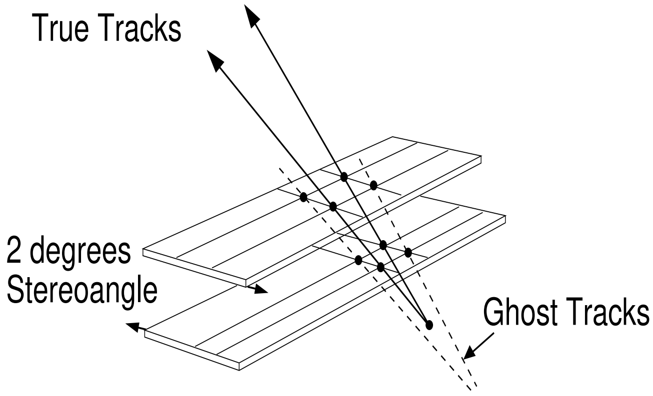

Figure 2.5: *Stereo Angle: The correct assignment of strip coordinates to a charged-particle track is aided by a 2 degree rotation (the so-called stereo angle) of the outer layer. Incorrect matches do not point back to the common vertex.*

Ladders and half-ladders

The basic unit of the SMD is the half-ladder. Each half-ladder is built of a silicon sensor pair, a kapton cable (z-side), two hybrid electronic units (in short just called the hybrid) and the structural support of the half-ladder composed of Aluminium Nitrate (AlN) and quartz plates.

Full SMD ladders are formed by joining two half-ladders with a molded carbon fibre/epoxy support rib of 300 μm thickness and an overall length of 314 mm. The rib is glued to the ϕ surface of the four silicon sensors and the surface of the hybrids. It is isolated from the ladder components by a 0.50 mm thick kapton sheet and grounded to the $r\phi$ side readout of the detector. The overall length of the full ladders is 400 mm. The metrology study in 1993 [57] measured a single ladder assembly precision of $\sim$ 5, 10 and 8 μm in the x, y, z-directions respectively, and a precision of the ladder assembly on the support structure of 15, 25 and 10 μm in x, y, z, respectively.

Sensors and Kapton cable

An SMD sensor is made of 300 μm thick high-purity n-type silicon[2] and has a surface of 70 mm by 40 mm. The junction side of the sensor carries strips implanted every 25 μm with a readout pitch of 50 μm. The strips run parallel to the long side of the sensor and measure the $r\phi$ coordinate.

[2]Impurities with 5 valence electrons have been introduced in the pure silicon that has four valence electrons. This leaves one electron for conduction. In the case of p-type silicon, the impurity has only 3 valence electrons, thus, leaving a hole behind.

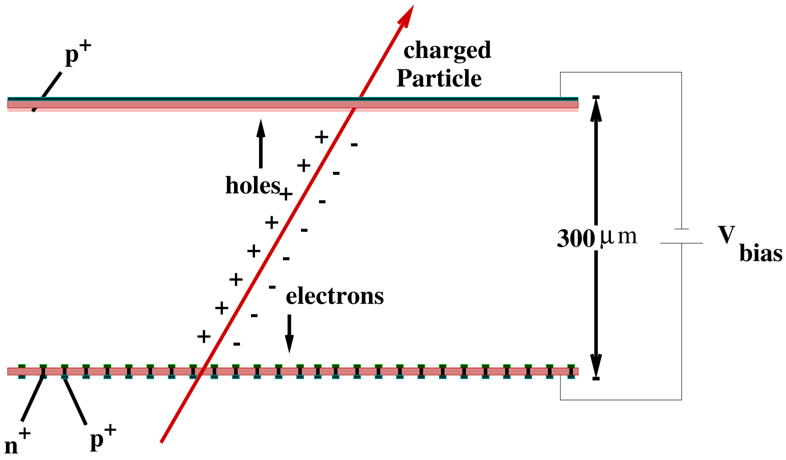

Figure 2.6: *A schematic view of the* SMD *silicon wafer.*

On the sensors ohmic side and perpendicular to the junction-side strips, n^+ strips are placed every 50 μm, with alternate p^+ strips designed to interrupt the surface charge accumulated between the n^+ strips. Since the accuracy of the determination of the centre-of-gravity changes when the track angle changes, the readout pitch is 200 μm over the polar angle θ range $0.93 > |\cos\theta| > 0.53$ and 150 μm over the range $0.53 > |\cos\theta| > 0.0$, where θ is measured with respect to the beam line. These strips measure the z coordinate. When a charged particle passes through the silicon, electron-hole pairs are created. When a voltage bias is applied across the wafer, the electrons and holes will drift to nearby strips on both surfaces (see figure 2.6).

Readout electronics and Data AcQuisition (DAQ)

In figure 2.7 a half ladder is schematically drawn. For the readout of an SMD wafer a so-called SVX chip is used. It is coupled to the Silicon sensors by a capacitor chip placed on a quartz substrate. The SVX chip is glued on an AlN substrate. This substrate is also the base of the hybrid processor. The hybrid contains surface mount resistors and capacitors for distributing chip power and sensor bias voltages and filtering. The signals from the ohmic side of a sensor (z-coordinate) are rerouted from the sensor's long edge to the readout electronics by a flexible kapton cable. This way the readout electronics on this side is taken out of the sensor's active region.

In figure 2.8 the SMD readout and data acquisition (DAQ) is drawn schematically. An intermediate electronic converter board transmits digital and analog signals between the hybrids and the external world. Analog and digital signals are sent between the SVX and the DAQ through the use of an optical transceiver board (a so-called optoboard).

The readout of the SMD silicon strips is done semi-parallel. The 48 hybrids are read out simultaneously while the strips in the 12 SVX chips of each hybrid are read out serially. The SMD signals are received at the DAQ end by a Data Reduction Processor (DRP). A DRP is a hardware filter which suppresses those signals which are not due to the passage of a charged particle through the silicon.

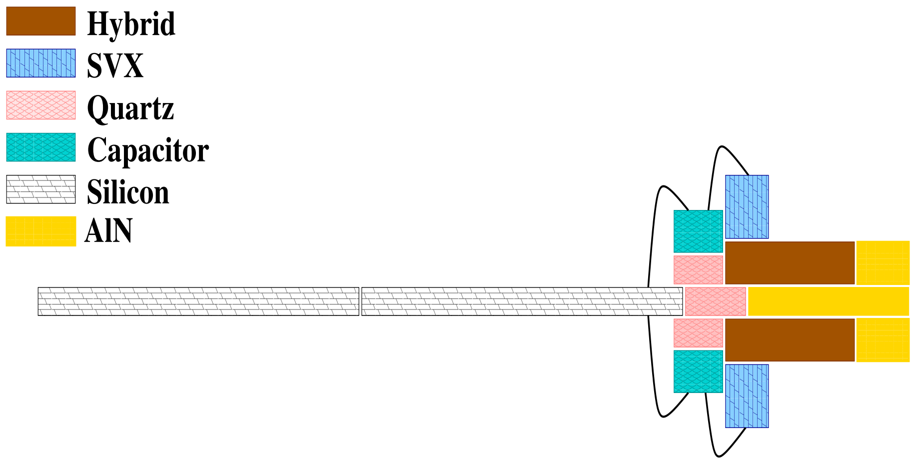

Figure 2.7: *A schematic view of an* SMD *half ladder.*

To calibrate the SMD, a run of several hundred internally generated triggers is performed to determine the Common Mode Noise (CMN)[3] for each SVX chip, along with the pedestal values (Ped) (ADC amplitude in absence of a signal) and their variance ('noise') for each SVX strip. In addition, multiple pedestals are taken with different injected test charges to determine a linear gain fit for each strip. These parameters are stored in the DRP for use by its data reduction algorithms and are also written to an external database.

Support structure

A 1m long cylindrical tube split lengthwise into 2 symmetric halves serves as the mechanical support structure for the ladders and converters of the SMD. Each half-tube is made from 3 separate carbon fibre sections. At both ends and between the sections aluminium alloy half-rings are placed. The interior half-rings contain cooling channels and provide the ladder mechanical fixation. The SMD is attached to the inner wall of the TEC with the outer two half rings.

Cooling system

The SMD components dissipate 200 W of heat. Heat instabilities may disturb the stability of the TEC drift gas. The hybrids are, therefore, cooled by a chilled water-based coolant flowing through a channel in the aluminium alloy support rings. The SMD cooling system is designed to maintain the TEC inner wall temperature at a stable working point ($18 \pm 0.1^\circ$ C) and the readout electronics temperature at some constant temperature less than about 45° C. The temperature stability of the SMD during data taking is better than 0.2°C [58].

[3]The ADC signal amplitude of all channels connected to the same wafer show a coherent time dependent shift called common noise.

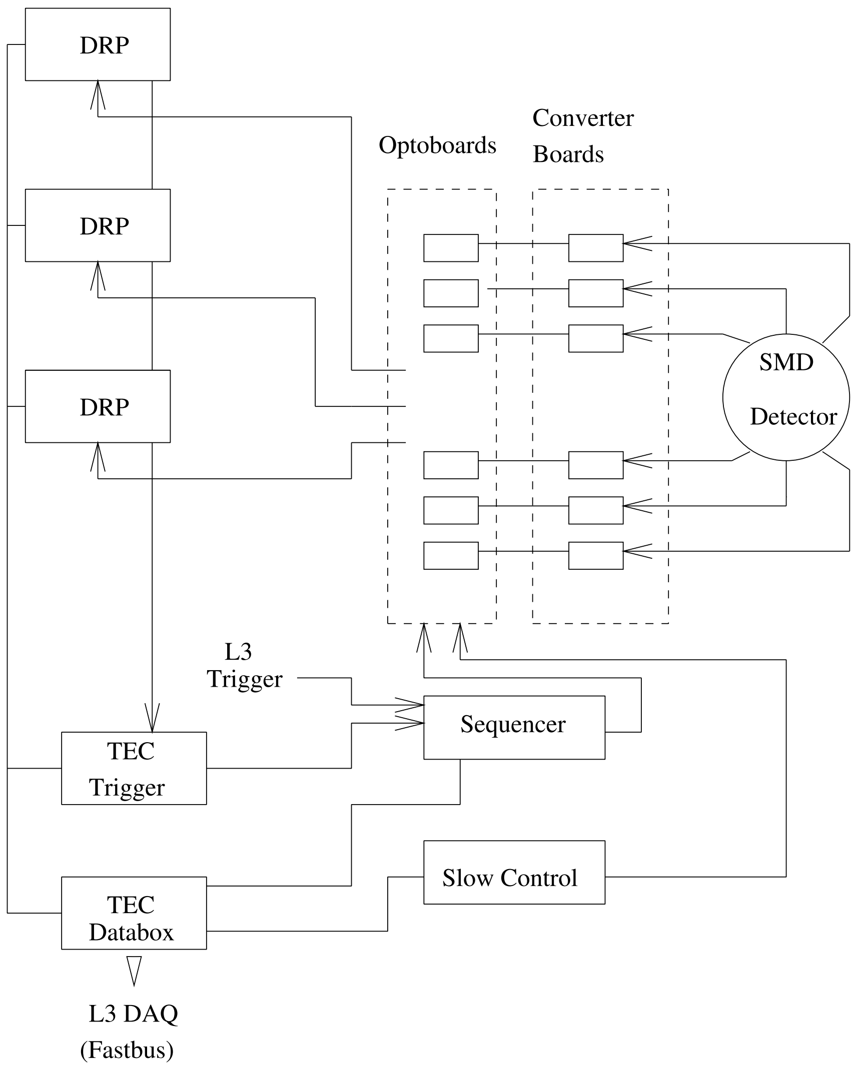

Figure 2.8: *A schematic view of the* SMD *data stream. Signals from the* SMD *detector are converted in the converter boards, 'changed' into light signals in the optoboards and sent to the DRPs. After data reduction has been performed a signal is sent to the* L3 TEC *trigger and the* L3 *DAQ.*

Radiation monitoring

A set of 12 radiation monitoring silicon diodes is installed in the vicinity of the SMD on both sides designed to measure dose rates and integrated doses and to send a beam dump signal to LEP control if the radiation dose rate in the diodes exceeds a predefined threshold. On each side there are 4 diodes. They are used for online monitoring and integrated dose calculations. Their dose rate ranges up to 70 mrad/s. Four other diodes are used for high dose rate monitoring and LEP beam dump. Their rate ranges up to 18 rad/s. Two of the diodes are used for extremely high doses. Their range is up to 6 krad/s. The two remaining diodes are left as spare diodes. The signals from the diodes are integrated over 100 μs and thus sensitive to rapid radiation fluxes. The beam is dumped if either the dose rate in the sensors on both sides of the interaction point exceeds 6 rad/s for at least 300 μs and the SMD is on or if the dose rate exceeds 600 rad/s for at least 300 μs. The latter triggers the beam dump even if SMD is off [59].

Displacement monitoring

The time dependent movement of SMD relative to the TEC is monitored by two individual systems. One system is a Laser Displacement Monitoring System (LDMS) and the other is a Capacitive Displacement Monitoring System (CDMS).

The LDMS consists of a laser diode, which produces 50 ns long pulses of infrared (λ = 905 nm) light, that is transmitted to optical heads, glued to the inner wall of TEC. Each optical head redirects the light onto the silicon wafer, striking the wafers at both 90° and 45° incidence. Test beam results [60] show that reconstruction of the centre of the light spot can be achieved to an accuracy of a few microns. A change of the centre of the light spot indicates relative translation between the SMD silicon wafer and the TEC.

The CDMS is more sensitive to angular displacements than to translations. A sensor on the SMD faces a grounded electrode on the TEC inner wall. An AC current with a frequency of 15 kHz produces a voltage drop between the sensor and the ground that is shaped to produce a nearly DC voltage which varies inversely with the capacitance of the sensor and the grounded electrode. In this way a typical sensitivity of 2.5 mV/μm is achieved for radial displacements and of 0.7 mV/μm [58] for transverse displacements. For the entire SMD six triplets of sensors are used. These triplets are positioned on the SMD support tube. Two triplets are sensitive to displacements in Δr and Δz and four triplets are sensitive to displacements in Δr and $r\Delta\phi$. The resolution, achieved under actual experimental conditions, is 1-2 μm in the radial direction and 5-10 μm in the transverse direction [58].

The running of SMD in 1994

In 1994, a significant amount of common mode noise (CMN) affected the SMD. This manifested itself in many so-called noisy channels that changed during the running period. A new calibration method was developed [56] to take into account the continuously changing noisy channels. A regular calibration was done as described in the previous part to identify the noisy channels after which the pedestals were re-computed. Therefore, the noise problem did not seriously affect the integrity of the SMD data taken during 1994. The main source of the CMN was identified to come from the (switching) power supplies of the SMD itself. A small parasitic capacitance of about 100 pF was still present causing the high CMN levels observed at the beginning of the year. The problem was fixed by synchronisation of the power supplies to each other and the LEP beam crossing [56]. In the winter shutdown, the power supplies were modified to compensate the parasitic capacitor, so in 1995 the SMD ran without CMN problems.

2.2.2 Alignment

For the alignment of the detector two coordinate systems are used. The normal/global L3 coordinate system (as defined above) and a local coordinate system for each wafer. The origin of the local coordinate system is in the centre of the active region of the wafers, the x-axis measuring the $r\phi$ coordinate, the z-axis measuring the z coordinate and the y-axis perpendicular to the sensor, going outwards with respect to the interaction point. The assumption is made that all clusters are located at y=0. See also figure 2.4.

There are two different levels of alignment. The first is the global alignment, i.e., the procedure to measure the SMD position inside the TEC. For this, the SMD is translated and rotated as a whole. Misalignment of the SMD with respect to the TEC can be corrected by three rotations around the x, y and z axes, respectively, and a translation of the SMD centre with respect to the TEC centre. A point $\vec{x_g}$ in SMD global coordinates can, therefore, be described by: $\vec{x_g} = R_z R_y R_x \vec{x_1} + \vec{x_0}$, where $\vec{x_1}$ is a coordinate vector in the ideal (i.e., misaligned) global reference system, the vector $\vec{x_0}$ is the true global position of the centre of the SMD and R_x, R_y and R_z are rotation matrices around the x, y and z axis, respectively.

After the global positioning, the individual wafers may still have a slightly different position with respect to their nominal ones and additional adjustments may be needed. The local alignment proceeds in the same way as the global alignment with rotations around the three local axes and a displacement of the centre of the wafer with respect to the nominal position. This amounts to a total of 576 (6 times 96 wafers) parameters to be determined.

In general, after the most accurate extrapolations of the TEC tracks onto the SMD wafers are found, they are compared with the actual positions of the SMD clusters. The SMD is moved to minimise the discrepancy between the two. For this exercise dimuon and Bhabha (dielectron) events are used. They have the advantage of low multiplicity, which minimises association problems between tracks and clusters.

Global alignment

To find the global alignment, one minimises the residuals of the predicted impact point of the TEC track onto an SMD wafer and the associated clusters. The χ^2 function to be minimised is the following [61]:

$$\chi^2 = \sum_{i=1}^{N_z} w_{z,i} \times (\Delta z_i)^2 + \sum_{j=1}^{N_x} w_{x,j} \times (\Delta x_j)^2, \tag{2.4}$$

where $\Delta z = z_{\mathrm{TEC}} - z_{\mathrm{SMD}}$ for clusters on the z side and $\Delta x = x_{\mathrm{TEC}} - x_{\mathrm{SMD}}$ for clusters on the the $r\phi$ side. The weights w_z and w_x are derived from the errors in the residuals in the relevant local coordinate. They are dominated by uncertainties in the TEC prediction on the wafer. The sum runs over all $r\phi$ and z clusters matched with TEC tracks.

For a more detailed description of the global alignment see reference [61]. The final results for 1994 and 1995 can be found in reference [62]. After global alignment, there is still a misalignment of the order of 20-30 μm in $r\phi$ and 50-100 μm in z [61].

Local alignment

The predictions of TEC-only tracks on the SMD wafer are not precise enough for the purpose of local alignment. The prediction can be improved by adding another SMD cluster to the TEC track. There are two possibilities: (same) side prediction and back-to-back prediction. For the side prediction, the SMD cluster under consideration is compared to a track that has been refitted with either an SMD cluster in the other SMD ring, or a cluster in the overlapping ladder, or a combination of the two (see figure 2.9). The overlap region provides information on relative positions inside the ring. The comparison of hits in the inner and outer ring provides information on the relative position of the two rings.

For the back-to-back prediction dimuon and Bhabha events are selected. Here, a wafer on one side of the SMD is positioned with respect to a wafer on the opposite side of the SMD. In the case of the L3 detector with a magnetic field of 0.5 T and a silicon detector very close to the vertex, the assumption is made that all hits lie along a straight line. This increases statistics since predictions can be made with only two SMD points.

The χ^2 to be minimised is the same as that for the global alignment given in eq. (2.4), but the differences are in local coordinates and the predictions come either from the side- or the back-to-back case or both. Both x_{SMD} and z_{SMD} hits are required on a wafer unless one side of the wafer is known to be non- or badly functioning. Alignment parameters are determined assuming they are small, so only first-order terms are taken into account. In the aligned system, new predictions are obtained and the alignment procedure is iterated until individual residues reach 0.1 times the estimated error or the χ^2 value begins to increase. The results can be found in [62].

2.2.3 Track Matching

The outer layer of the SMD is rotated 2° with respect to the inner layer around the axis perpendicular to its wafer plane. This rotation correlates the xy and z measurements.

The measurements in the local SMD reference system l_i $(i = 1,4)$ [4] can be rotated and translated to L3 global coordinates in the two rings A (inner) and B (outer) in the following way:

$$\begin{aligned}
\mathrm{A}:\quad & x_a = l_2 && \text{Layer } 2 && (2.5)\\
& y_a = 0 && && (2.6)\\
& z_a = l_1 && \text{Layer } 1 && (2.7)\\
\mathrm{B}:\quad & x_b = l_3\sin\theta + l_4\cos\theta && \text{Layer } 4 && (2.8)\\
& y_b = 0 && && (2.9)\\
& z_b = l_3\cos\theta - l_4\sin\theta && \text{Layer } 3, && (2.10)
\end{aligned}$$

where $\theta \simeq 2°$ is the 'stereo angle' of the outer layer.

For the matching only well-measured TEC tracks and SMD clusters are used. The TEC tracks must satisfy the requirements:

- DCA < 80 mm.

[4] l_1 (l_2) represents a hit in the inner SMD z (ϕ) layer z_{inner} (ϕ_{inner}) and l_3 (l_4) represents a hit in the outer SMD z (ϕ) layer z_{inner} (ϕ_{outer}).

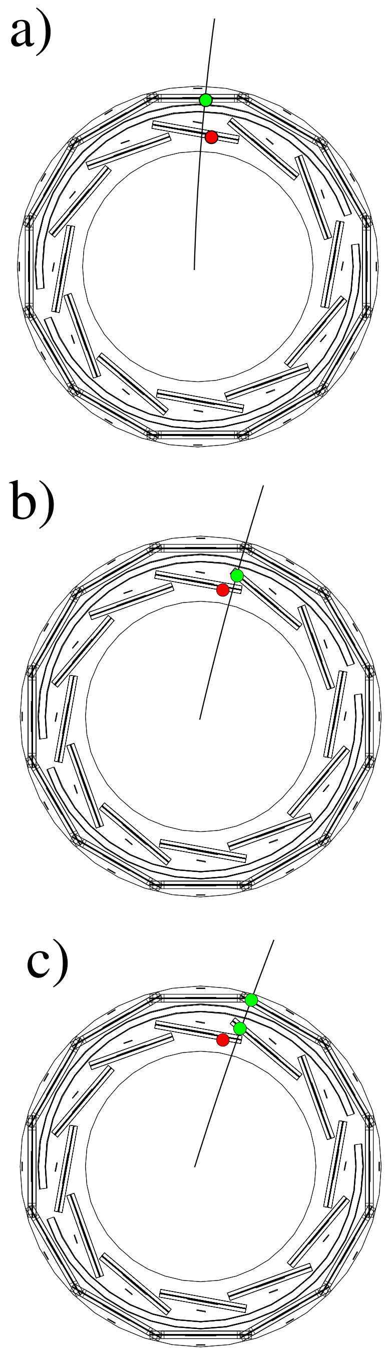

Figure 2.9: *Types of 'side' predictions for the internal* SMD *alignment. a) Two layers, b) overlap, c) best case.*

- number of TEC hits ≥ 10
- span ≥ 15
- sz fit performed,

where, the DCA is the distance-of-closest-approach in the transverse plane to the interaction point, and the span is the length of the track expressed as the number of wire distances covered in TEC.

An SMD cluster consists of a group of SMD strips that were hit, i.e. strips were upon charge is deposited by a particle that passes through the SMD wafer. The SMD clusters are selected by the following criteria:

- cluster amplitude ≤ 250 ADC counts
- number of cluster hits ≥ 1
- signal/noise ratio of cluster ≥ 5
- cluster width(number of strips) $\geq \begin{cases} 3 & \text{for } x \text{ clusters,} \\ 5 & \text{for } z \text{ clusters.} \end{cases}$

A track is extrapolated to the ladder under consideration. In layer 2, simply, the cluster closest to the prediction within 3.5 times the uncertainty is taken. If two different tracks point to the same cluster, the cluster is associated to the closer track in layer 2. Due to the overlap region it is possible that one track has two clusters associated with it. These clusters are in different ladders, however. With an ideal MC sample, i.e., without detector effects taken into account, an efficiency to find at least one hit on a track that crosses layer 2 of $(88.2 \pm 0.3)\%$ is obtained. A misidentification rate was found to be $(1.0 \pm 0.1)\%$ [63].

Layer 4 only contributes to an improvement of the TEC track if also a cluster in layer 3 is found (because of the stereo angle). It is, therefore, decided to take just the closest cluster in layer 4. The resulting efficiency is (76.7 ± 1.1) % on tracks with an associated cluster in Layer 2 and the misidentification rate is $(1.1 \pm 0.3)\%$ [63].

For association in Layer 3 an improved prediction, the so-called 'stereo-prediction', is used. From eq. (2.8) follows:

$$l_3^{\text{predicted}} = \frac{x - l_4 \cos\theta}{\sin\theta}, \tag{2.11}$$

where x is the global coordinate in the xy plane (from the TEC) and l_4 is the local cluster prediction. Using all events with a cluster in the 4th layer and taking the cluster in layer 3 closest to the stereo prediction, an efficiency of $(91.8 \pm 0.2)\%$ is obtained. The misidentification was found to be $(2.7 \pm 0.2)\%$ [63].

After the track is refitted with the 'stereo' clusters found in the outer layers, the residues of the TEC prediction and clusters in layer 1 are taken. There are long tails in the distribution that come from tracks not pointing to the interaction vertex. These residues are improved if a better estimate of the z-coordinate of the event vertex is found and the tracks are refitted with this improved vertex constraint. However, tails remain since not all tracks (for instance b-decay tracks) originate from the vertex. With the improved prediction an efficiency of $(84.7 \pm 0.3)\%$ is obtained, with a misidentification rate of $(4.2 \pm 0.2)\%$ [63]. Finally, all clusters closest to the track after all previous refits are accepted.

2.2.4 Calibration of TEC with SMD

A further advantage of the SMD is that now the calibration of the TEC can be improved with information from the SMD. Instead of performing the TEC calibration with information mainly coming from the chamber itself (an iterative and difficult procedure) it can be done using mainly information from outside TEC and is non-iterative, stable and can reach the internal precision of the chamber. This way, the TEC resolution improves [64](for the 94b period):

- the angular resolution from 0.9 to 0.4 mrad,
- the DCA resolution from 133 to 105 μm,
- the p_T resolution from 0.0182 to $0.0171 \cdot p_T$ %.

2.2.5 SMD efficiency

Experimentally, not all tracks are matched with hits in all four layers of the SMD. This inefficiency can have several causes:

- digitiser and amplifier (the hybrid) malfunction (dead half ladder)
- noisy channels
- a dead z_{outer} layer causing also a dead ϕ_{outer} layer
- wrong TEC prediction
- aging effects

The ladder efficiency ε_l, defined as the number of times a cluster is associated with a track that crosses the active region of the ladder. For both SMD inner layers and the z_{outer} layers efficiencies are found of about 80 to 85 % and for the ϕ_{outer} layers an efficiency of about 65 % [65]. This last lower efficiency is due to the fact that a coincidence is required with a z_{outer} hit.

2.2.6 SMD resolutions

The SMD point resolution is 10 μm in the $r\phi$ plane and 21 μm $\oplus$ 15 μm / $\tan\theta$ and 21 μm $\oplus$ 26 μm / $\tan\theta$ in the sz plane for the normal and large pitch region, respectively. The symbol $\oplus$ indicates that the numbers should be added in quadrature. Thus a vertical track has a resolution of 21 μm in the sz plane.

Another important measure of physical precision is the distance-of-closest-approach resolution. With the SMD a DCA resolution of 66 μm is obtained in hadronic events (see figure 2.10).

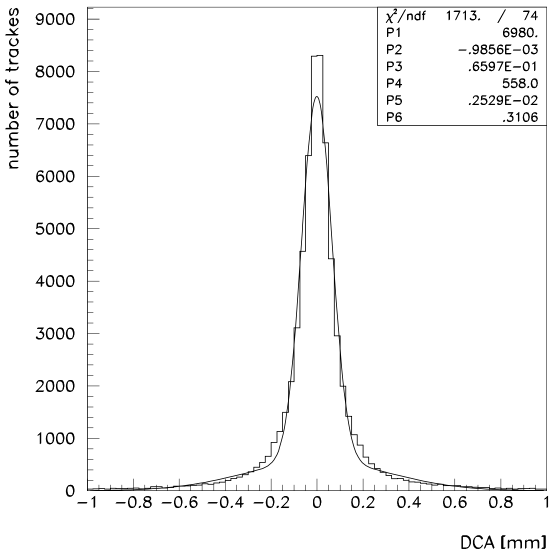

Figure 2.10: *The DCA resolution in hadronic events. For the fit a double Gaussian is used. P1 and P4 are the heights of the two Gaussians, P2 and P5 are the mean values and P3 and P6 are the widths.*

2.3 The simulation

To study the efficiencies and purities of the collected data, they are compared with Monte Carlo (MC) simulated data. This simulation is performed in two stages. First, the events are generated according to our present knowledge of particle production in the reactions:
$e^+e^- \rightarrow \gamma/Z \rightarrow q\bar{q} \rightarrow$final state particles. The program used to describe these reactions is JETSET [66]. After that, the detector simulation is run. Two specific software packages are used: GEANT [67] and SIL3 (SImulation of L3). The first package is very general and can be used to simulate the interaction of any particle with any detector material, the second package is L3 specific. The simulated events are written to tape in the same format as are normal data events.

The inefficiency of the detector subcomponents is taken into account by the software from information of a database containing the sub-detector performances during actual data taking runs. A MC run with a fully operational detector is called ‘ideal’ detector MC simulation. When time dependent effects are taken into account, the MC simulation is called a ‘real’ detector simulation.

Chapter 3

Reconstruction and selection methods

The strategy to observe excited B mesons is to examine the invariant-mass spectrum of the BX system, where X is a pion in the case of a $B^{**}_{u,d}$ meson and a photon in the case of a B^{*} meson. The invariant mass is given by:

$$M_{BX} = \sqrt{M_B^2 + M_X^2 + 2E_B E_X - 2\vec{p_B} \cdot \vec{p_X}} \quad . \tag{3.1}$$

The masses M_B and M_π of the B meson and pion are known [4]. The energy and the direction of the B meson are measured and $\vec{p_B}$ is calculated from these. The same is done for the π^0 and the photon. For the $\pi^\pm$, the transverse momentum and the direction are measured and $\vec{p_\pi}$ and E_π are calculated from these.

Before performing the analysis on experimental data, we study the Monte-Carlo (MC) simulation of the $B^{**}_{u,d}$ decay and the detector response to it. This is described in section 3.1. The selection of events (in actual data and MC simulation) and the tagging of B mesons is presented in section 3.2. The selection of charged pions is given in section 3.3. In section 3.4, several reconstruction methods are investigated to obtain the energy and the direction of flight of the B meson. The method best suited for the purpose of the $M_{B\pi}$ determination is chosen on the basis of the signal-to-noise ratio and the real invariant-mass resolution as defined in section 3.1. In section 3.5, the invariant-mass spectrum is obtained for the charged-pion channel and compared to the MC predictions.

The neutral-pion selection is described in section 3.6. In section 3.7 a sideband study is performed to determine the characteristics of the combinatorial background.

Although the parameters of the B^{*} meson are already well known, we present a study of B^{*} decays in section 3.8, as a check of the reconstruction method used for the $B^{**}_{u,d}$ channel. The B^{*} decays electromagnetically to a B meson and a photon. For the reconstruction of the B^{*} the same B-meson reconstruction is used as for the analysis of the $B^{**}_{u,d}$. The photon selection is described in the last section.

3.1 Monte-Carlo predictions

First, we examine the $B^{**}_{u,d}$ signal generated according to a Monte-Carlo (MC) model. After that, the variables important for the determination of the B-meson reconstruction method optimally suited to the present analysis are discussed. Charged pions are used, since the charged-pion channel has more statistics, since charged-track reconstruction is more efficient than π^0

reconstruction. However, it is assumed that the conclusions are applicable to the neutral-pion channel, as well.

In figure 3.1 (a), the Monte-Carlo (MC) prediction for the $B^{**}_{u,d}$ mass spectrum is plotted as the sum of the narrow ($j_q = 3/2$ B^*_2 and B_1) and broad ($j_q = 1/2$ B^*_1 and B_0) states. Spin counting is used ($B^*_2 : B_1 : B^*_1 : B_0 = 5 : 3 : 3 : 1$) for the relative cross sections and Breit-Wigner functions are assumed with the following mass and width values:

$$\begin{array}{ll} M_{B^*_2} = 5.769 \ \text{GeV} & \Gamma_{B^*_2} = 0.040 \ \text{GeV} \\ M_{B_1} = 5.757 \ \text{GeV} & \Gamma_{B_1} = 0.030 \ \text{GeV} \\ M_{B^*_1} = 5.634 \ \text{GeV} & \Gamma_{B^*_1} = 0.100 \ \text{GeV} \\ M_{B_0} = 5.675 \ \text{GeV} & \Gamma_{B_0} = 0.100 \ \text{GeV}\,. \end{array}$$

The 'generated' $B^{**}_{u,d}$ mass resolution is defined as the difference $M_{B^{**}_{u,d}} - M_{B\pi}(\text{gen})$ between the generated mass and the invariant mass M_{BX} obtained according to eq.(3.1) from the *generated* B and π variables. This is plotted for B^*_2, B_1 and the combined [1] B^*_1 and B_0 in figure 3.1 (b), (c) and (d), respectively. When the Bπ invariant mass is calculated according to eq. (3.1), it is assumed that the $B^{**}_{u,d}$ decays to Bπ [2]. For the states that actually decay to $B^*\pi$, the invariant mass $M_{B\pi}$, therefore, underestimates the $B^{**}_{u,d}$ mass. The resolution is thus shifted to positive values. This can be seen e.g. in sub-figure (c) where the resolution plotted for $B_1 \to B^*\pi$ is not centred around zero. In sub-figure (d), two peaks are observed, one due to $B_0 \to B\pi$ around zero and one shifted to positive values due to $B^*_1 \to B^*\pi$. In figure (b), however, three peaks are observed, one around zero due to $B^*_2 \to B\pi$ and one shifted to positive values due to $B^*_2 \to B^*\pi$. The third peak, at even higher positive values, is due to $B^*_2 \to B^{(*)}\pi^{\pm}\pi$. Since only one pion is explicitly taken into account in the invariant-mass calculation, the Bπ invariant mass underestimates the $B^{**}_{u,d}$ mass even more.

We, furthermore, define the 'real' resolution as $M_{B^{**}_{u,d}} - M_{B\pi}(\text{rec})$, where the invariant mass is still calculated according to eq.(3.1), but from the *reconstructed* B-meson and pion variables. This resolution is plotted in figure 3.2. In (a) no pion selection is applied, in (b) track-quality cuts are applied and in (c) an additional cut on the pion energy ($E_\pi > 1.5$ GeV) is required (see section 3.3). The real resolution is fitted with a single Gaussian function. It improves when good quality tracks are required and a cut on the pion energy is performed. The improvement is mostly due to the fact that the third peak of figure 3.1 (b) disappears. This can easily be understood as in those cases the $B^{**}_{u,d}$ decays into a B meson and two pions instead of one. The available energy has to be shared among these and the 'observed' pion is of low energy. The two other peaks visible in figure 3.1 (b) and (d) are smeared by resolution and can no longer be resolved in figure 3.2. It is, therefore, impossible in this analysis to disentangle the narrow and broad states from each other.

In figure 3.3 the reconstructed invariant Bπ mass is plotted for MC events. The pions are selected according to selection criteria to be described in section 3.3. The dots are all MC Bπ combinations and the shaded histogram corresponds to all Bπ background combinations, i.e., to those combinations that do not originate from a $B^{**}_{u,d}$. A signal can be observed above the background as a wide enhancement between 5.4 and 6 GeV.

[1] For editorial reasons B^*_1 and B_0 have not been plotted in separate plots. Since B^*_1 decays only to $B^*\pi$ and B_0 only to B π, the two states can be distinguished in one plot.

[2] The $B^*\pi$ is not considered in this analysis, since the detection of the B^* decay-photon would reduce the statistics too much for the $B^{**}_{u,d}$ measurement.

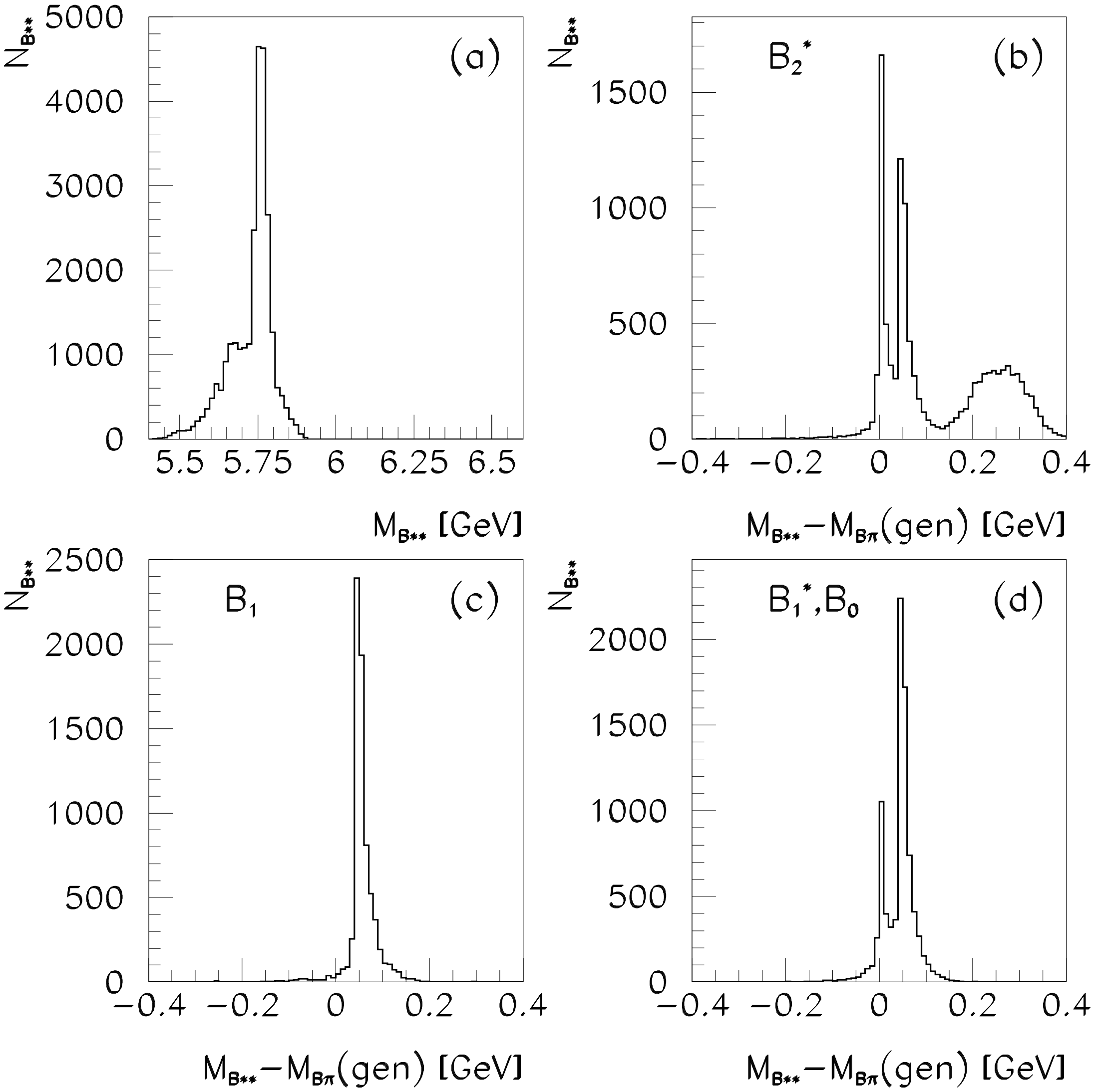

Figure 3.1: *The* $B^{**}_{u,d}$ *mass in (a) and its resolution,* $M_{B^{**}_{u,d}} - M_{B\pi}(\mathrm{gen})$*, where the invariant mass* $M_{B\pi}(\mathrm{gen})$ *is obtained from the generated B-meson and pion variables for the* B^*_2 *(b) the* B_1 *(c) and the* B^*_1 *and* B_0 *(d) states, respectively.*

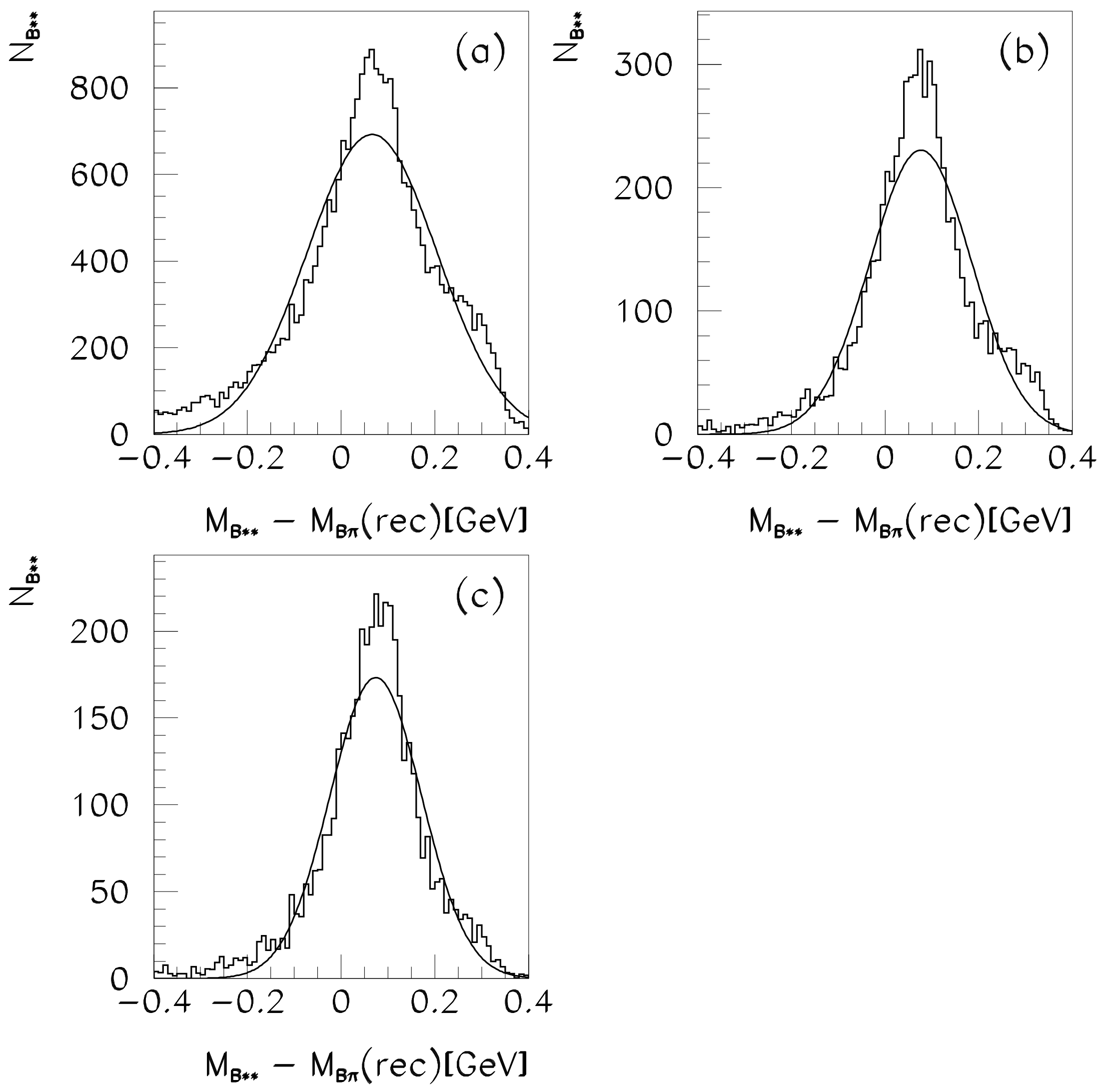

Figure 3.2: *The real* $B^{**}_{u,d}$ *mass resolution,* $M_{B^{**}_{u,d}} - M_{B\pi}(\mathrm{rec})$*, where the invariant mass* $M_{B\pi}$ *is obtained from the reconstructed B-meson and pion variables, with no cuts on the selected pions (a), with track-quality cuts (b) and with an additional cut on the energy of the pion (c).*

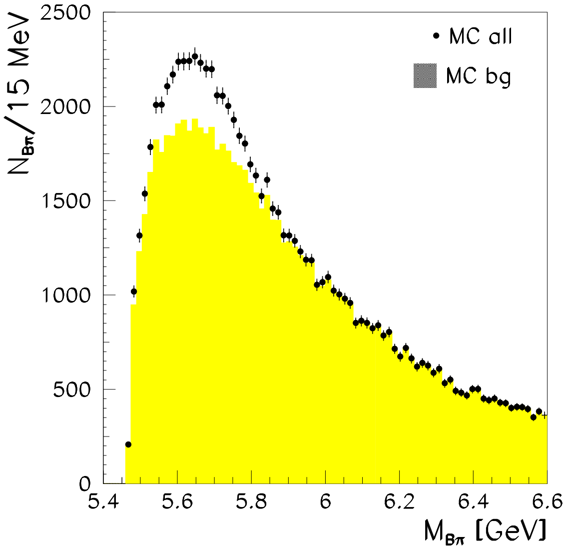

Figure 3.3: *The MC invariant Bπ mass, $M_{B\pi}$, when the reconstructed B meson and pion values are used. The dots are all combinations and the shaded histogram are the background combinations, i.e., those combinations that do not originate from a* $B^{**}_{u,d}$.

Another important quantity is the signal-to-noise ratio, S/N. It is defined as the ratio of signal combinations to background combinations in the signal region of 5.4-6.0 GeV. Both the ‘real’ resolution and the signal-to-noise ratio will be used to determine which B-meson reconstruction method and pion-selection criteria should be applied.

3.2 Event selection

3.2.1 Hadronic event selection

Firstly, a hadronic event selection is performed similar to that used for the measurement of the total hadronic cross section [68], with the aim to obtain a sample of events in which the Z^0 decays into $q\bar{q}$ pairs:

- $|\cos\theta_{\mathrm{thrust}}| < 0.72$
- $0.6 < \frac{E_{\mathrm{vis}}}{\sqrt{s}} < 1.4$
- $\frac{E_{\perp}}{E_{\mathrm{vis}}} < 0.4$
- $\frac{E_{\parallel}}{E_{\mathrm{vis}}} < 0.4$
- number of BGO clusters ≥ 13,

where θ_{thrust} is the polar angle of the thrust axis $\vec{n_{\mathrm{t}}}$ [3], E_{vis} the total visible energy, the sum of the jet energies and remaining cluster energies, $\sqrt{s}$ the centre of mass energy, $E_{\perp}$ the energy imbalance in the plane transverse to the beam axis and $E_{\parallel}$ the longitudinal energy imbalance. The cut on the number of BGO clusters rejects $\mathrm{Z}\to \mathrm{e^+e^-}, \mu^+\mu^-, \tau^+\tau^-$ decays. The energy cuts discard 2-photon events, the cuts on the energy imbalance discard beam-gas and beam-wall events and the cut on the angle of the thrust axis is applied to ensure good tracking, i.e., to select events in the barrel region.

Secondly, in addition to this hadronic selection, it is required that there be no more than 2 jets in an event. The jets are obtained by the Simple JeT (SJT) algorithm. First, the calorimetric cluster with the highest energy is taken. After that, the clusters in a cone of 30° around this high energy cluster are summed to form a jet. The procedure is repeated with the remaining clusters until there are no more high energy clusters to be found (i.e. clusters with an energy of at least 7 GeV). Finally, clusters within a cone of 20° of a cluster that has already be assigned to one of the jets is also included in that jet. The jet direction is defined as the centre-of-gravity direction of all the clusters assigned to the jet. The energy of the jet is obtained by the summation over the energies of the clusters assigned to the jet. In this analysis, only jets with an energy higher than 10 GeV are taken into account. The cut on the number of jets is needed for the reconstruction of the B-meson properties described below.

Finally, it is required that there be more than 5 tracks that have been fitted with the Kalman Filter [69]. The so-called Kalman Filter fit gives an estimate of the track resolution, based on the TEC and SMD resolution functions and the GEANT description of the material. The track parameters and the error matrix based on TEC information are projected onto the outer SMD plane and serve as an initial prediction point. The weighted average is taken between the measured and predicted track parameters while multiple scattering effects are included. The new track parameters are projected onto the next (inner) SMD plane and the procedure is repeated. In this way good error estimates for tracks are obtained. The Kalman-filter track fit makes optimal use of the SMD information, particularly for low momentum tracks, and removes poorly reconstructed and fake tracks [70]. This requirement is needed for a good reconstruction of the primary vertex representing the Z-decay vertex, and thus for the tagging algorithm of b quarks.

3.2.2 B-tagging

After the standard hadronic-event selection, a selection is applied to obtain a sample of $\mathrm{Z}\to \mathrm{b\bar{b}}$ decays. Before installation of the SMD, usually a lepton tag was applied. Due to the large b-quark mass, the lepton from the semileptonic B-meson decay can have high momentum p and transverse momentum p_{T} with respect to the jet axis. By selecting events containing a lepton with high p and p_{T}, a high-purity sample of $\mathrm{b\bar{b}}$ events is obtained. However, since semileptonic branching fractions of the B meson are small, this method had a low efficiency.

With the installation of SMD, several techniques have been developed which make use of the long lifetime of b-hadrons to tag $\mathrm{Z}\to \mathrm{b\bar{b}}$ events. One method explicitly reconstructs the B-meson decay vertex and thus the decay length. Another method uses the impact parameter (with respect to the primary vertex) of the reconstructed tracks to calculate a probability that the event does not contain a b quark.

[3]The thrust axis $\vec{n}_{\mathrm{t}}$ is the direction for which $\sum_i |\vec{p_i}\cdot\vec{n_{\mathrm{t}}}|/\sum_i|\vec{p_i}|$ is maximal, where p_i is the momentum of particle i, so that $\vec{n_{\mathrm{t}}}$ can be considered as the main event axis.

We choose a three dimensional (3D) tagging algorithm, which achieves an efficiency of 70 % with a b-hadron purity of 80 %. The high efficiency of the 3D method is crucial for the present analysis. This method is described in detail in [70] and is only summarised here: Firstly, a 3D primary vertex (PV) is reconstructed, using tracks which fulfil the following requirements:

- fitted with Kalman Filter
- $|d_{\mathrm{r}\phi}| < \min(10\ \mathrm{mm},\ \ 5\sigma(d_{\mathrm{r}\phi}))$
- $|d_{\mathrm{sz}}| < 100\ \mathrm{mm}$,

where $d_{\mathrm{r}\phi}$ is the distance of closest approach in the xy-plane, d_{sz} that in the sz-plane and $\sigma(d_{\mathrm{r}\phi})$ is the error on $d_{\mathrm{r}\phi}$. The following χ^2 is minimised:

$$\chi^2_N = \sum_{i=1}^{N}[\vec{t_i} - \vec{f}(\vec{v},\vec{q_i})]^{\mathrm{T}} G_i^{-1}[\vec{t_i} - \vec{f}(\vec{v},\vec{q_i})] + (\vec{v} - \vec{v_{\mathrm{fill}}})^{\mathrm{T}} V_{\mathrm{fill}}^{-1}(\vec{v} - \vec{v_{\mathrm{fill}}}), \qquad (3.2)$$

where N is the number of tracks under consideration, $\vec{t_i}$ is the vector of measured parameters for the i^{th} track and G_i the corresponding covariance matrix, $\vec{f}(\vec{v},\vec{q_i})$ are the predicted measurements assuming the track originated from the vertex $\vec{v}$ with momentum $\vec{q_i}$, $\vec{v_{\mathrm{fill}}}$ is the so-called fill or N-event vertex [71, 72], which is the mean event vertex in N events obtained by minimising $\chi^2 = \frac{d_i^2}{\sigma_i^2}$, where d_i is the DCA in the xy-plane and σ_i is the error on the DCA, and V_{fill} describes the size of the beam spot.

For each track, the probability $P_i = P(\chi^2_N - \chi^2_{N-1,i})$ is calculated and if either the vertex probability χ^2_N is below 4% or any P_i is below 2%, the track with the lowest P_i is removed. The fit procedure is iterated until no more tracks need to be removed. In the end, only those primary vertices are used for which at least 3 tracks have remained.

Secondly, a plane perpendicular to the thrust axis divides the event into two hemispheres. The assumption is made that the direction of the B meson is given by the jet as defined by the simple jet algorithm. For each track in a given hemisphere a decay length is computed along the jet direction and the probability that it originates from the primary vertex. To do this, the distance of closest approach is defined in the $r\phi$ plane ($d_{r\phi}$) and the sz plane (d_{sz}). These distances are signed positive (d_1 in figure 3.4) if the track crosses the jet axis in the direction of the jet, negative (d_2 in figure 3.4) if the extrapolation of the track crosses at the opposite side. The distance between the primary vertex [4] and the crossing point of the track with the jet axis, the so-called decay length of the track, is determined in both projections ($L_{r\phi}$ and L_{sz}, respectively) and given the same sign as the distance of closest approach. These projected decay lengths provide independent measurements of the true decay length of the B meson and the weighted average can be taken to form the decay-length variable L. Tracks from the decay of long-lifetime particles as the B meson will usually have a large and positively signed decay length.

The $r\phi$ measurement usually dominates the average, because SMD and TEC have better resolution in that plane. However, if the $r\phi$ measurement is not useful, for example if a track is at small angle to the jet direction in the $r\phi$ projection, the sz decay length measurement

[4] For tracks that were used in the primary vertex, the PV reconstruction is recalculated without the track under consideration. This to avoid correlations in the track probabilities.

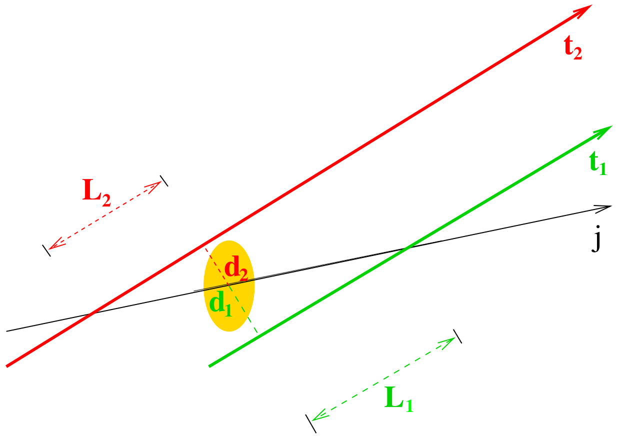

Figure 3.4: *The sign definition of $d_{r\phi}$ and d_{sz}. Track t_1 crosses jet j in the jet direction and the distance of closest approach d_1 is therefore signed positive. The extrapolated track t_2 crosses the jet on the opposite side and d_2 is therefore signed negative. The ellipse represents the errors on the primary vertex.*

becomes important. The probability that the $r\phi$ and sz measurements are compatible with each other peaks at small probabilities. Therefore, the two measurements are averaged if that probability is larger than 5%. Otherwise, only the $r\phi$ projection is used, thus minimising the effect of mistakes in the sz pattern recognition.

Furthermore, the significance $S = L/\sigma_L$, where σ_L is the error on the decay length L, is used to compute the probability that a given track with decay length L is compatible with coming from the primary vertex. The assumptions are made that tracks with a negative sign come from the PV and that the probability density $f(S)$ is symmetric around zero. Then the negative side of the significance distribution can be used to determine the distribution $f(S)$ of S. The track probability function,

$$P(|S_i|) = \frac{\int_{|S_i|}^{\infty} f(S)\mathrm{d}S}{\int_0^{\infty} f(S)\mathrm{d}S}, \tag{3.3}$$

gives the probability that track i originating from the primary vertex has a significance $|S_i|$ or larger. A track originating from a secondary (B decay) vertex will have a large significance S and hence small $P(S)$.

Finally, the track probabilities can be combined into a hemisphere or an event probability. In earlier b-tagging methods such as the 2D tag [73], the probability was obtained by simple multiplication of the probabilities of positive-decay-length tracks only. In that case, the probability to obtain a product of track probabilities smaller than the observed value is calculated. The event probability is given by (see appendix A):

$$P_{\mathrm{event}} = \Pi \sum_{i=0}^{N-1} \frac{(-\ln \Pi)^i}{i!}, \quad \text{where } \Pi = \prod_{j=1}^{N} P(S_j), \tag{3.4}$$

and where N is the number of tracks in the event with positive decay length. By construction,

P_{event} is flat for events which contain no long-lifetime particles, whereas events containing decay tracks from long-lifetime particles cause a peak at $P_{\text{event}} = 0$.

However, the method neglects the number of tracks with negative decay length. That these tracks are important can be seen in the following example: If there are 10 tracks with a negative sign and 2 tracks with a positive sign, the evidence for lifetime is not as strong as in the case that there are 2 positively signed tracks and only 1 negatively signed track. Negative-decay-length tracks can be included by setting $P = 1$ under the assumption that tracks from long-lifetime particles as the B meson never have a negative value of S. Using also here the product of probabilities, this results in the following event probability:

$$P'_{\text{event}} = \frac{\Pi}{2^N} \sum_{i=0}^{N-1} \sum_{j=i+1}^{N} \binom{N}{j} \frac{(-\ln \Pi)^i}{i!}, \qquad \text{where } \Pi = \prod_{j=1}^{N^+} P(S_j), \tag{3.5}$$

where N is the total number of tracks in the event and N^+ is the total number of tracks with positive decay length. Again P'_{event} is flat for events that contain no long-lifetime particles, while events that do contain long-lifetime particles have probabilities close to zero. The derivation of P_{event} and P'_{event} is given in appendix A, where, furthermore, it is shown that with a cut on P'_{event} a better efficiency is obtained than when P_{event} is used. From now on, P'_{event} will be used as the event probability. Since the event probability is very small in the case of B decays, one can expand the region of interest by defining the discriminant

$$B_{\text{event}} = -\log P'_{\text{event}}. \tag{3.6}$$

The efficiency ε_{b} of the B-tagging can be obtained from Monte-Carlo sampling as the ratio of the number of selected b events to the total number of b events generated. The purity π_B is the ratio of the number of selected b events to the total of selected events. In the data, the efficiency can be determined by:

$$\varepsilon_{\text{b}} = \frac{R_{\text{tag}} - R_{\text{c}}\varepsilon_{\text{c}} - (1 - R_{\text{b}} - R_{\text{c}})\varepsilon_{\text{uds}}}{R_{\text{b}}}, \tag{3.7}$$

where R_{b} and R_{c} are the fractions of b-quark and c-quark events in the hadronic sample, respectively (taken from the MC), ε_{c} and ε_{uds} are the c quark and uds quark efficiencies (taken from MC) and R_{tag} is the total fraction of tagged events in the data [5].

In figures 3.5 and 3.6, the event discriminant B_{event} distribution, in the top plot, and the efficiency and purity as a function of a cut on the discriminant, in the bottom plot, are plotted for the 1994 data and MC and the 1995 data and MC, respectively. As can be seen from the bottom plots, the efficiency of the B-tagging obtained in the data and MC agree well. The purity obtained in data and MC (superimposed in the figure) agree very well by definition. Since there is a difference between the distributions for the two years, different cuts for the two data samples are necessary to obtain the same purity. For the 1994 data a cut of 2.3 is chosen and for the 1995 data a cut of 2.0. This results in a purity of 82.1 % and an efficiency of 63.8 % for both years combined.

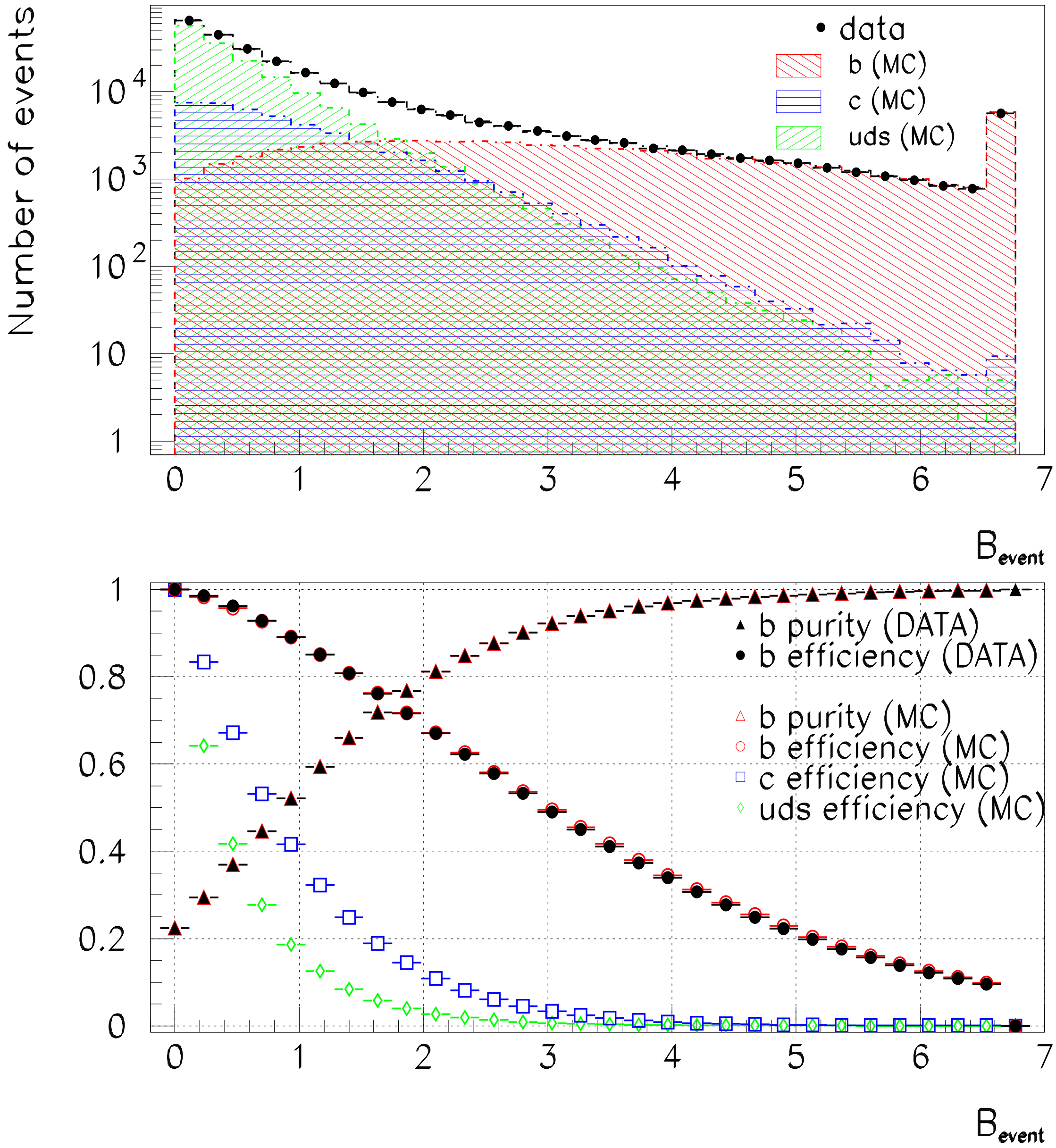

Figure 3.5: *The event-discriminant distribution for the 1994 data and MC is shown in the upper plot. The last bin is the overflow bin. The efficiency and purity as a function of a cut on the discriminant is shown in the bottom plot.*

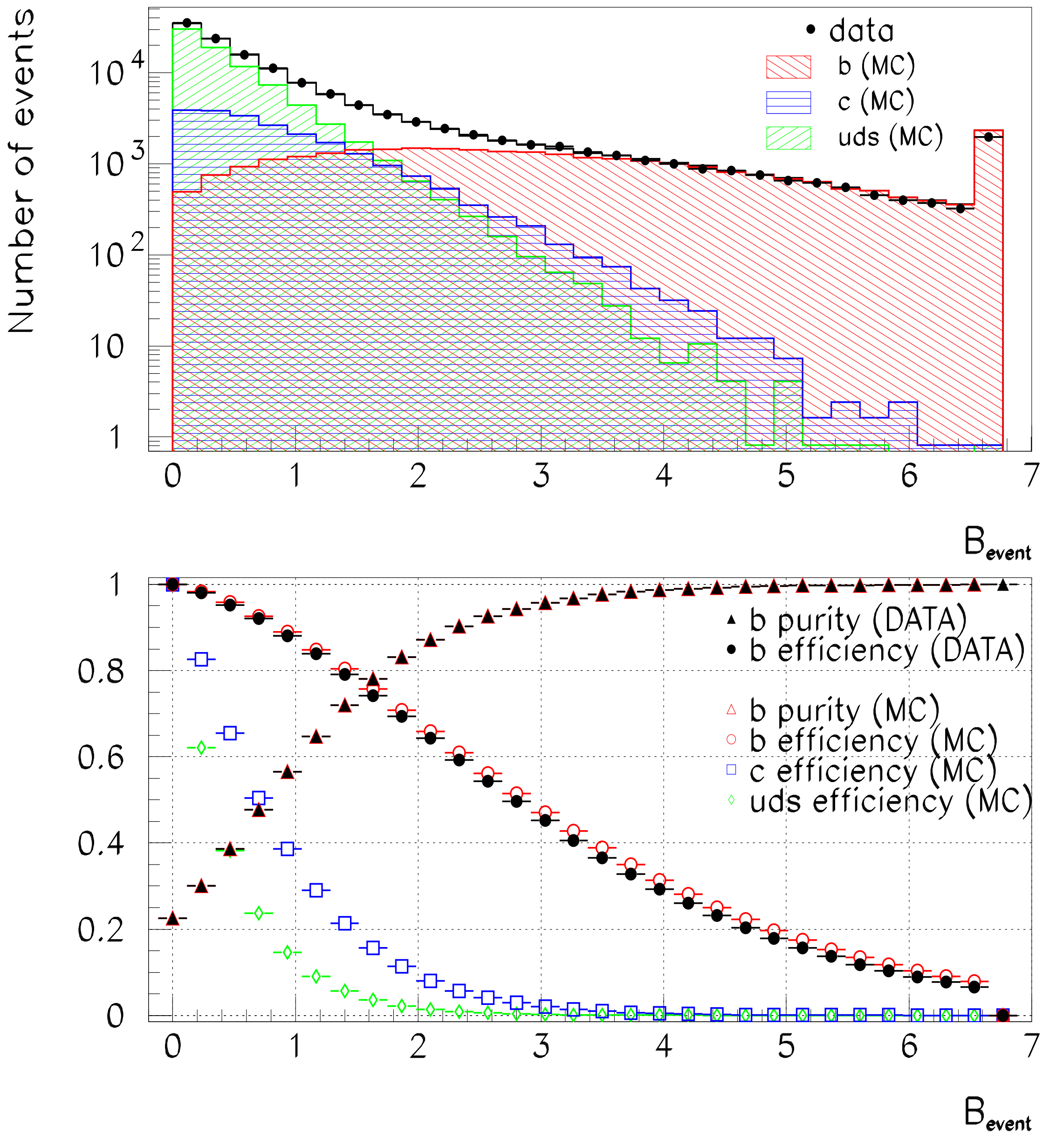

Figure 3.6: *Same as figure 3.5, but for the 1995 data and MC.*

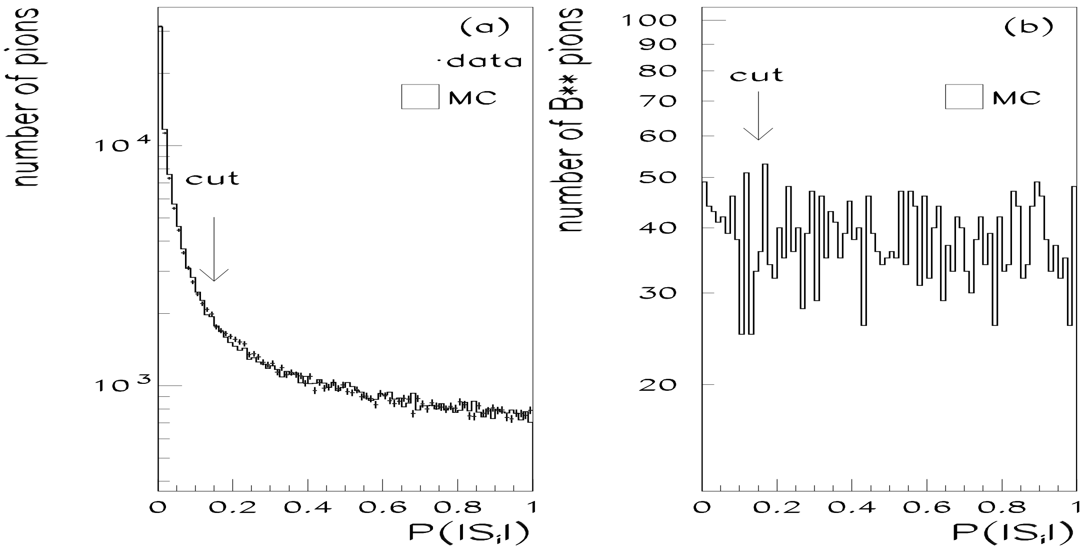

Figure 3.7: *The probability distribution for a track to come from the PV (a) and the probability for a* $B^{**}_{u,d}$ *pion to come from the PV, as obtained from MC (b).*

3.3 Charged-pion selection

All charged tracks are assumed to be pions. Firstly, they have to fulfil the following selection criteria (these are the same requirements as used for the B tagging method [70]):

- Number of TEC hits ≥ 30
- span ≥ 40
- Number of TEC inner hits ≥ 1
- $p_\perp > 300$ MeV
- $D_{\text{poca}} < 650\,\mu\text{m}$ [6]
- $d_{r\phi} < 2$ mm
- $|\phi_{\text{local}}| > 0.005$.

The span is the wire-number difference between the first and the last hit of the TEC track, $p_\perp$ is the transverse momentum of the track, D_{poca} is the distance of closest approach between the track and the jet axis in 3D, $d_{r\phi}$ is the distance of closest approach in the xy plane and ϕ_{local} is the angle between the track and the closest inner TEC anode. Furthermore, tracks were

[5] By defining ε_b as a function of R_c, ε_c, ε_{uds} and R_b the purity in data is the same as the MC purity by construction.

[6] only for tracks with sz information

selection	$\frac{S}{N}$ [%]	$M_{B^{**}_{u,d}} - M_{B\pi}$ [GeV]	$\varepsilon_{\pi^{\pm **}}$
none	2.0	0.156	-
quality	2.9	0.115	27.5
previous + P_{PV}> 0.15	5.1	0.114	23.0
previous + $p_{t\pi}$> 0.130 GeV	5.5	0.099	20.5
previous + ϕ cut	5.6	0.099	18.8
previous + most energetic	6.0	0.086	12.6

Table 3.1: *The signal-to-noise ratio, the $M_{B\pi}$ resolution and the $\pi^{\pm **}$ efficiency for the pion selection cuts.*

required to have at least two z measurements. A z measurement can be one of the following: z_{outer} in combination with a ϕ_{outer} SMD hit , a z_{inner} SMD hit, or a Z chamber (TECZ) hit, where ϕ_{inner} (ϕ_{outer}) is an SMD hit in the inner (outer) $r\phi$ layer of the SMD and z_{inner} (z_{outer}) is an SMD hit in the inner (outer) sz layer of the SMD. This means that the tracks are required to have : (ϕ_{inner} and ϕ_{outer} z_{outer}) and (TECZ or z_{inner} or both). From now on, these track selections will be referred to as the track quality cuts.

Secondly, since the $B^{**}_{u,d}$ decays strongly, the decay pion comes from the primary vertex (PV). The probability $P(|S_i|)$, as defined in eq.(3.3) that the particle originates from the PV can, therefore, be used as a selection variable. The probability distributions (data and MC) for all selected pions are plotted in figure 3.7 (a) and show a steep peak for $P(S_i) < 0.15$. That of the MC $B^{**}_{u,d}$ pions is plotted in figure 3.7 (b) and is relatively flat, i.e., most $B^{**}_{u,d}$ pions come from the PV. In addition to the above selection criteria, the track is, therefore, required to have a probability $P(|S_i|) > 15$ %.

While pions come from many sources, including the decays of K, K*, K**, η and ω, only pions from D* and D** tend to peak in the Bπ mass spectrum (see figure 3.8). In the same figure, the transverse momentum $p_{t\pi}$ of the pion with respect to the B-meson direction is plotted for pions originating from $B^{**}_{u,d}$, D* and D**. As can be seen, the D* pions peak at low transverse momenta. With a cut of 0.130 GeV, most of these pions can, therefore, be rejected without losing too much of the signal events.

The pion θ and ϕ distributions from data and MC are compared in figures 3.9 and 3.10. In two TEC regions, there is a difference between data and MC in the ϕ direction due to incorrect modelling of detector efficiencies. Since this difference could bias the analysis, cuts are applied to eliminate these regions.

Finally, as most of the signal $B^{**}_{u,d}$ pions are the most energetic one in the jet, only the most energetic particle in the jet is selected.

In table 3.3 the signal-to-noise ratio (S/N) and the $M_{B\pi}$ resolution ($M_{B^{**}_{u,d}} - M_{B\pi}$), as defined in section 3.1, and the $\pi^{\pm **}$ efficiency $\varepsilon_{\pi^{\pm **}}$, where $\pi^{\pm **}$ is used to indicate the $\pi^{\pm}$ from the $B^{**}_{u,d}$ decay, is listed for the pion selection. It is clear that both S/N and the Bπ resolution improve with each additional cut.

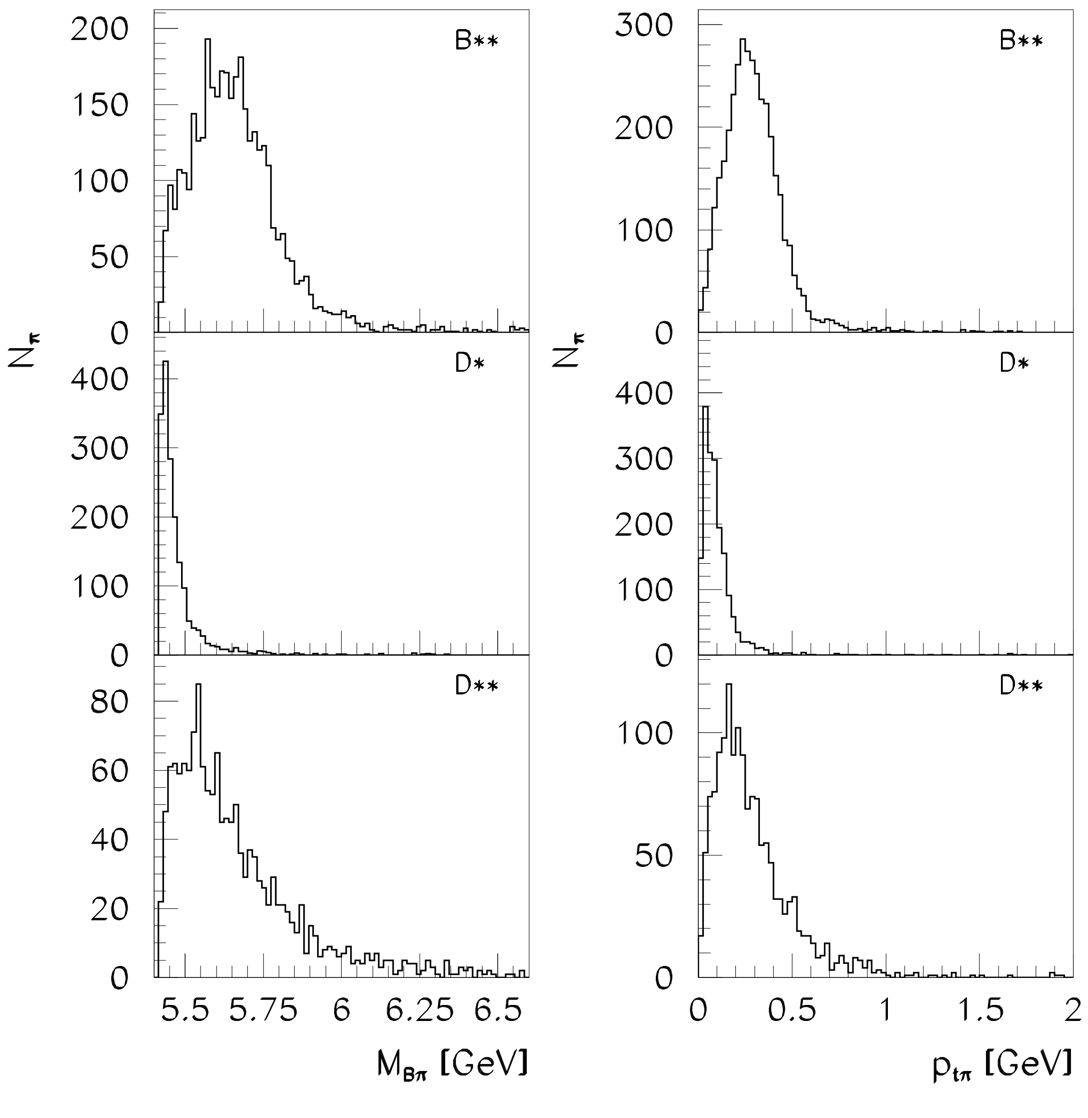

Figure 3.8: *The* B$\pi^{\pm}$ *mass distributions, where the charged pion originates from the decay of the* $\mathrm{B}^{**}_{\mathrm{u,d}}$, D^{*} *and* D^{**} *on the left-hand side and the transverse-momentum distributions of those pions on the right-hand side.*

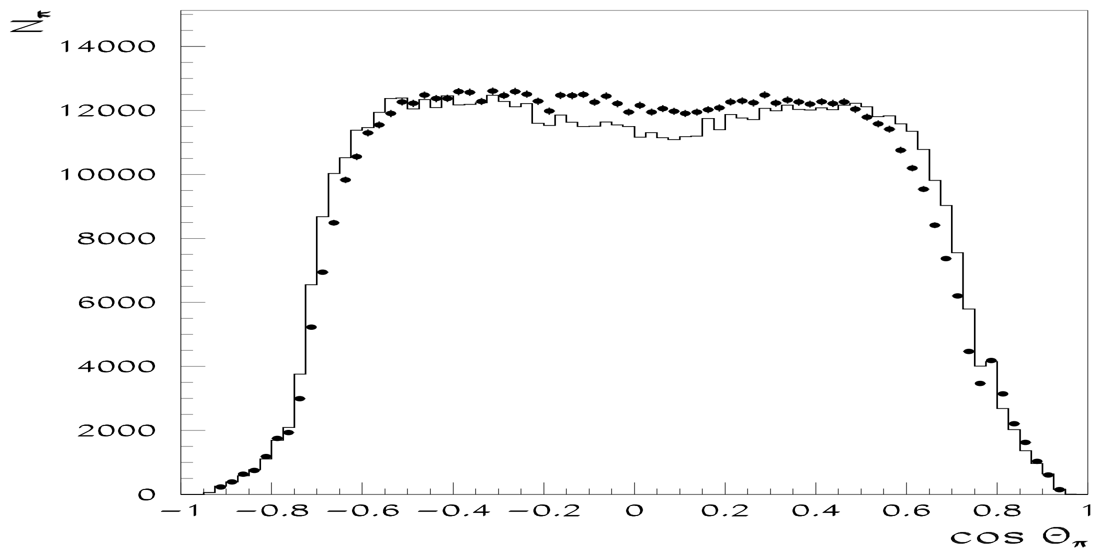

Figure 3.9: *The* $\cos\theta$ *distribution of the pion for data (dots) and MC (solid line).*

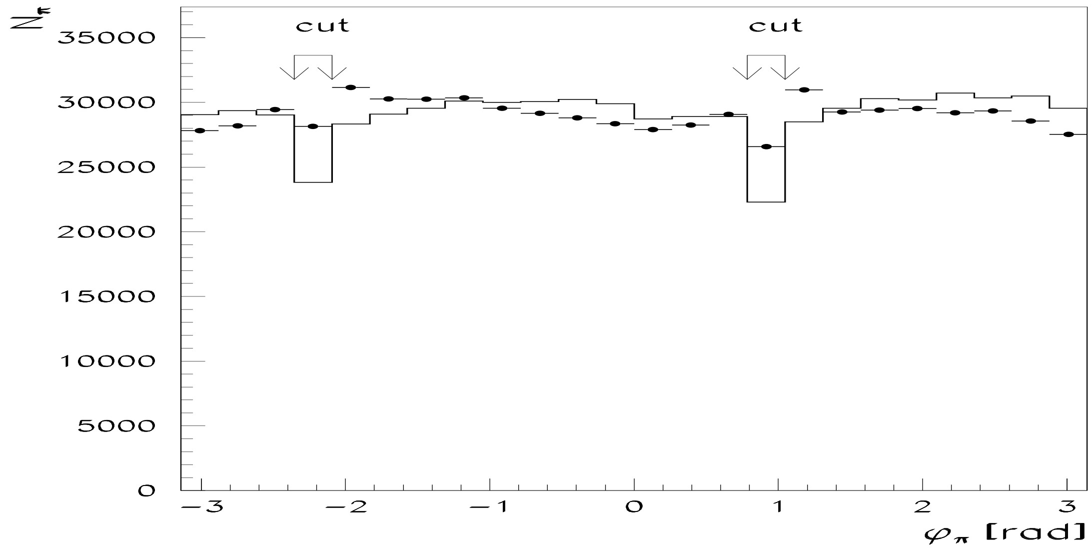

Figure 3.10: *The* ϕ *distribution of the pion for data (dots) and MC (solid line).*

3.4 B-meson reconstruction

A secondary (B-decay) vertex algorithm can be used to obtain the B-meson direction, as described in subsection 3.4.1. A so-called rapidity algorithm can be used to reconstruct both the B-meson energy and direction. This is described in subsection 3.4.2. The application of an additional constraint for the reconstruction of the B-meson energy is described in subsection 3.4.3, the application of a weighted average of the rapidity and of SV methods for the reconstruction of the B-meson direction in subsection 3.4.4.

3.4.1 Secondary-vertex reconstruction

For the reconstruction of secondary vertices the same information is used as for the b-tagging method: the decay length of a track. Tracks with compatible decay lengths are grouped to form vertices. The following likelihood function is maximised:

$$\mathcal{L} = \sum_{iv=1}^{N_{\mathrm{vtx}}} \sum_{it=1}^{N_{iv}} -\log(P(\chi^2_{it,iv})) - \log(N_{iv}), \tag{3.8}$$

where $\chi^2_{it,iv} = \frac{(L_{it}-L_{iv})^2}{\sigma^2(L_{it})+\sigma^2(L_{iv})}$, and L_{it} is the decay length of track it, L_{iv} is the decay length of vertex iv, $\sigma(L_{it})$ is the error on the track-decay length and $\sigma(L_{iv})$ is the error on the vertex-decay length. When the track had already been assigned to this vertex, the vertex-decay length is recalculated without the track under consideration. A penalty is given (i.e., $\log(P(\chi^2_{it,iv})) = -4.5$) when the algorithm tries to make a vertex of one track.

When a group of N tracks is found with compatible decay lengths, a similar algorithm as for the PV reconstruction is used. The χ^2 of eq.(3.2) is minimised, but the vertex is constrained to lie along the jet axis, assuming that the direction of flight of the B meson is given by the jet axis.

In figure 3.11 (a) the reconstructed B-decay length L is plotted and in (b) the B-decay length divided by its error L/σ_L. In the following part of the analysis it is required that $L > 3\sigma_L$. This results in a b-purity of 85.5 %.

After a secondary vertex is found the PV is refitted without the SV tracks. Also the b-tagging algorithm is repeated with the new PV.

An estimate of the B-meson direction can be obtained by the line connecting the primary and the secondary vertex:

$$\theta = \arctan\left(\frac{\sqrt{x^2+y^2}}{z}\right) \qquad \phi = \arctan\left(\frac{y}{x}\right), \tag{3.9}$$

where $x = x_{\mathrm{s}} - x_{\mathrm{p}}$, with similar expressions for y and z, and x_{p} is the x-coordinate of the primary vertex and x_{s} that of the secondary vertex. The resolution obtained for the θ and ϕ angles from the secondary-vertex (SV) method is shown in figure 3.12. The distributions are fitted with a double Gaussian and the resulting fit parameters are listed in table 3.2. In section 3.4.4 they will be compared with the results from other B-reconstruction methods.

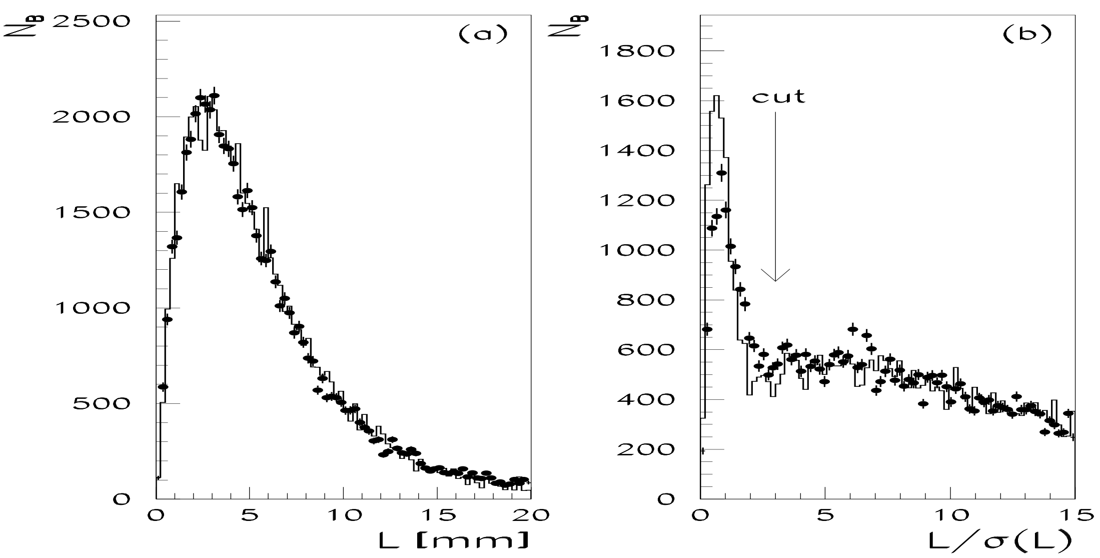

Figure 3.11: *The B-meson decay length (a) and the decay length divided by its error (b).*

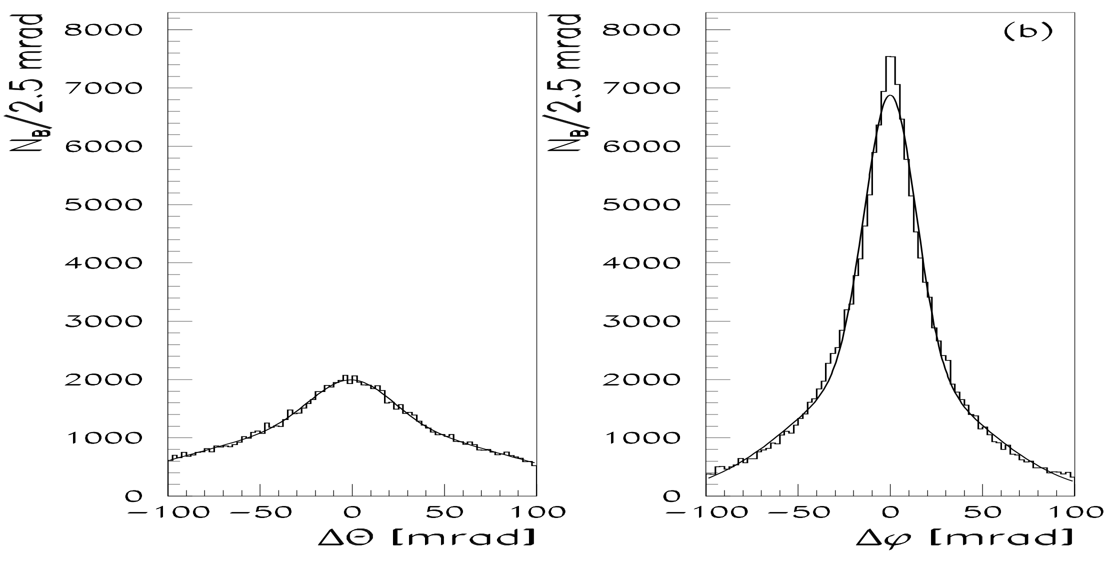

Figure 3.12: *The* θ *resolution* ($\theta_{gen} - \theta_{rec}$)*(a) and* ϕ *resolution* ($\phi_{gen} - \phi_{rec}$)*(b) obtained by the SV method. Both distributions are fitted with a double Gaussian. The parameters and their errors are summarised in table 3.2.*

algorithm	angle	μ_1	σ_1	$\frac{A_1}{A}$	μ_2	σ_2	$\frac{A_2}{A}$
SV-PV	θ	-0.55 ± 0.42	22.1 ± 0.7	0.151 ± 0.011	-2.8 ± 0.6	83.8 ± 2.0	0.849 ± 0.011
	ϕ	-0.07 ± 0.08	13.8 ± 0.1	0.387 ± 0.007	-2.3 ± 0.2	49.1 ± 0.3	0.613 ± 0.007
rapidity	θ	-0.13 ± 0.09	21.6 ± 0.2	0.543 ± 0.012	0.34 ± 0.18	46.9 ± 0.5	0.457 ± 0.012
	ϕ	-0.027 ± 0.10	21.4 ± 0.2	0.490 ± 0.012	-2.25 ± 0.17	46.8 ± 0.4	0.510 ± 0.012
weighted + χ^2	θ	-0.35 ± 0.09	21.4 ± 0.2	0.527 ± 0.012	0.44 ± 0.17	46.2 ± 0.5	0.473 ± 0.012
	ϕ	-0.17 ± 0.08	16.7 ± 0.1	0.442 ± 0.007	-2.3 ± 0.1	44.0 ± 0.3	0.558 ± 0.07

Table 3.2: *The fitted parameter values of the resolution of the B-meson direction for the different methods. σ_1 and σ_2 are the widths and μ_1 and μ_2 the mean values in mrad and the areas A_1 and A_2 are divided by the total area A of the two-Gaussian fit.*

3.4.2 Rapidity algorithm

The B-meson energy and direction are reconstructed with the help of the rapidity algorithm. The rapidity is defined as $y = 0.5 \cdot \ln(\frac{E+p_{\|}}{E-p_{\|}})$, where $p_{\|}$ is the component of the momentum along the jet axis as defined by the simple jet (SJT) algorithm described in section 3.2.1. Charged particles are TEC/SMD tracks and they are assumed to be pions. Neutral particles are calorimetric clusters, reconstructed as ASRC's (Across L3 clusters) by the L3 reconstruction program. All neutral particles are assumed to be massless. As can be seen from MC events in figure 3.13, B-meson decay particles are expected to have on average higher rapidity than particles from fragmentation. Charged and neutral particles are assumed to be B-meson decay particles if their rapidity is larger than 1.5.

The direction and the transverse momentum of a charged track are measured by the TEC and the SMD, the energy is derived by assuming the particle mass to be the pion mass. The tracks are required to fulfil the same track-quality selection criteria as the pions in section 3.3. The pion selected in section 3.3 does not participate in the algorithm, since it is assumed to be the $B^{**}_{u,d}$ decay pion and thus not a B-decay particle.

The neutral-particle direction and energy are obtained from the calorimetric cluster. In the general L3 reconstruction program the assumption is made that such clusters originate from the centre of the L3 detector. Here, the direction is recalculated under the assumption that the neutral particle comes from the reconstructed primary (i.e. Z^0 decay) vertex.

The algorithm starts by assuming that the B direction is identical to the jet direction obtained by the SJT algorithm from calorimetric clusters recalculated under the assumption that it originates from the PV. Then, the particle with the lowest rapidity with respect to this direction is discarded. The algorithm then calculates a new 'B-meson direction' and this procedure is repeated until all particles have a rapidity with respect to the B-meson direction higher than

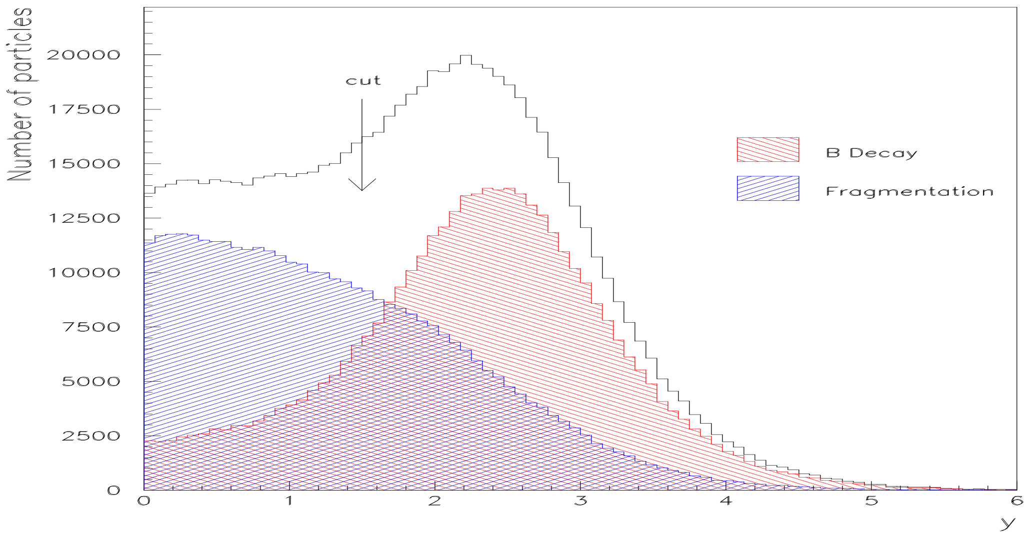

Figure 3.13: *The rapidity distribution for both neutral and charged particles from B-meson decay and from fragmentation, as predicted by MC.*

1.5. The B-meson energy is now simply given by the sum over the energies of all particles selected and the B-meson direction obtained from the sum over the momenta of the selected particles.

The energy distribution is shown in figure 3.14 (a), the energy resolution $\Delta E_B = E_{gen} - E_{rec}$, i.e., the difference of MC generated and reconstructed energy, in figure 3.14 (b). A single Gaussian function is used to fit the resolution and the fit parameters are summarised in table 3.3. A rather poor energy resolution of about 13 GeV is obtained in this manner. The resolutions for the θ and ϕ angles obtained by the rapidity method are shown in figure 3.15. The resolution is fitted with a double Gaussian and the resulting fit parameters are listed in table 3.2. These values will be compared with those obtained with other methods in sections 3.4.3 and 3.4.4.

3.4.3 B-meson energy

The energy resolution can be improved by constraining the energy obtained in the rapidity algorithm by the known centre-of-mass energy. The relation is given by:

$$E_B = \frac{E_{cm}^2 - m_{rec}^2 + m_B^2}{2E_{cm}}, \tag{3.10}$$

where E_{cm} is the centre-of-mass energy, m_B is the invariant mass of all particles with rapidity higher than 1.5 and m_{rec} is the invariant mass of all particles with rapidity lower than 1.5 . The energy distribution and energy resolution obtained in this way are plotted in figure 3.16 (a) and (b). The resolution is asymmetric and is fitted with a bifurcated Gaussian function. The widths are 2.7 GeV on the right-hand side, 4.5 GeV and 10 GeV on the left-hand side.

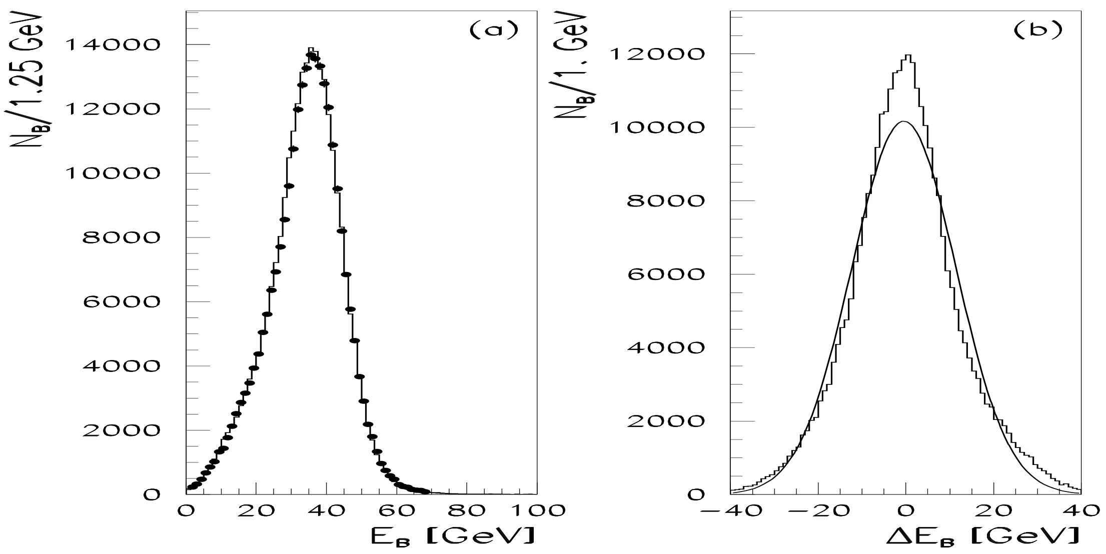

Figure 3.14: *(a) The energy of the B meson obtained from the rapidity algorithm. (b) The energy resolution of the B meson ($E_{\text{gen}} - E_{\text{rec}}$) obtained from the rapidity algorithm. The resolution is fitted with a Gaussian function. The parameters and their errors are summarised in table 3.3. The dots are data and the histogram is MC.*

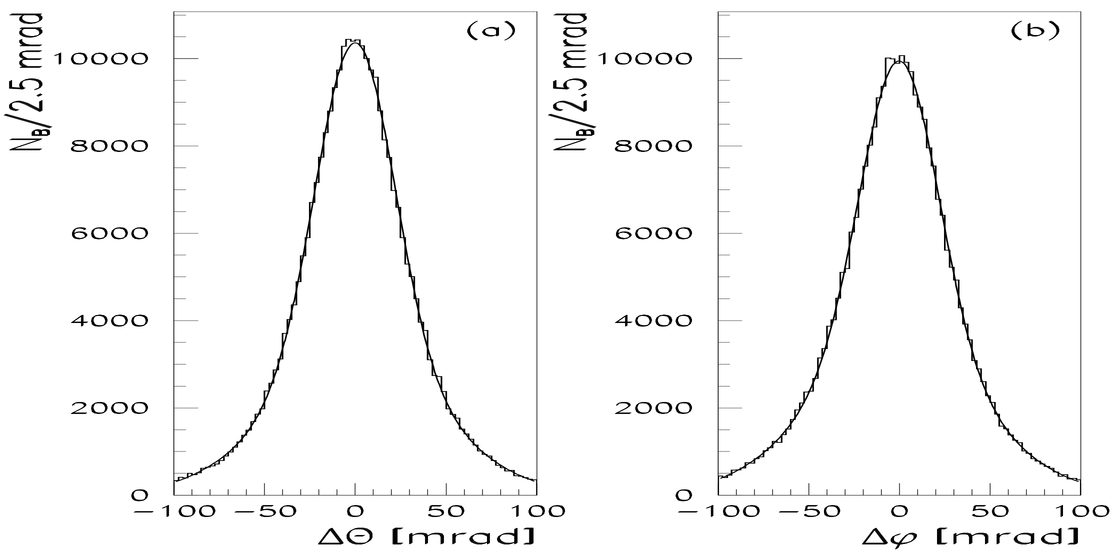

Figure 3.15: *The θ resolution ($\theta_{\text{gen}} - \theta_{\text{rec}}$)(a) and ϕ resolution ($\phi_{\text{gen}} - \phi_{\text{rec}}$)(b) obtained by the rapidity algorithm. Both distributions are fitted with a double Gaussian. The parameters and their errors are summarised in table 3.2.*

algorithm	μ_1	σ_1	σ_2	μ_2	σ_3
rapidity	-0.48 $\pm$ 0.02	11.9 $\pm$ 0.02			
rapidity + constraint	-0.13 $\pm$ 0.03	2.17 $\pm$ 0.02	4.63 $\pm$ 0.03	-5.77 $\pm$ 0.07	10.12 $\pm$ 0.04

Table 3.3: *The fit values of the resolution of the B-meson energy in* GeV*. In the first line, the resolution σ_1 and mean value μ_1 of the fitted single Gaussian are listed. In the second line, the parameters are those of a bifurcated Gaussian with one Gaussian function to fit the right-hand side, with mean value μ_1 and width σ_1, and two Gaussian functions to fit the left-hand side, with mean values μ_1 and μ_2 and widths σ_2 and σ_3.*

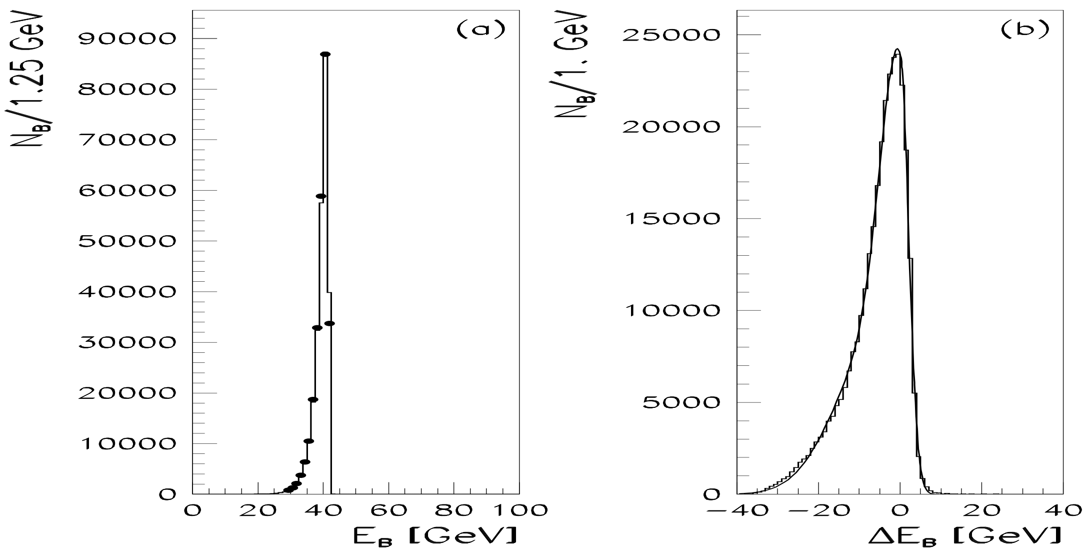

Figure 3.16: *(a) The energy of the B meson obtained from the rapidity algorithm and constrained by the centre-of-mass energy. (b) The energy resolution. The distribution is fitted with a bifurcated Gaussian consisting of one Gaussian at the right hand side and two Gaussians at the left-hand side. The parameters are summarised in table 3.3. The dots are data and the histogram is MC.*

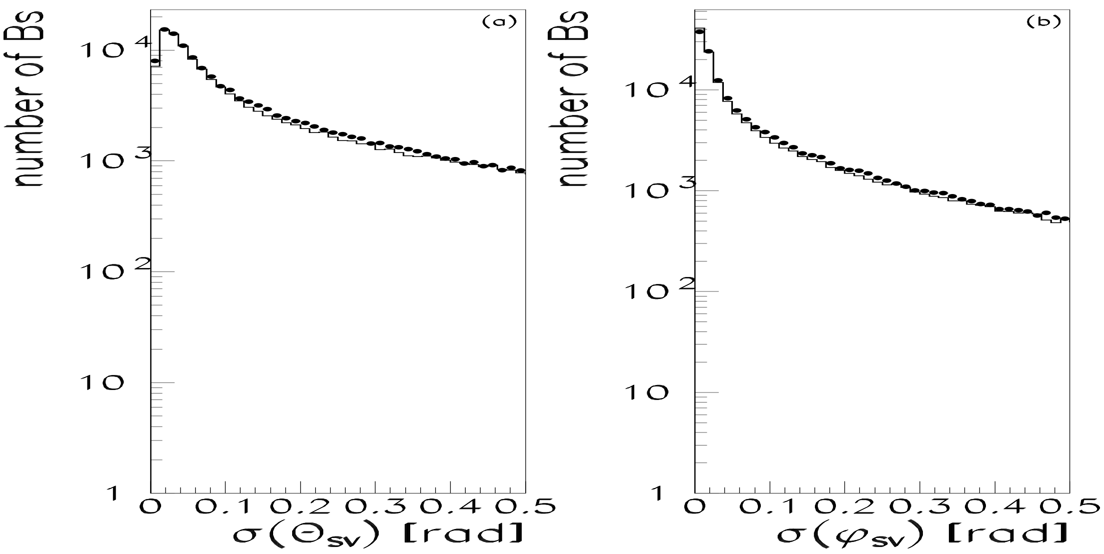

Figure 3.17: *The error distributions for θ (a) and ϕ (b) calculated by the SV method. The dots are data and the histogram is MC.*

The advantage of the constraint is the better resolution, but with the disadvantage that it is asymmetric. However, one can correct for the bias. The rapidity algorithm combined with the centre-of-mass constraint is used for the reconstruction of the B-meson energy. The energy obtained from the rapidity algorithm alone is used to determine the systematic error of that measurement.

3.4.4 B-meson direction

There are two methods, the SV method (subsection 3.4.1) and the rapidity method (subsection 3.4.2), to reconstruct the B-meson direction. These methods are independent and the weighted average can be taken.

For the SV method the errors are known through the covariance matrices,

$$(\sigma(\theta_{\mathrm{SV}}))^2 = \sum_{i=1}^{3}\sum_{j=1}^{3} \frac{\delta\theta}{\delta x_{\mathrm{p}i}}\frac{\delta\theta}{\delta x_{\mathrm{p}j}} V_{\mathrm{p}i,j} + \frac{\delta\theta}{\delta x_{\mathrm{s}i}}\frac{\delta\theta}{\delta x_{\mathrm{s}j}} V_{\mathrm{s}i,j}, \tag{3.11}$$

where $x_{\mathrm{p}i}$ are the x-, y- and z-coordinates of the primary vertex, respectively, $x_{\mathrm{s}i}$ those of the secondary vertex and V_{p} and V_{s} are the covariance matrices of the primary and secondary vertices, respectively. A similar equation is obtained for $(\sigma(\phi_{\mathrm{SV}}))^2$.

The covariance matrix of the rapidity algorithm cannot be calculated since the errors on θ, ϕ and energy of neutral particles can not be computed for individual calorimetric measurements, as they are for the charged particles. The width of a single Gaussian fit to the θ and ϕ resolutions is taken as an estimate of the errors on the direction of the rapidity method.

The θ and ϕ error distributions for data and MC of the SV method and of the weighted-average method are plotted in figures 3.17 and 3.18, respectively.

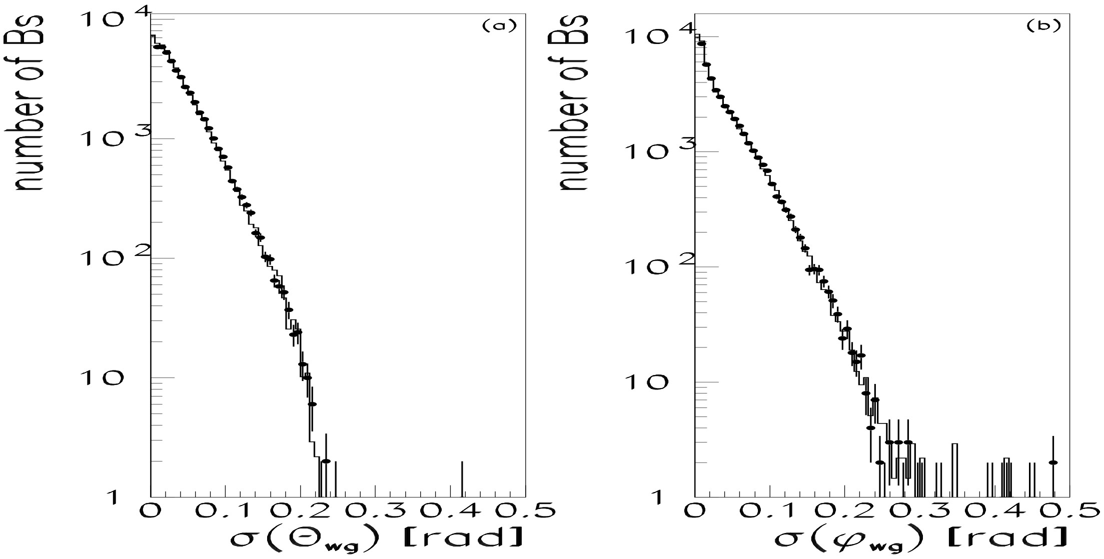

Figure 3.18: *The error distributions for θ (a) and ϕ (b) calculated by the weighting method. The dots are data and the histogram is MC.*

The SV method is more accurate (at least in ϕ), but can sometimes fail completely resulting in the large tails in figure 3.12. The rapidity algorithm is more reliable. In order to combine the good resolution with reliability, the confidence level of

$$\chi^2_\theta = \frac{(\theta_{\rm rap} - \theta_{\rm sv})^2}{\sigma^2_{\theta_{\rm rap}} + \sigma^2_{\theta_{\rm sv}}}, \tag{3.12}$$

and a similar expression for ϕ, are plotted in figure 3.19. A large peak is observed at low χ^2 probabilities. This peak is a consequence of the large tails in the SV distributions.

An improvement in resolution can be achieved with the weighted-average method by requiring the χ^2-probability to be larger than 5%. If this is not the case the rapidity method is chosen. The resulting distributions are plotted in figure 3.20. The resolution curves are fitted with a double Gaussian and the fitted parameters are summarised in table 3.2. The θ resolution is clearly better than that obtained with the SV method, but about the same as that obtained with the rapidity algorithm. The ϕ resolution is not better than that obtained with the SV method, but the tails are smaller. The ϕ resolution is better than that obtained with the rapidity algorithm.

It is difficult to decide which method is better suited for the reconstruction of the Bπ invariant mass. One could even suggest that taking a 'mix' of $\theta_{\rm rap}$ and $\phi_{\rm SV}$ is the best way to reconstruct the B-meson direction. However, when the $\mathrm{B}^{**}_{\rm u,d}$ signal is taken into account in MC, both the signal-to-noise ratio S/N and the $M_{\rm B\pi}$ resolution obtained with this 'mixing' method are inferior to those obtained by the rapidity or the weighted-average methods. As can be seen in table 3.4.4, the last two methods give about the same S/N and $M_{\rm B\pi}$ resolution. In this analysis the weighted-average method is used to reconstruct the B-meson direction and the rapidity method is used as an estimate of the systematic error due to the B-reconstruction method.

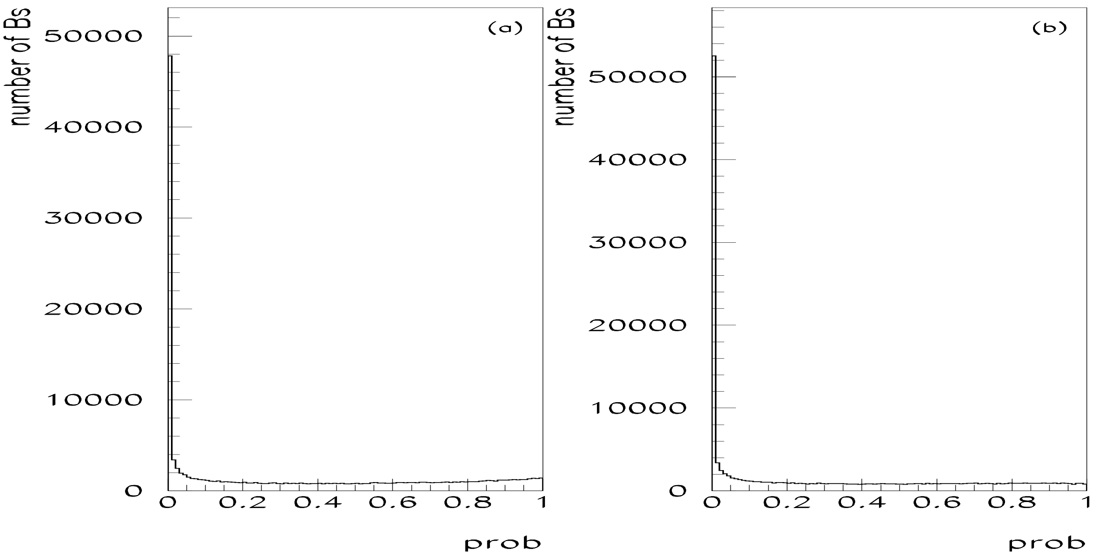

Figure 3.19: *The* χ^2 *probability distribution for* θ *(a) and* ϕ *(b) .*

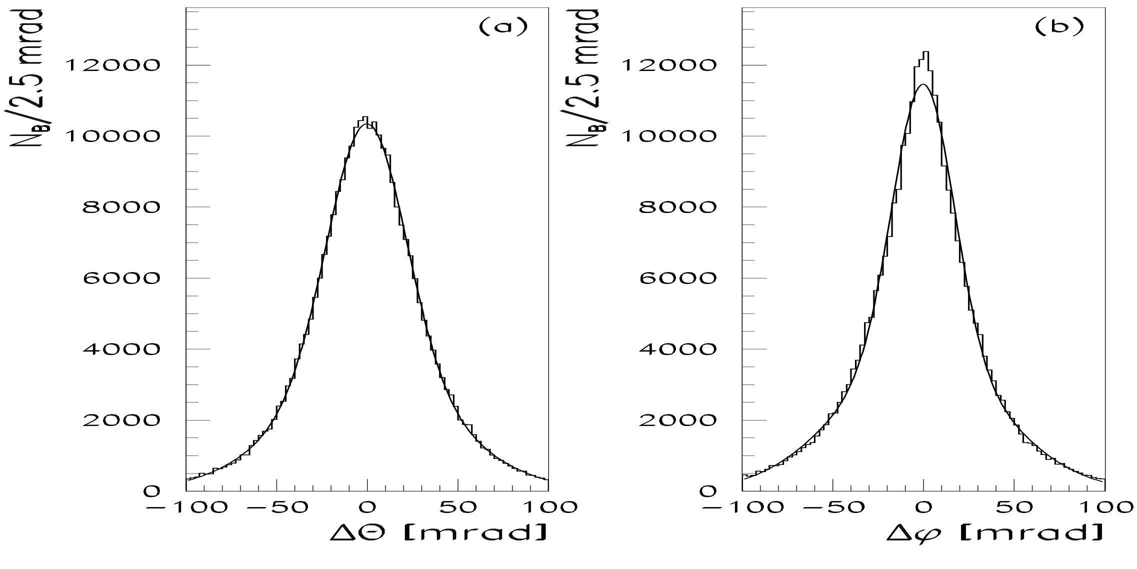

Figure 3.20: *The* θ *resolution (a) and* ϕ *resolution (b) obtained by the weighted-average method + probability criterion. Both distributions are fitted with a double Gaussian. The parameters and their errors are summarised in table 3.2.*

method	$\frac{S}{N}$[%]	$M_{B^{**}_{u,d}} - M_{B\pi}$ [GeV]
SV	8.1 ± 0.2	0.115 ± 0.006
rapidity	5.9 ± 0.1	0.090 ± 0.003
weighted	6.0 ± 0.1	0.086 ± 0.003
mix	4.3 ± 0.2	0.098 ± 0.003

Table 3.4: *The signal-to-noise ratio S/N and the $M_{B\pi}$ resolution $M_{B^{**}_{u,d}} - M_{B\pi}$ for the different reconstruction methods for the direction of the B meson.*

3.5 Invariant mass for the charged-pion channel

The $B\pi$ invariant mass is given by:

$$M_{B\pi} = \sqrt{M_B^2 + M_\pi^2 + 2E_B E_\pi - 2p_B p_\pi \cos\alpha} \quad , \tag{3.13}$$

where M_B and M_π are the masses of the B meson and the pion assumed to be known [4], E_B and p_B the B-meson energy and momentum as obtained from the reconstruction described in the previous section, E_π and p_π the pion energy and momentum of the pions selected in section 3.3, and α is the opening angle between the B meson and the pion.

The $M_{B\pi}$ distribution is plotted in figure 3.21. The MC background is formed by all $B\pi$ combinations, where the pion does not originate from the $B^{**}_{u,d}$. It is normalised to the data in the tail of the distribution ($M_{B\pi} > 6$ GeV). A signal is visible in the data above the MC background. In the next chapter the parameters of the $B^{**}_{u,d}$ resonance will be determined by fits to the distribution.

3.6 Neutral-pion selection

Neutral pions are reconstructed from their two-photon decays. The photon is reconstructed from a cluster of crystals in the BGO selected by the following criteria [74] :

- $N_{\text{crystals}} \geq 1$
- $|\cos\theta_\gamma| < 0.74$ (barrel region)
- $E_\gamma \geq 55$ MeV
- $F_{NN} > \begin{cases} 0.3413 + 0.4 \cdot E_\gamma & \text{for } E_\gamma < 0.93 \text{ GeV,} \\ 0.7133 & \text{for } E_\gamma \geq 0.93 \text{ GeV.} \end{cases}$
- if $|\phi_{TEC} - \phi_{BGO}| < 5\,\sigma_{\phi BGO}$, then $|\theta_{TEC} - \theta_{BGO}| > 5\,\sigma_{\theta BGO}$,

where N_{crystals} is the number of crystals above threshold in a 3x3 array centred on the electromagnetic shower, θ_γ is the polar production angle of the photon in the L3 system, E_γ is the photon energy summed over those crystals, F_{NN} is the output of a neural-network analysis [75]

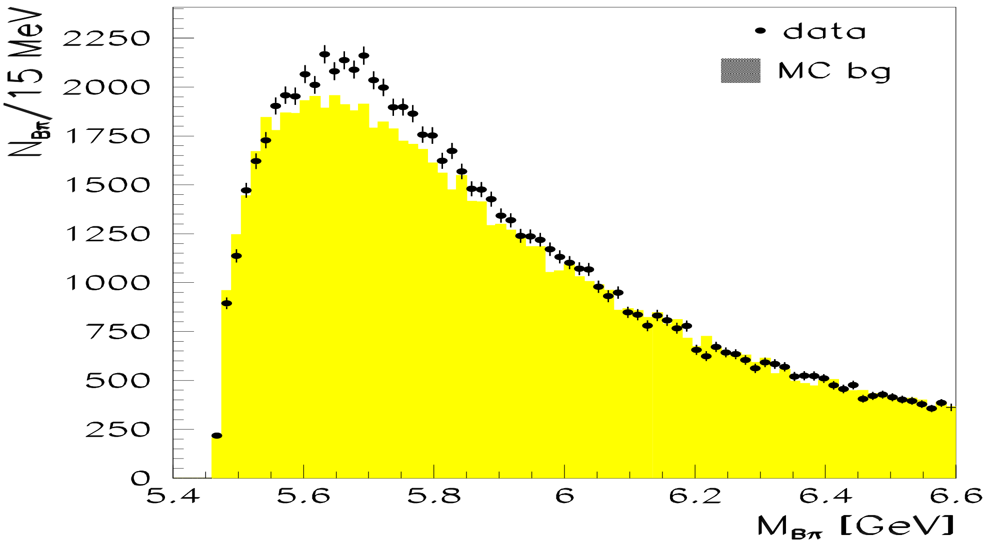

Figure 3.21: *The* Bπ *invariant-mass distribution for the charged-pion channel. The dots are data, the shaded histogram is the MC background.*

that determines the probability that the cluster comes from a photon, and the last criterion rejects BGO clusters that match a charged track and are likely to be electrons. Here, $\phi_{\rm TEC}$ and $\theta_{\rm TEC}$ are the angles of the closest charged track, $\phi_{\rm BGO}$ and $\theta_{\rm BGO}$ are the angles of the BGO cluster and $\sigma_{\phi \rm BGO}$ and $\sigma_{\theta \rm BGO}$ are the ϕ-BGO and θ-BGO resolution functions [74].

After the photon selection, photons are combined to see whether the combination can come from a π^0 according to:

- $M_{\gamma\gamma} - m_{\pi^0} \leq 3.0 \cdot \sigma_{\rm M_{\gamma\gamma}}$,

where $M_{\gamma\gamma}$ is the mass calculated from the two-photon combination, assuming both photons came from the primary vertex [7], m_{π^0} is the nominal π^0 mass, $\sigma_{\rm M_{\gamma\gamma}}$ is the error on the calculated pion mass $M_{\gamma\gamma}$. After this, a kinematic fit is performed [74,76]. The following χ^2 is minimised: $\chi^2 = (\vec{x} - \vec{x}_m)^T \vec{G}(\vec{x} - \vec{x}_m)$, subject to the constraints $\vec{F}(\vec{x}) = 0$. In this case the vector $\vec{x}_m$ contains the θ, ϕ and energy values of both photons and the primary vertex values and the constraint $F = \frac{M_{\gamma\gamma}}{m_{\pi^0}} - 1.0$ is used. The χ^2 probability, called $P_{\rm PV}$, is required to be larger than 1 %.

In figure 3.22, the reconstructed two-photon mass is plotted for all two-photon combinations. The hatched area indicates those two-photon combinations which fulfil the π^0 selection criteria and the shaded areas are the so-called sidebands, which are obtained by the requirement that $M_{\gamma\gamma} - m_{\pi^0} > 3.0 \cdot \delta_{M_{\gamma\gamma}}$ and $M_{\gamma\gamma} - m_{\pi^0} \leq 6.0 \cdot \delta_{M_{\gamma\gamma}}$. The sideband combinations will be used to examine the combinatorial background.

In table 3.6 the signal-to-noise ratio S/N, the $M_{\rm B\pi}$ resolution $M_{\rm B^{**}_{u,d}} - M_{\rm B\pi}$ and the π^{0**}efficiency ε_{π^0}, where π^{0**} is used to indicate the π^0 from the $\rm B^{**}_{u,d}$ decay, are listed for each cut.

[7] It is in fact the π^0 that originates from the primary vertex, but due to the short lifetime of the π^0 this is the same as assuming the common vertex of the two photons to be the PV.

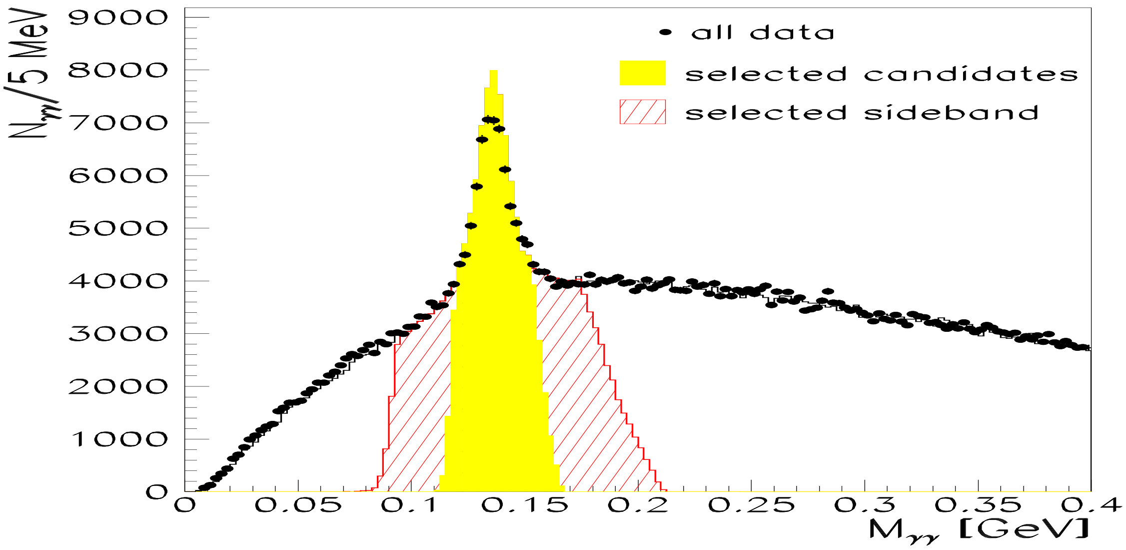

Figure 3.22: *The reconstructed π^0 mass for all two-photon combinations . Indicated are also the signal π^0 cut and the side-band cut.*

selection	$\frac{S}{N}$ [%]	$M_{B^{**}_{u,d}} - M_{B\pi}$ [GeV]	$\varepsilon_{\pi^{0**}}$
mass + PV cut	2.07	0.119	10.5
previous + E_π > 1.0 GeV	2.91	0.106	3.8
previous + 1 pure γ	2.97	0.106	2.7
mass + PV cut + E_π> 1.0 GeV + most energetic	2.99	0.102	2.7

Table 3.5: *The signal-to-noise ratio, the $M_{B\pi}$ resolution and the π^{0**} efficiency for the pion selection cuts.*

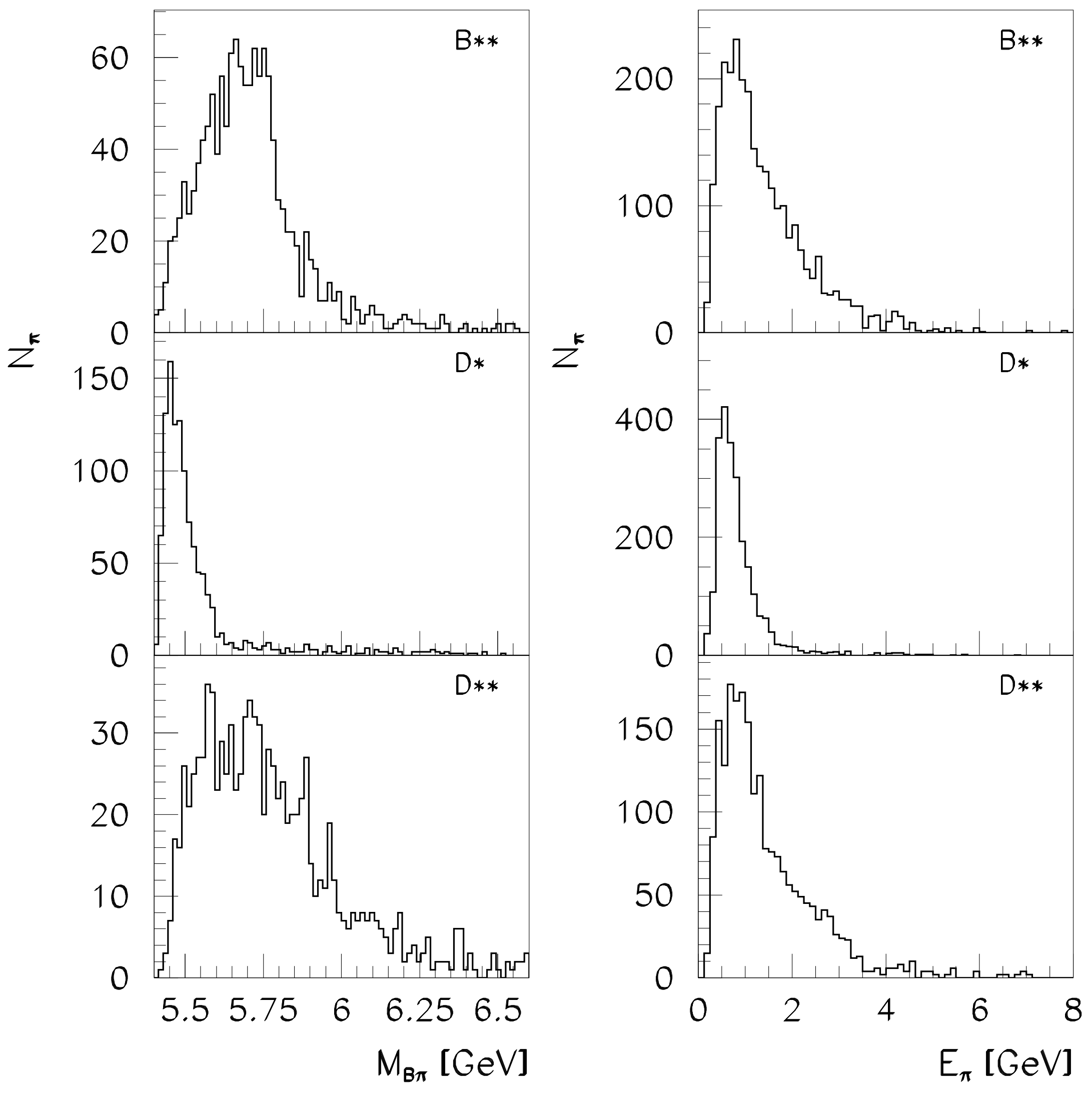

Figure 3.23: *The* $B\pi^0$ *mass distribution, where the neutral pion originates from the decay of* $B^{**}_{u,d}$, D^* *and* D^{**} *on the left-hand side and the pion energy distributions for those pions on the right-hand side.*

As in the case of the charged pions there is a contribution to the Bπ mass at low values due to D^* decays. This can be seen in figure 3.23. Contributions from K, K^{**}, D and D^{**} pions again do not appear to form resonances. When the energy of the neutral pions is plotted on the right-hand side of figure 3.23, most of the D^*-decay pions turn out to have energies smaller than 1 GeV. Therefore, π^0's are required to have an energy larger than 1 GeV to cut out most of the contamination due to D^* decay.

3.7 Invariant mass for the neutral-pion channel

The $B\pi^0$ invariant mass is calculated from eq.(3.13). In figure 3.24, the invariant-mass distribution is plotted for the neutral-pion channel. As in the case of the charged-pion channel, the MC background is normalised to the data in the tail ($M_{B\pi} > 6$ GeV) of the distribution. A signal is visible in the data above the MC background.

In figure 3.25 the invariant-mass distribution is plotted for the side bands of figure 3.22. Good agreement between the data and MC distributions is observed, not only in the tail, where the MC distribution is normalised to the data, but also in the signal area. This gives confidence that the MC background provides a good description of the real background in the data and that the enhancement observed in figure 3.24 is indeed due to π^0 decays.

3.8 B^* photon selection

To observe the decay $B^* \rightarrow B\gamma$, the same photon selection is applied as for the π^0 reconstruction. However, two additional cuts are applied. Photons are accepted if not already selected as π^0-decay candidates and if $\cos\theta^* > 0$, where θ^* is the angle of the photon with respect to the direction of the B^* transformed to the B^* rest frame.

In figure 3.26 the $\cos\theta^*$ distribution is plotted for all selected photon candidates. The total distribution peaks at $\cos\theta^* = -1$. From parity conservation in the (electromagnetic) $B^* \rightarrow B\gamma$ decay one expects the $\cos\theta^*$ distribution to be symmetric w.r.t. zero. A big part of the background is removed with the cut on $\cos\theta^*$.

In figure 3.27 the $M_{B\gamma}$ distribution is shown. The MC background is formed by all Bγ combinations where the photon does not originate from the B^*. It is normalised to the data in the tail of the distribution ($M_{B\gamma} > 5.38$ GeV). A signal is visible in the data above the MC background. In the next chapter the parameters of the B^* resonance will be determined.

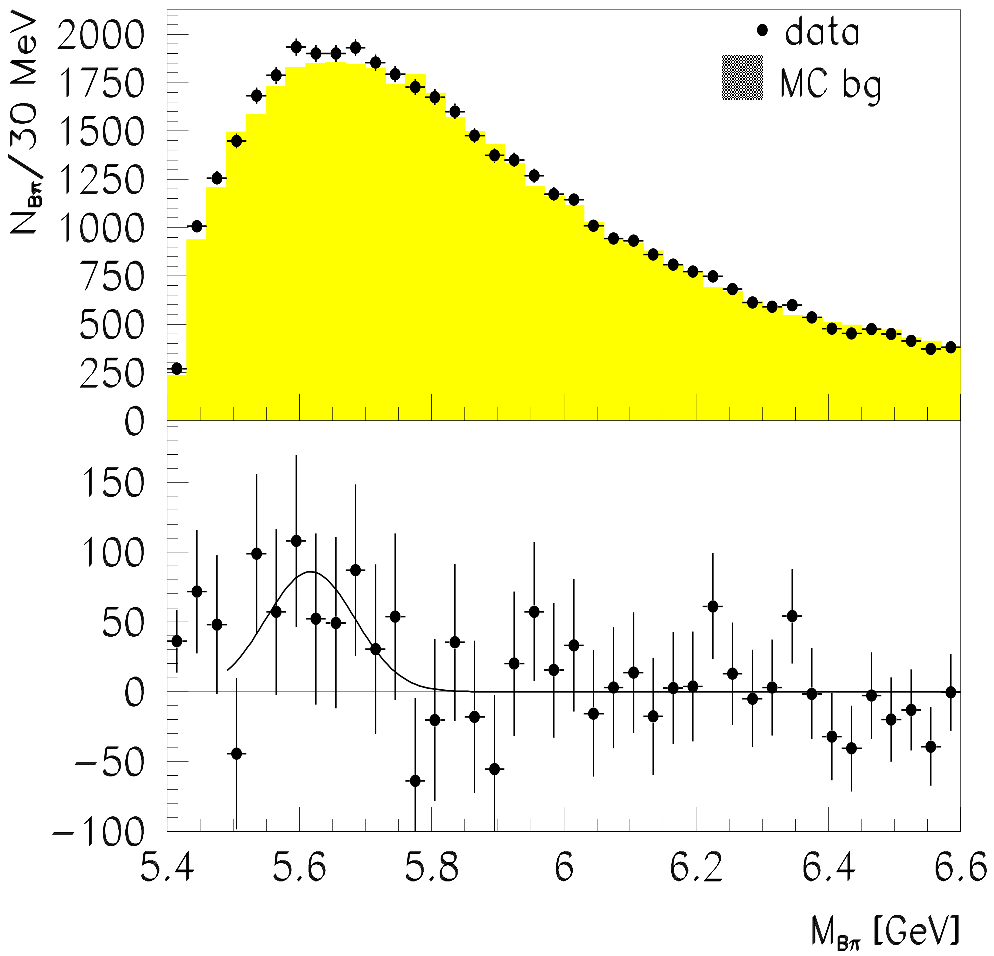

Figure 3.24: *The invariant-mass distribution for the neutral-pion channel after all cuts are performed. The dots are data and the shaded histogram is the MC background. In the bottom plot the difference between the data and the MC background is plotted.*

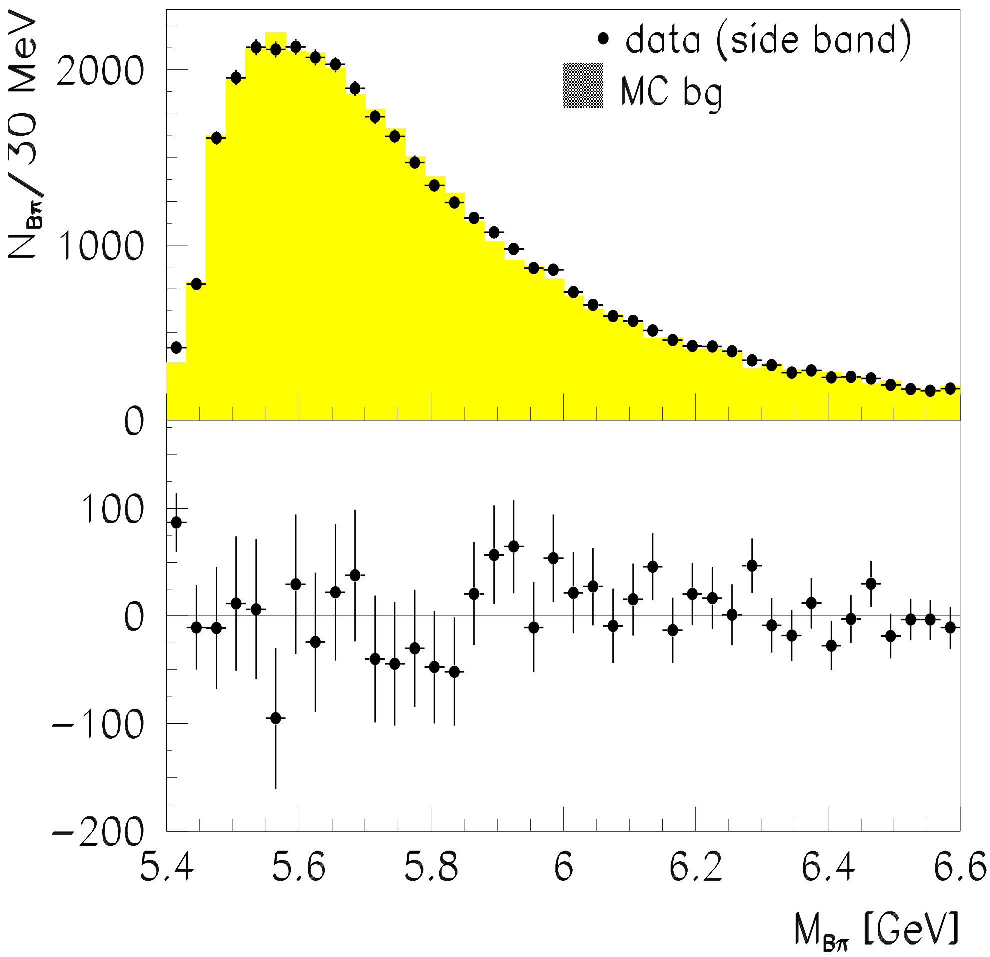

Figure 3.25: *The invariant-mass distribution for the sidebands. The dots are the data and the shaded histogram is the MC background. In the bottom plot the difference between data and MC background is plotted.*

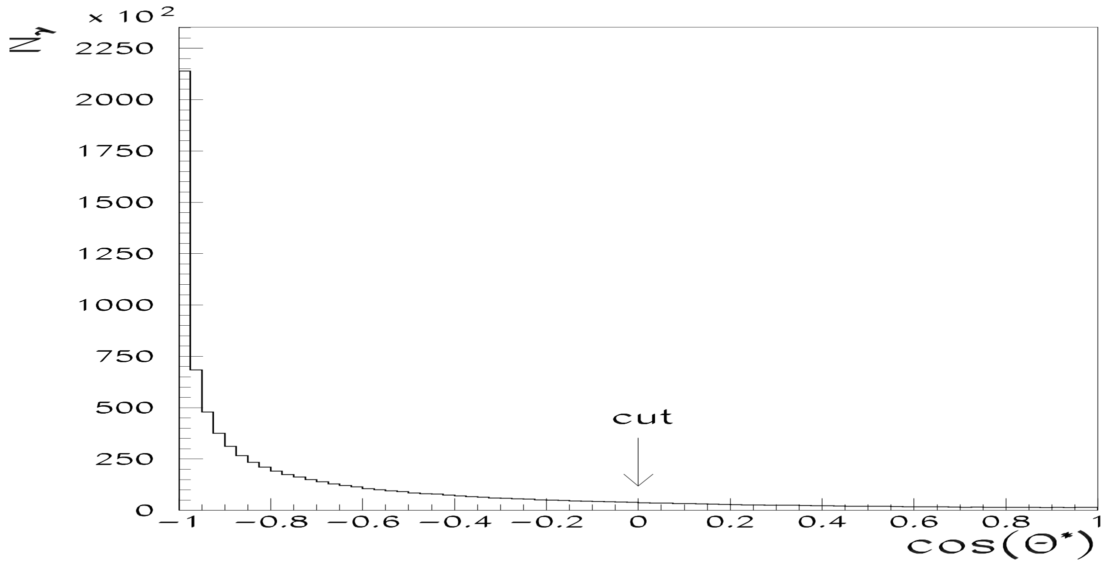

Figure 3.26: *The* $\cos\theta^*$ *distribution for all selected photons.*

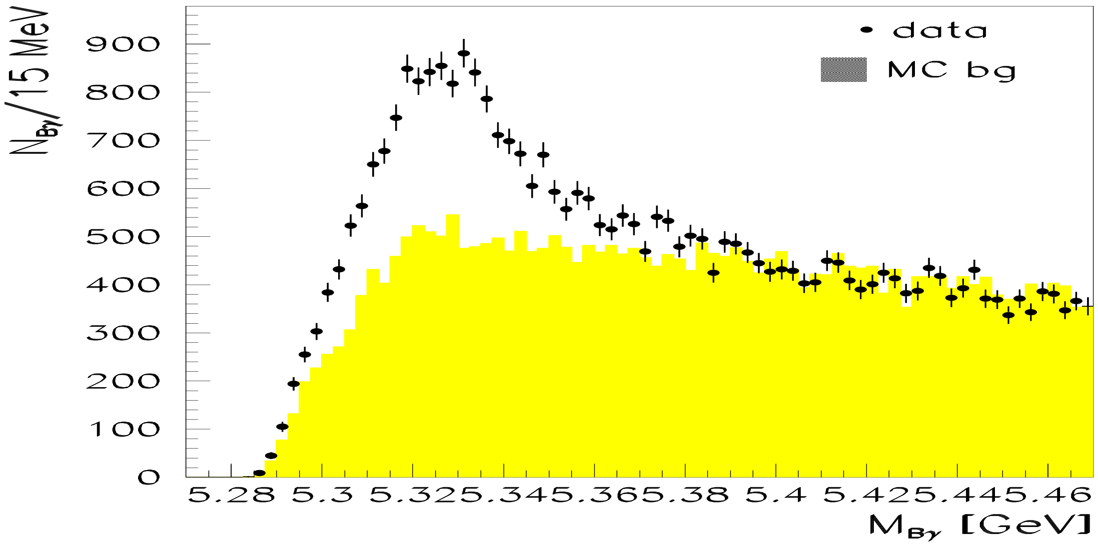

Figure 3.27: *The invariant-mass distribution for the* B^* *after all cuts are performed. The dots are data and the histogram represents the MC background.*

Chapter 4

Results

4.1 Signal extraction

Using the method described in the previous chapter, the $M_{\mathrm{B}\pi}$ distribution is obtained for $\pi^{\pm}$ and π^{0} and plotted in figures 4.1 and 4.2, respectively. Also plotted in both figures is the expected background determined from the MC as described in section 3.5. An enhancement above the MC background estimation is seen in both plots. A binned likelihood fit is used to extract the signal properties. The likelihood function is given by:

$$\mathcal{L} = \prod_i \frac{(b_i + s_i)^{d_i} \cdot e^{-(b_i+s_i)}}{d_i!}, \tag{4.1}$$

where b_i is the number of background combinations (from MC) in bin i, d_i the number of data combinations in bin i and s_i the number of signal combinations in that bin obtained with a single Gaussian function given by: $s_i = N_\mathrm{s} \frac{1}{\sqrt{2\pi\sigma}} \int_{\mathrm{bin}\, i} \exp\left[-\frac{(m_{\mathrm{B}^{**}_{\mathrm{u,d}}} - m_{\mathrm{B}\pi})}{2\sigma}\right] \mathrm{d}m_{\mathrm{B}\pi}$, where the total number of $\mathrm{B}^{**}_{\mathrm{u,d}}$, N_s, the $\mathrm{B}^{**}_{\mathrm{u,d}}$ mass, $m_{\mathrm{B}^{**}_{\mathrm{u,d}}}$ and the width of the Gaussian σ are fitted.

4.1.1 $\mathrm{B}^{**}_{\mathrm{u,d}}$ signal from the charged-pion channel

The $M_{\mathrm{B}\pi}$ distribution for $\mathrm{B}\pi^{\pm}$ combinations is plotted in figure 4.1 for the data and the smoothed MC background. The performed fit is shown as a solid line. The χ^2 of the fit is 119 for 77 degrees of freedom. The structure in the $M_{\mathrm{B}\pi}$ distribution is observed at

$$M_{\mathrm{B}^{**}_{\mathrm{u,d}}} = (5.712 \pm 0.010)\ \mathrm{GeV}. \tag{4.2}$$

with a width of

$$\sigma = (0.079 \pm 0.006)\ \mathrm{GeV}. \tag{4.3}$$

The number of $\mathrm{B}^{**}_{\mathrm{u,d}}$ decays to $\mathrm{B}^{(*)}\pi^{\pm}$ is

$$N(\mathrm{B}^{**}_{\mathrm{u,d}}) = 2926 \pm 213. \tag{4.4}$$

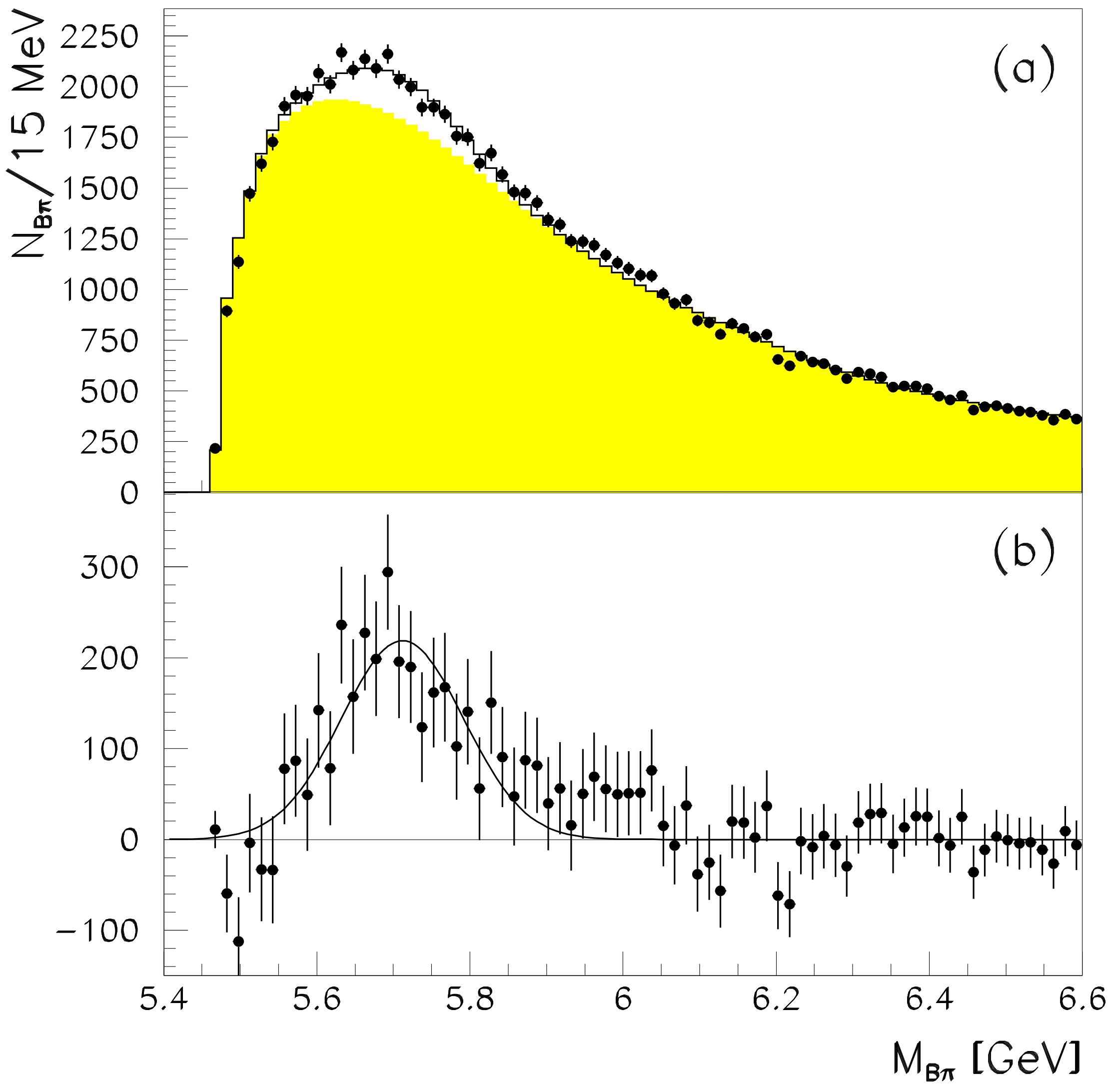

Figure 4.1: *(a) The $M_{B\pi^\pm}$ distribution. The dots are the data, the shaded histogram the MC background and the open histogram the total fit, when the signal is fitted with a single Gaussian; (b) the MC background is subtracted from the data and the signal fit is plotted.*

4.1.2 $B^{**}_{u,d}$ signal from the neutral-pion channel

In figure 4.2 the $M_{B\pi}$ distribution for $B\pi^0$ combinations is plotted for the data and the smoothed MC background. The fit is shown as a solid line. The χ^2 of the fit is 44.7 for 37 degrees of freedom. The structure is observed at

$$M_{B^{**}_{u,d}} = (5.604 \pm 0.019)\ \text{GeV}. \tag{4.5}$$

This value is lower than the $B^{**}_{u,d}$ mass obtained in the charged-pion channel of this analysis. The signal has a width of

$$\sigma = (0.082 \pm 0.026)\ \text{GeV}. \tag{4.6}$$

This value is consistent with the Gaussian width obtained in the charged-pion channel. The number of reconstructed $B^{**}_{u,d}$ decays to $B^{(*)}\pi^0$ is

$$N(B^{**}_{u,d}) = 527 \pm 156. \tag{4.7}$$

4.1.3 Resolution

The measured width found in the previous two sections is large compared to the predicted Breit-Wigner width of the narrow states and of about the same order of magnitude as the Breit-Wigner width of the broad states. This suggest that a large part of the measured width is due to the detector resolution. To get an idea of the contribution of the resolution to the measured width, each MC signal is fitted separately with a Breit-Wigner convoluted with a Gaussian. The Breit-Wigner width is fixed to the known MC value given in section 3.1. The resulting resolution is plotted in figure 4.3. In the case of the narrow resonances, a large part of the width is due to the resolution. The obtained resolution is not good enough to fit several signal shapes for the signal and to try to determine the parameters of the different resonances.

4.2 The $B^{**}_{u,d}$ production rate

4.2.1 The production rate in the charged-pion channel

The measured number of $B^{**}_{u,d}$ mesons, $N(B^{**}_{u,d})$, is related to the relative production rate of $B^{**}_{u,d}$ mesons in Z decays by the following expression:

$$N(B^{**}_{u,d}) = N_{tag}\eta_B\varepsilon_{\pi^{**}}\frac{N_{B^{**}_{u,d}}}{N_B}, \tag{4.8}$$

were N_{tag} is the number of tagged events, η_B the b purity of the sample, $\varepsilon_{\pi^{**}}$ the efficiency to select charged decay pions from $B^{**}_{u,d}$ and N_B the total number of B mesons and baryons. The pion efficiency and b purity obtained from MC are (12.6 ± 0.2) % and (85.52 ± 0.37) % , respectively, and N_{tag} = 183 068. Using these numbers, the following relative $B^{**}_{u,d}$ production rate is found to be

$$B_c = \frac{BR(Z\to b\to B^{**}_{u,d}\to B^{(*)}_{u,d}\pi^{\pm})}{BR(Z\to b)} = (14.8 \pm 1.2)\%. \tag{4.9}$$

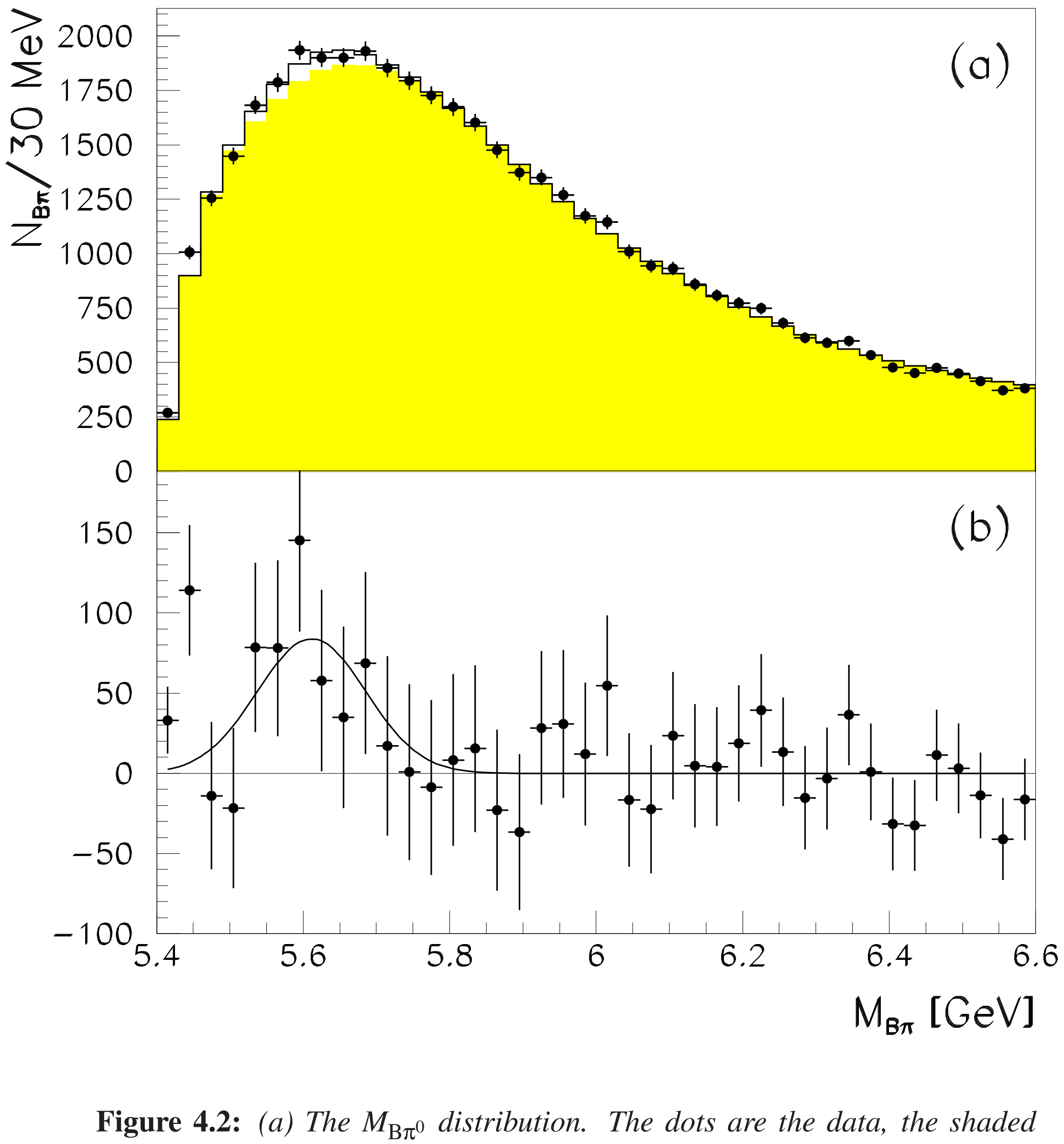

Figure 4.2: *(a) The $M_{B\pi^0}$ distribution. The dots are the data, the shaded histogram is the MC background and the open histogram the total fit when the signal is fitted with one Gaussian; (b) the background is subtracted from the data and the signal fit is plotted.*

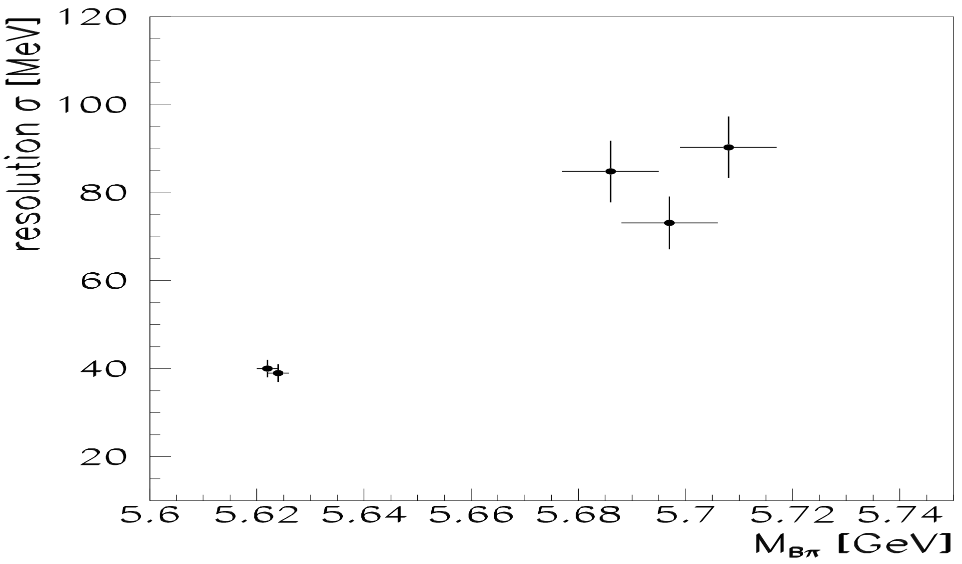

Figure 4.3: *The resolution obtained from a Breit-Wigner convoluted with a Gaussian as a function of the measured Bπ mass.*

4.2.2 Production rate in the neutral-pion channel

For the neutral pion channel an expression similar to 4.8 can be written down with $\varepsilon_{\pi^{**}}$ replaced by ε_{π^0} and $N(\mathrm{B}^{**}_{\mathrm{u,d}})$ obtained from the neutral-pion fit. The pion efficiency obtained from MC is $(3.8 \pm 0.1)\%$. With these numbers the following relative $\mathrm{B}^{**}_{\mathrm{u,d}}$ production rate is found to be

$$B_{\mathrm{n}} = \frac{\mathrm{BR}(\mathrm{Z}{\to}\mathrm{b}{\to}\mathrm{B}^{**}_{\mathrm{u,d}}{\to}\mathrm{B}^{(*)}_{\mathrm{u,d}}\pi^0)}{\mathrm{BR}(\mathrm{Z}{\to}\mathrm{b})} = (8.9 \pm 2.5)\%. \tag{4.10}$$

4.2.3 Total $\mathrm{B}^{**}_{\mathrm{u,d}}$ production rate

Isospin symmetry predicts that, for two-body decays to pions, 2/3 of the $\mathrm{B}^{**}_{\mathrm{u,d}}$ decays are into $\pi^{\pm}$ with the remaining 1/3 decaying to π^0. In this analysis, for the first time, both the charged- and neutral-pion channels were measured. Their relative production ratio can be combined by minimising the following χ^2, which imposes the 1:2 decay ratio:

$$\chi^2(x) = \frac{(2/3x - B_{\mathrm{c}})^2}{\sigma(B_{\mathrm{c}})^2} + \frac{(1/3x - B_{\mathrm{n}})^2}{\sigma(B_{\mathrm{n}})^2} \tag{4.11}$$

where, x is the total production ratio, B_{c} and B_{n} are the production ratio into the charged and neutral channel, respectively, and $\sigma(B_{\mathrm{c}})$ and $\sigma(B_{\mathrm{n}})$ are the errors on the production ratio into the charged and neutral channel, respectively. This results in a value of $\mathrm{BR}(\mathrm{b} \to \mathrm{B}^{**}_{\mathrm{u,d}})$ = (22.4 $\pm$ 1.8) % for the total production ratio. The value of the χ^2 is 0.2 for 1 dof. So, the data are in good agreement with the isospin-symmetry hypotheses.

The total $B^{**}_{u,d}$ production rate of BR($b \rightarrow B^{**}_{u,d}$)= (23.7 ± 2.8)% , obtained by simply adding the results of the charged- and neutral pion- channels, compares well with the result obtained by imposing isospin symmetry.

In order to compare the results with other experiments, one should actually calculate the ratio of the number of $B^{**}_{u,d}$ events to the number of $B_{u,d}$ events. Taking into account that about 10% of the b events are baryons and about 12 % are B_s, a production ratio of $\frac{BR(b\rightarrow B^{**}_{u,d})}{BR(b\rightarrow B_{u,d})}$ = (29.9 ± 3.5)% is obtained. This value is consistent with the other LEP experiments [37–40].

4.3 Results on $B^* \rightarrow B\gamma$

4.3.1 Signal fit of the B^*

The fit of the B^* signal is performed in the same way as that of the $B^{**}_{u,d}$. In figure 4.4 data, MC background and fit results are plotted. The χ^2 of the fit is 170 for 77 degrees of freedom. The structure is observed at:

$$M_{B\gamma} = (5.3254 \pm 0.0007)\ \text{GeV}, \tag{4.12}$$

This gives a mass splitting $(M_{B^*} - M_B)$ of (46.5 ± 0.7) MeV. This value is in agreement with experimental results obtained by other experiments including L3. The Gaussian has a width of:

$$\sigma = (15.7 \pm 0.4)\ \text{MeV}. \tag{4.13}$$

The number of reconstructed B^* decays to $B\gamma$ is:

$$N(B^*) = 5712 \pm 137. \tag{4.14}$$

4.3.2 The $B^* \rightarrow B\gamma$ production rate

The measured number of B^* mesons, $N(B^*)$, is related to the relative production rate of B^* mesons in Z decays by the following expression:

$$N(B^*) = N_{tag}\eta_B\varepsilon_\gamma \frac{N_{B^*}}{N_{B^*} + N_B}, \tag{4.15}$$

with ε_γ the efficiency to select B^* decay photons, N_{tag} the number of tagged events and η_B the b purity of the sample. The photon efficiency and b purity, both obtained from MC, are ε_γ = (5.0 ± 0.2)% and η_B = (85.52 ± 0.37)%, respectively and N_{tag} = 183 068. With these numbers the following relative B^* production rate is found to be

$$\frac{BR(Z\rightarrow b\rightarrow B^*\rightarrow B\gamma)}{BR(Z\rightarrow b)} = (72.7 \pm 3.3)\%. \tag{4.16}$$

This value is consistent with the other experimental results [43–49].

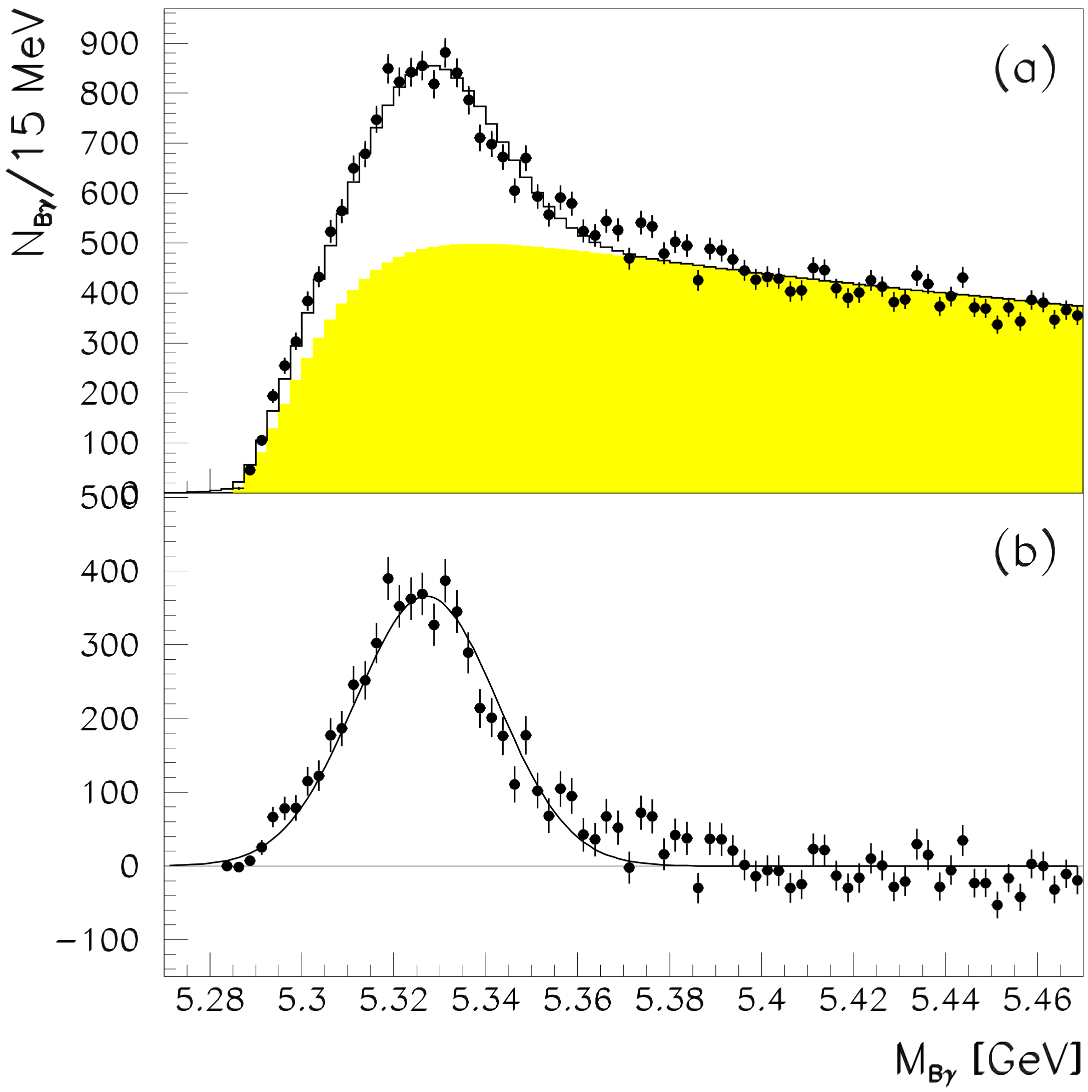

Figure 4.4: *(a) The $M_{B\gamma}$ distribution. The dots are the data. The shaded histogram the MC background and the open histogram the total fit when the signal is fitted with one Gaussian; (b) the background is subtracted from the data and the signal fit is plotted.*

Chapter 5

Systematic errors

Systematic errors may arise from uncertainties in the the event selection, in the reconstruction method and in the background. The uncertainties due to the selections are estimated by varying the cut values within reasonable values. The maximum deviation of the measurement obtained within this range is taken as the contribution to the total systematic error of the measurement due to this cut.

Furthermore, there arises an uncertainty due to the reconstruction method used for the B meson. Therefore, the analysis is repeated with the rapidity method to reconstruct the B-meson properties. The difference of these results with the those from the weighted-average method is taken as a measure of the uncertainty due the the B-meson reconstruction.

Finally, there is a contribution to the systematic error due to the uncertainty in the background shape. To estimate the uncertainty, two factors are considered. First, instead of using the MC background distribution as an estimate of the background, a threshold function is used. The results obtained this way are compared with those where the MC background was used. Secondly, the fragmentation parameter in the MC is varied within its estimated errors. The MC background distribution thus obtained is used to determine the signal. The results obtained this way are compared with those of the original MC background distribution where the default MC parameters were used.

5.1 Charged-pion channel

In the charged-pion case, the cut on the pion energy, the b-purity cut, the $L/\sigma(L)$ cut and the cut on the probability that the particle comes from the PV were varied. The influence on the Bπ mass, width and branching ratio are plotted in figure 5.1, 5.2 and 5.3, respectively. The contributions to the total systematic error are listed in table 5.1.

When the analysis is redone with the rapidity algorithm to reconstruct the B meson, a $\mathrm{B}^{**}_{\mathrm{u,d}}$ mass of 5.698 ± 0.008 GeV, a width of 0.076 ± 0.006 GeV and a number of signal events of 2970 ± 218 is obtained. This uncertainty mainly affects the mass of the signal. The contribution to the systematic error due to the reconstruction method of the B properties is listed in line 5 of table 5.1.

In order to get an idea of the systematic error due to the uncertainty in the background, one can try to fit the background. An attempt is made with a threshold function, $F(x) = (x - p_1)^{p_2} e^{(p_3(x-p_1)+p_4(x-p_1)^2+p_5(x-p_1)^3+p_6(x-p_1)^4)}$, where x is the Bπ mass and the

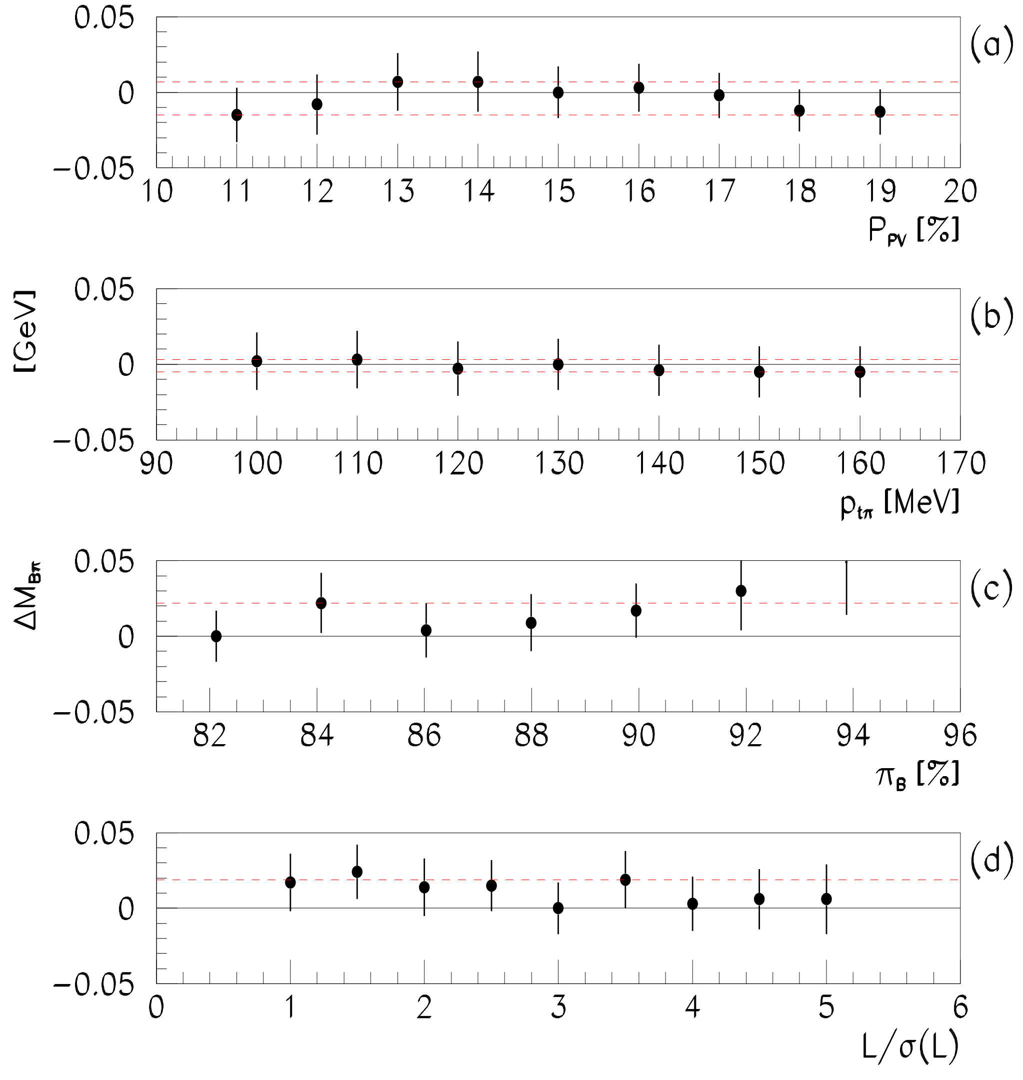

Figure 5.1: *Change in $B\pi^{\pm}$ mass as a function of: (a) the cut on the probability of a particle to come from the PV , (b) the cut on the pion energy E_{π}, (c) the btag cut (expressed in the corresponding purity values) and (d) the cut on $L/\sigma(L)$.*

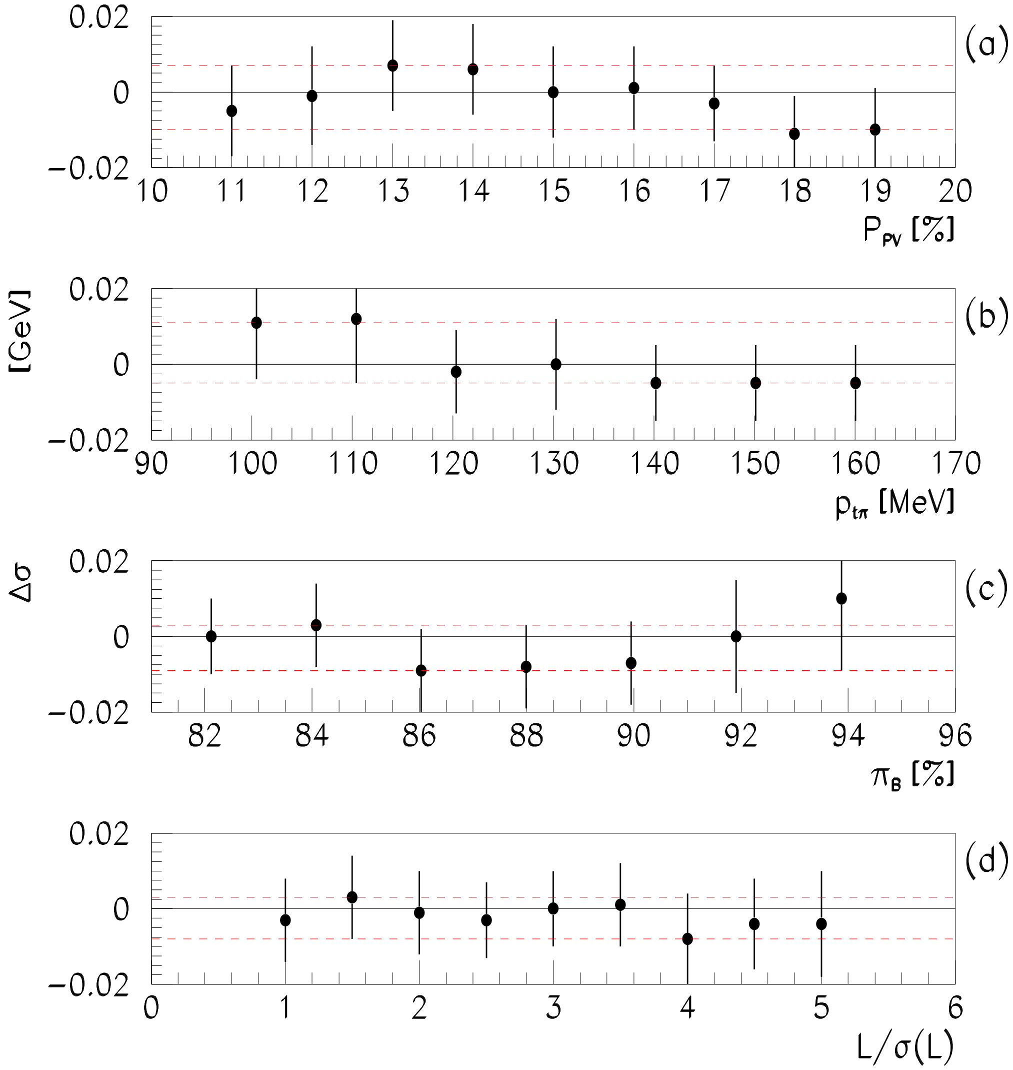

Figure 5.2: *Change in width of the signal of the charged-pion channel as a function of: (a) the cut on the probability of a particle to come from the PV , (b) the cut on the pion energy E_π, (c) the btag cut (expressed in the corresponding purity values) and (d) the cut on $L/\sigma(L)$.*

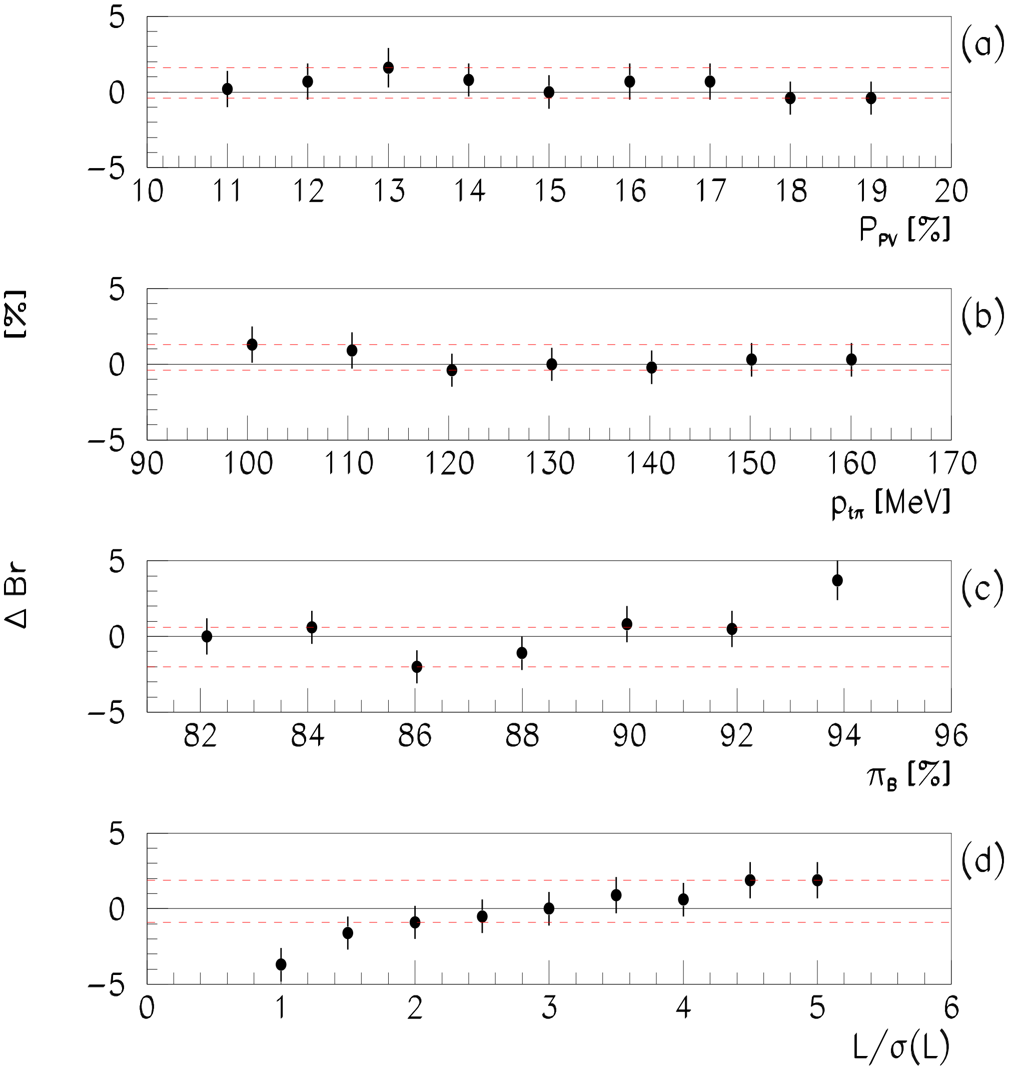

Figure 5.3: *Change in branching ratio of the charged-pion channel as a function of: (a) the cut on the probability of a particle to come from the PV , (b) the cut on the pion energy E_π, (c) the btag cut (expressed in the corresponding purity values) and (d) the cut on $L/\sigma(L)$.*

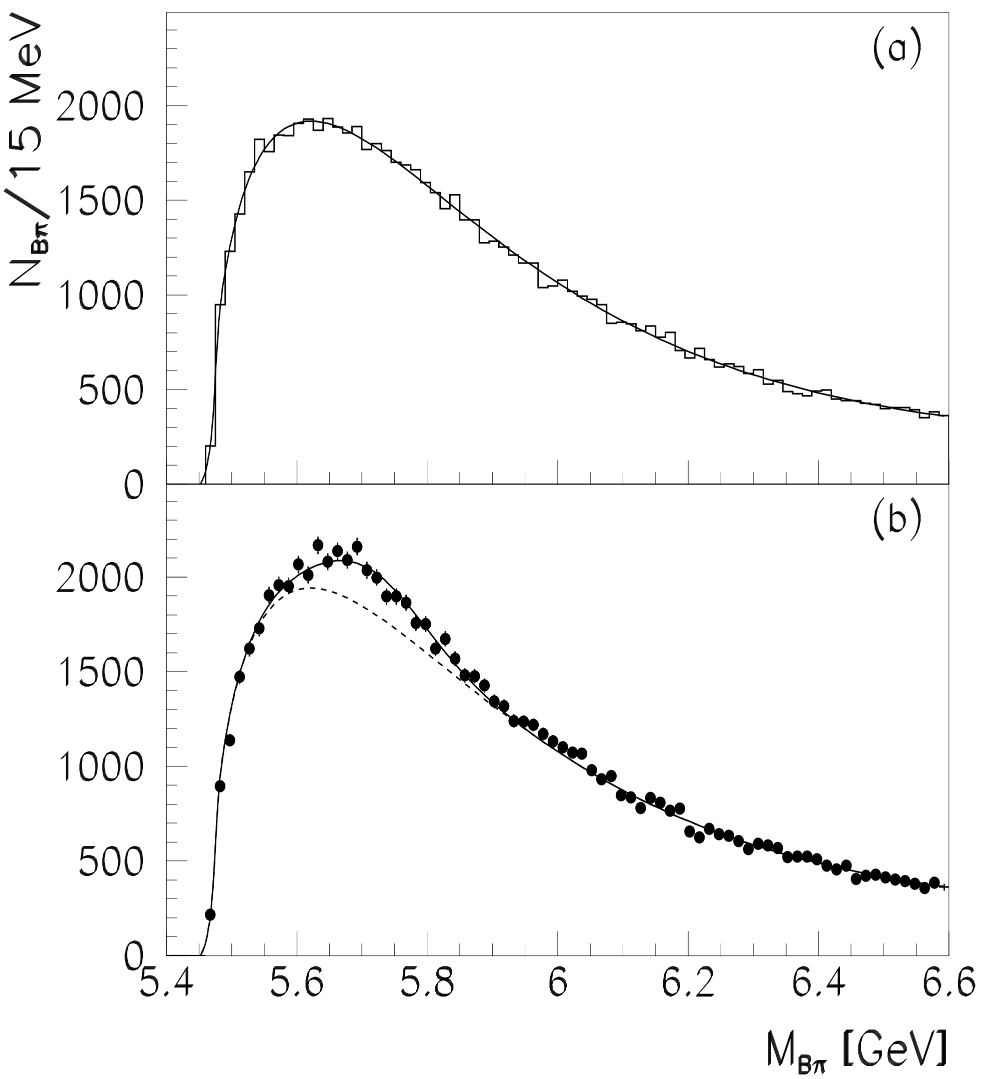

Figure 5.4: *(a) The MC $M_{\mathrm{B}\pi^{\pm}}$ background distribution fitted with the threshold function $F(x)$ and (b) The $M_{\mathrm{B}\pi^{\pm}}$ distribution. The dots are data and the dotted line is the threshold function fitted to the MC background. The signal is fitted with a simple Gaussian function. The solid line is the total fit.*

error source	$M_{B\pi}$ [GeV]	σ [GeV]	Br[%]
b purity (82-86)%	+0.022 -0.0	+0.003 -0.009	+0.6 -2.0
$L/\sigma(L)$ cut (2.0-5.0)	+0.019 -0.0	+ 0.003 -0.008	+1.9 -0.9
$p_\perp\pi$ cut (0.080-0.170) GeV	+0.003 - 0.005	+0.011 -0.005	+1.3 -0.4
P_{PV} cut (11-19) %	+0.007 -0.015	+0.007 -0.010	+1.6 -0.4
B reco method	$\pm$ 0.014	$\pm$ 0.003	$\pm$ 0.2
bg shape uncertainty 1	$\pm$ 0.005	$\pm$ 0.001	$\pm$ 0.3
bg shape uncertainty 2	+0.001 -0.008	+0.005 -0.001	$\pm$ 1.9
total	+0.034 -0.023	+0.015 -0.016	+3.5 -3.0

Table 5.1: *The systematic errors on the B$\pi\pm$ mass, width and branching ratio due to event selection and use of different methods for the signal fit.*

parameters p_1 through p_6 are determined by a fit to the MC background. As can be seen in figure 5.4(a), this function fits the MC background distribution well in the signal region. The fit to the data is shown in figure 5.4(b) . A simple Gaussian is used for the signal. In this case, a $B^{**}_{u,d}$ mass of 5.717 $\pm$ 0.008 GeV is obtained, with a width of 0.078 $\pm$ 0.005 GeV and a number of signal events of 2982 $\pm$ 208. The contribution to the systematic error due to the uncertainty in the background shape is listed in line 6 of table 5.1.

Another contribution to the uncertainty in the background shape is the uncertainty in the MC parameters. The so-called fragmentation parameter ε_b is considered to be the most important cause for the uncertainty in this analysis. The value used in the simulation is -0.0035 [77]. However, ε_b itself is not a measurable quantity. Usually $x_E = E_{hadron}/E_{beam}$ is used, where E_{hadron} is the generated b-hadron energy and E_{beam} is the beam energy. The choice of ε_b results in a mean normalised hadron energy $<x_E>$ of (0.70 ± 0.02) [78]. The variation of x_E within its errors corresponds to a variation of ε_b from -0.0018 to -0.0065. The correspondingly varied x_E distributions are compared on the generator level with the original one. The ratio of the new and the original distribution is used to reweight the MC at the detector level. The reweighted MC background distribution thus obtained is used to determine the new $B^{**}_{u,d}$ signal. The difference with the results obtained with the original MC background is taken as an estimate of the uncertainty due to the background shape. It is listed in line 7 of table 5.1. This mainly affects the branching ratio.

5.2 Neutral-pion channel

For the neutral-pion channel, the cut on the pion energy, the b-purity cut, the $L/\sigma(L)$ cut, the π^0 mass cut and the cut on the probability that the particle comes from the PV were varied. These variations for the Bπ mass, width and number of signal events are plotted in figure 5.5, 5.6 and 5.7, respectively. In table 5.2 the contributions to the total systematic error are listed for the π^0 channel.

When the analysis is redone with the rapidity algorithm to reconstruct the B meson, a $B^{**}_{u,d}$ mass of 5.603 $\pm$ 0.026 GeV, a width of 0.083 $\pm$ 0.030 GeV and a number of signal events of 535 $\pm$ 158 is obtained. The contribution to the systematic error due to the reconstruction

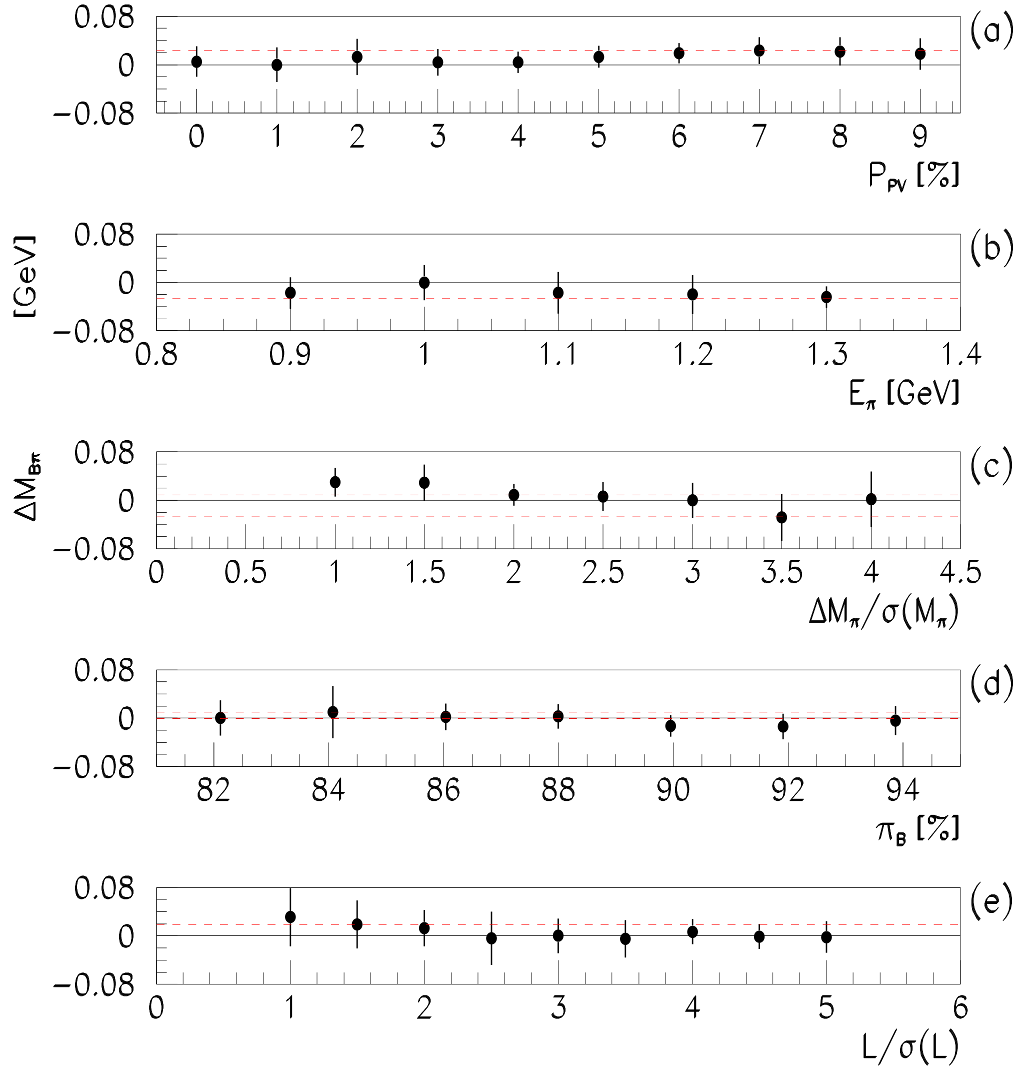

Figure 5.5: *Change in $B\pi^0$ mass as a function of: (a) the cut on the probability of a particle to come from the PV , (b) the cut on the pion energy E_π, (c) the cut on the reconstructed π^0 mass, (d) the btag cut (expressed in the corresponding purity values) and (e) the cut on $L/\sigma(L)$.*

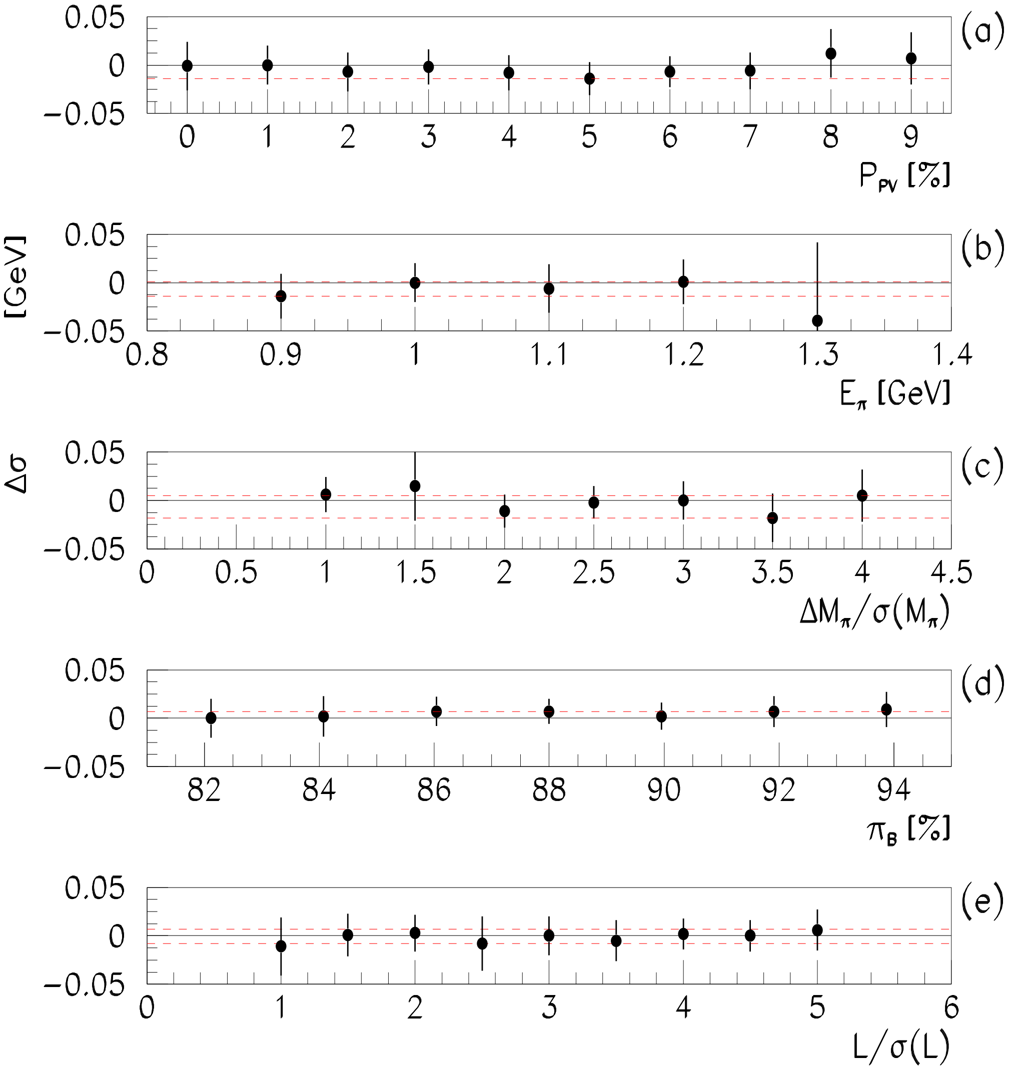

Figure 5.6: *Change in width of the signal of the neutral-pion channel as a function of: (a) the cut on the probability of a particle to come from the PV , (b) the cut on the pion energy E_π, (c) the cut on the reconstructed π^0 mass, (d) the btag cut (expressed in the corresponding purity values) and (e) the cut on $L/\sigma(L)$.*

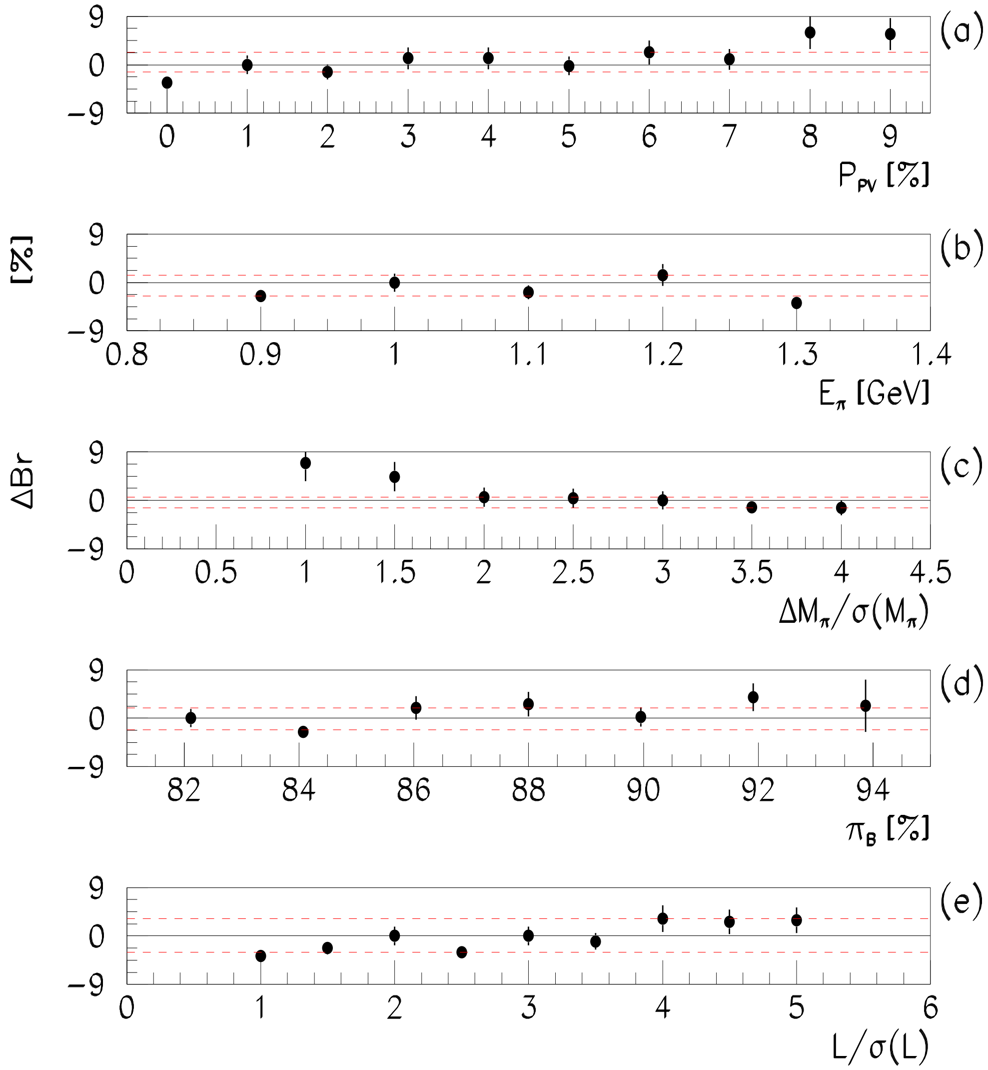

Figure 5.7: *Change in branching ratio of the neutral-pion channel as a function of: (a) the cut on the probability of a particle to come from the PV , (b) the cut on the pion energy E_π, (c) the btag cut (expressed in the corresponding purity values) and (d) the cut on $L/\sigma(L)$.*

error source	$M_{B\pi}$ [GeV]	σ [GeV]	Br[%]
b purity (82-86) %	+0.010 -0.001	+0.007 -0.0	+1.9 -2.2
$L/\sigma(L)$ cut (1.5-5.0)	+0.019 -0.005	+ 0.007 -0.008	+3.2 -3.0
E_π cut (0.9-1.2) GeV	+0.00 - 0.027	+0.001 -0.014	+1.4 -2.5
P_{PV} cut (1-7) %	+0.023 -0.0	+0.0 -0.014	+2.3 -1.3
π^0 mass cut (2.0-4.0)	+0.009 -0.027	+0.005 -0.018	+0.6 -1.4
B reco method	$\pm$ 0.001	$\pm$ 0.001	$\pm$ 0.1
bg shape uncertainty 1	$\pm$ 0.007	$\pm$ 0.014	$\pm$ 1.0
bg shape uncertainty 2	+0.027 -0.010	$\pm$ 0.041	$\pm$ 2.8
total	+0.041 -0.048	+0.045 -0.051	+5.5 -5.7

Table 5.2: *The systematic errors on the $B\pi^0$ mass, width and branching ratio due to event selection and use of different methods for the B reconstruction and uncertainty in the background shape.*

method of the B properties is listed in line 6 of table 5.2.

The background is fitted with the same threshold function as was used for the charged-pion channel (see previous section). The background fit is plotted in figure 5.8(a). The fit to the data is shown in figure 5.8(b). A simple Gaussian is used for the signal fit. In this case, a $B^{**}_{u,d}$ mass of 5.597 ± 0.026 GeV is obtained, with a width of 0.068 ± 0.031 GeV and a number of signal events of 469 ± 160. This uncertainty mainly affects the width of the signal. The contribution to the systematic error due to the uncertainty in the background shape is listed in line 7 of table 5.2.

Another contribution in the background shape is the uncertainty in the MC parameters. The fragmentation parameter ε_b is varied as described in the previous section. The contributions to the systematic error is listed in line 8 of table 5.2.

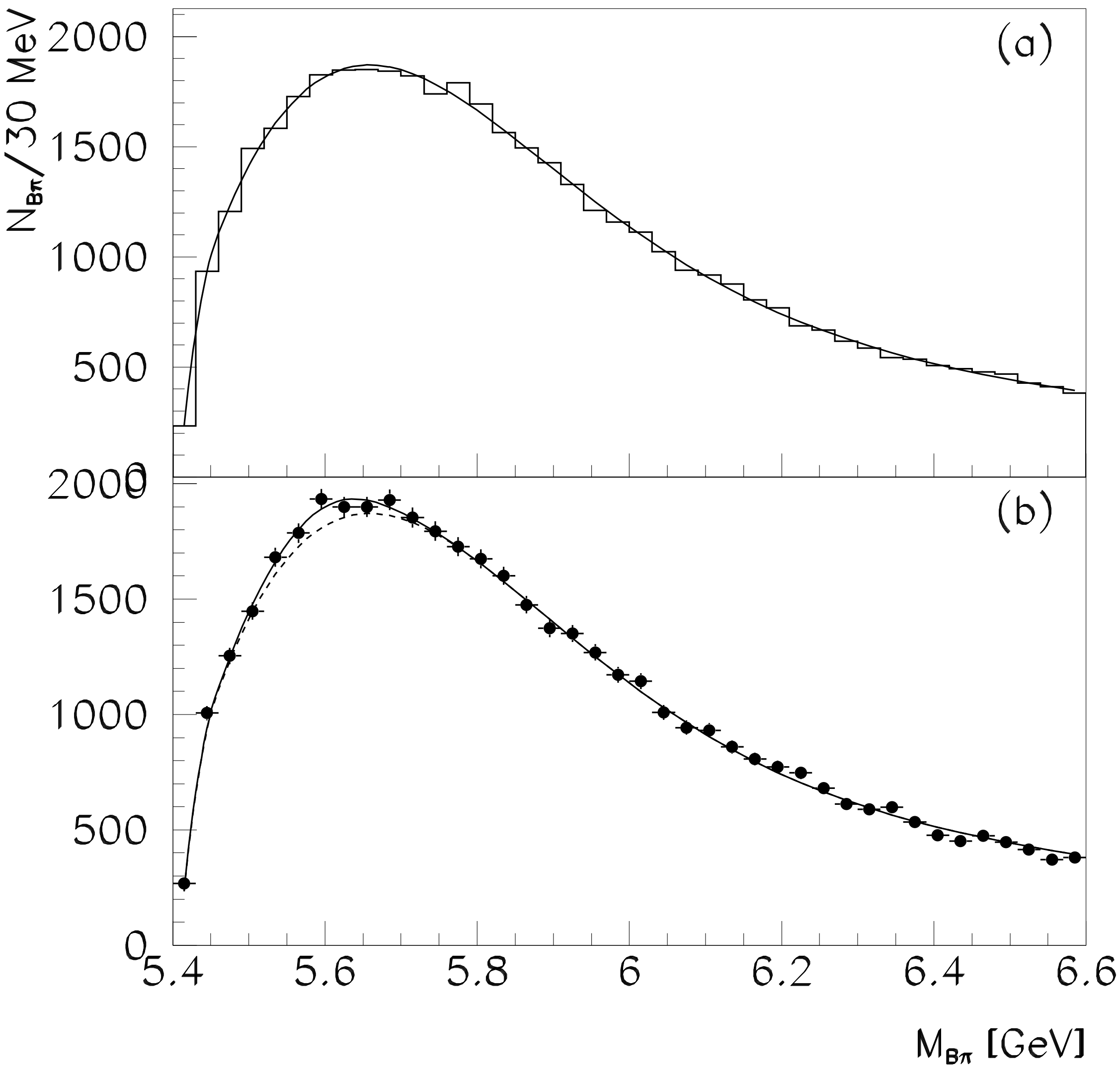

Figure 5.8: *(a) The MC $M_{B\pi^0}$ background distribution fitted with the threshold function $F(x)$ and (b) the $M_{B\pi^0}$ distribution.The dots are data and the dotted line is the threshold function fitted to the MC background. The signal is fitted with a simple Gaussian function. The solid line is the total fit.*

Chapter 6

Conclusions

Combining the results obtained in chapter 4 with the systematic uncertainties of chapter 5, the $B^{**}_{u,d}$ mass for the charged-pion channel is : $M_{B^{**}_{u,d}}$ = (5.712 ± 0.010 +0.034 -0.023) GeV and that for the neutral-pion channel is : $M_{B^{**}_{u,d}}$ = (5.604 ± 0.019 +0.041 -0.048) GeV. In figure 6.1 the values for the $B^{**}_{u,d}$ mass obtained in this analysis are compared to those obtained by the other LEP experiments. The results from the charged-pion channel are compatible with the results of the other LEP experiments. For the first time, the π^0-channel (not measured by the other experiments) can now be compared to the results of the $\pi^{\pm}$-channel. The $B^{**}_{u,d}$ mass obtained from the π^0-channel lies 2.3 standard deviations below the average mass of the $\pi^{\pm}$-channel. Heavy Quark Effective Theory predicts a mass of 5.767 and 5.755 GeV for the narrow states B_2^* and B_1, respectively. The masses of the broad states can not (yet) be well predicted, but have been assumed to lie about 100 MeV lower.

The widths of (0.079 ± 0.006 +0.015 - 0.016) and (0.082 ± 0.026 +0.045 - 0.051) obtained in the charged and neutral-pion channels, respectively, are compatible within errors (deviation is 0.05 σ). In both cases, the width is too large to be due only to the two narrow $B^{**}_{u,d}$ states. For the charged-pion channel, this is in agreement with the results obtained by the other LEP experiments.

In the charged-pion channel a relative production rate of (14.8 ± 1.2 +3.5 -3.0)% was measured, in the neutral-pion channel of (8.9 ± 2.5 +5.6 -5.8) %. When both rates are added, a total $B^{**}_{u,d}$ production rate BR($b \to B^{**}_{u,d} \to B\pi$) of (23.7 ± 2.8 ± 6.5) % is obtained. With about 10 % of the b-events being due to baryons and about 12 % due to B_s, a total production rate $\frac{BR(b \to B^{**}_{u,d} \to B\pi)}{BR(b \to B_{u,d})}$ of (29.9 ± 3.5 ± 8.2) % is obtained. As can be seen in figure 6.2, this value compares well to that of the other LEP experiments

Assuming isospin symmetry, a total production rate BR($b \to B^{**}_{u,d} \to B\pi$) of (22.4 ± 1.8 ± 6.3)% is obtained. This compares well with the value obtained by the sum of the charged- and the neutral-pion channel.

Since the different states of the $B^{**}_{u,d}$ cannot be separated, no conclusion can be drawn on their relative production rates.

For completeness, also the B^* signal was measured. A $B^* - B$ mass splitting of (46.5 ± 0.7) MeV was obtained, which is in agreement with the values obtained by other experiments as can be seen in figure 6.3. A production rate BR($b \to B^* \to B\gamma$) of (72.7 ± 3.3) % is measured, also in agreement with other measurements, as can be seen in figure 6.4.

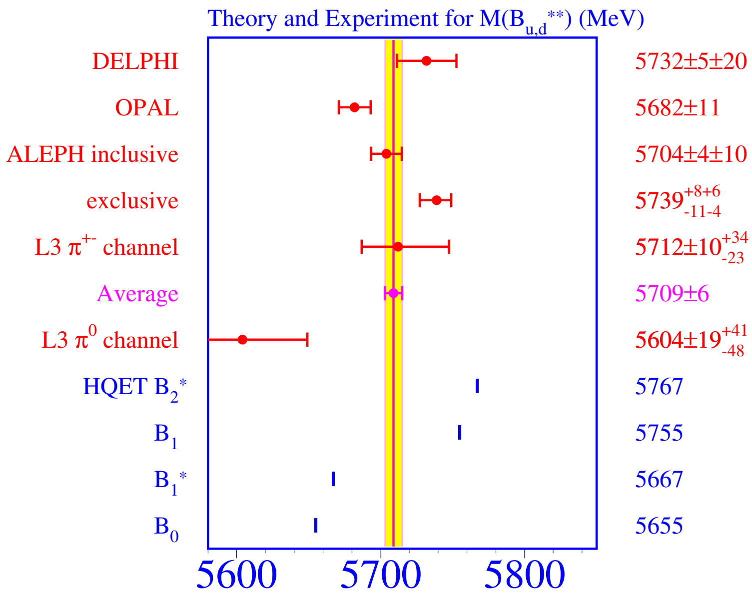

Figure 6.1: *A comparison between the* LEP *measurements of the* $\mathrm{B}^{**}_{\mathrm{u,d}}$ *mass.*

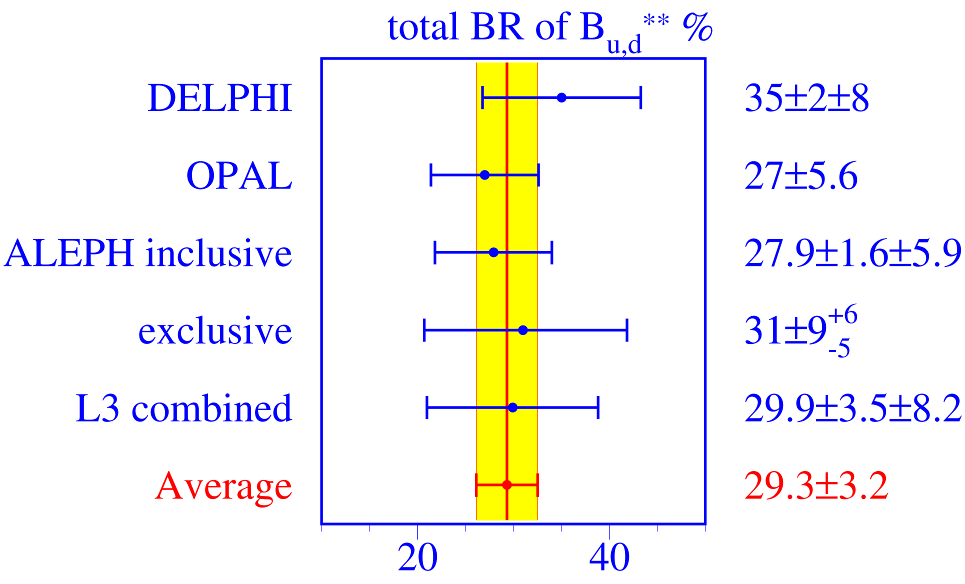

Figure 6.2: *A comparison between the* LEP *measurements of the* $\mathrm{B}^{**}_{\mathrm{u,d}}$ *total production rate* $\frac{\mathrm{B}^{**}_{\mathrm{u,d}}}{\mathrm{B}_{\mathrm{u,d}}}$.

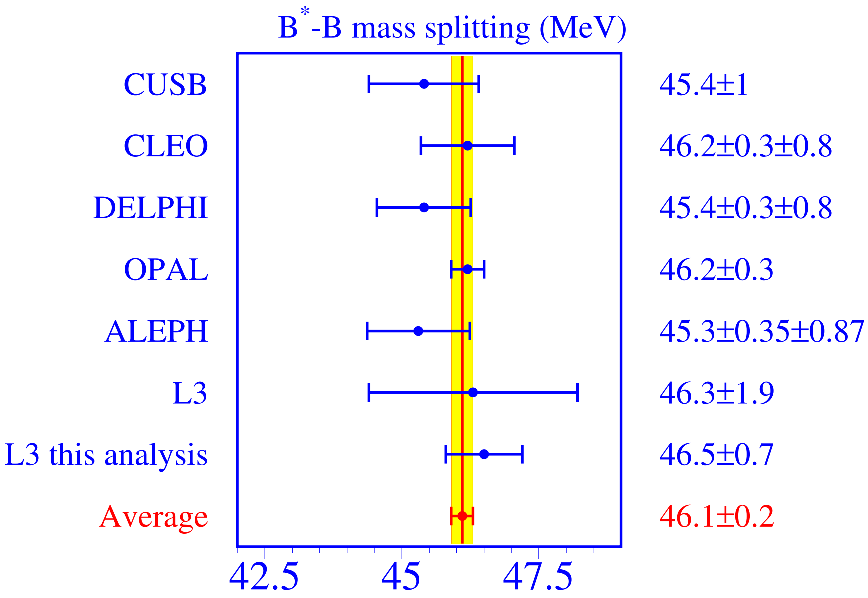

Figure 6.3: *A comparison between the* LEP *measurements of the* B^*-B *mass splitting.*

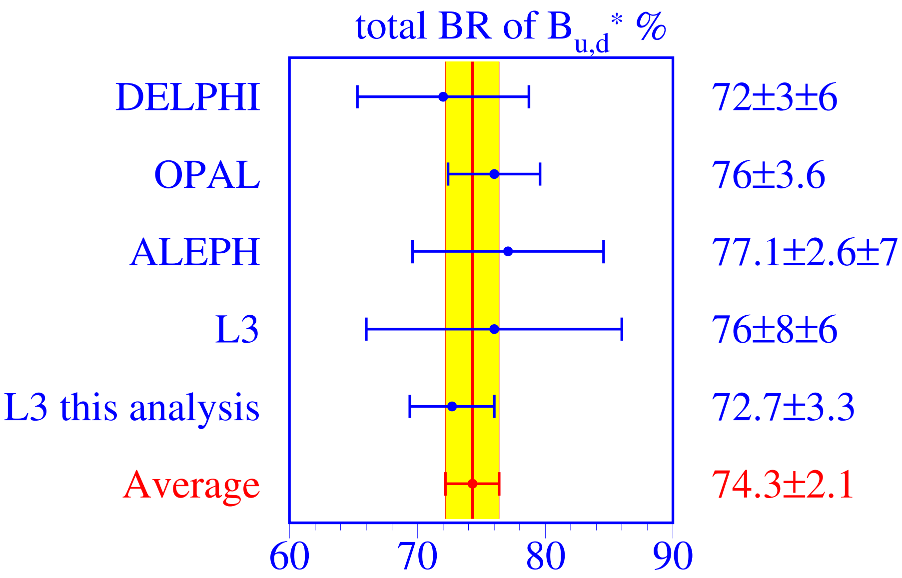

Figure 6.4: *A comparison between the* LEP *measurements of the* B^* *production rate.*

Appendix A

Combination of track probabilities

In this appendix, the various event probabilities given in section 3.2.2 are derived. The product

$$\Pi = \prod_{i=1}^{n} P(|S_i|), \tag{A.1}$$

where P_i is the probability of track i to come from the primary vertex, can be used to determine which event is a B event and which is not. However, this value depends very much on the number of tracks in an event. It is better to use the probability, or actually the confidence level, that an event with no B would have a product of probabilities less than or equal to the observed value of Π, i.e. $C_n(\Pi) = (\text{prob.that}) \prod_{i=1}^{n} x_i < \Pi$, where x_i are uniformly distributed variables representing the possible values for a given track-probability and Π is the product of observed variables of x_i as defined in equation A.1.

Let us start with the simple two-track case. The situation is plotted in figure A.1. The confidence level for two tracks $C_2(P_1P_2)$ is just one minus the (shaded) area inside the hyperbola defined by the equation: $x_1 = P_1P_2/x_2$. This leads to

$$C_2(P_1P_2) = 1 - \int_{\Pi}^{1}\int_{\Pi/x_2}^{1} \delta x_1 \delta x_2 = \Pi\,(1 - \ln\Pi)\,. \tag{A.2}$$

One can extend the above example to more than two tracks, using the fact that

$$\int \frac{\ln^n x}{x} \mathrm{d}x = \frac{1}{n+1} \ln^{n+1} x. \tag{A.3}$$

For n tracks this leads to $C_n(\Pi) = \Pi(1 - \ln\Pi + \frac{1}{2}\ln^2\Pi - \cdots (-)^{n-1}\frac{1}{(n-1)!}\ln^{n-1}\Pi)$. This can be written in a simpler form as:

$$C_n(\Pi) = \Pi \left(\sum_{i=0}^{n-1} \frac{(-\ln\Pi)^i}{i!} \right). \tag{A.4}$$

A more mathematical derivation of this confidence level can be found in [65]. Since this event confidence level is a very small quantity in the case of B-meson decays, the region of interest is expanded by defining the discriminant B_n as: $B_n = -\log C_n$. The efficiency and purity as a function of this event discriminant is plotted in figure A.2

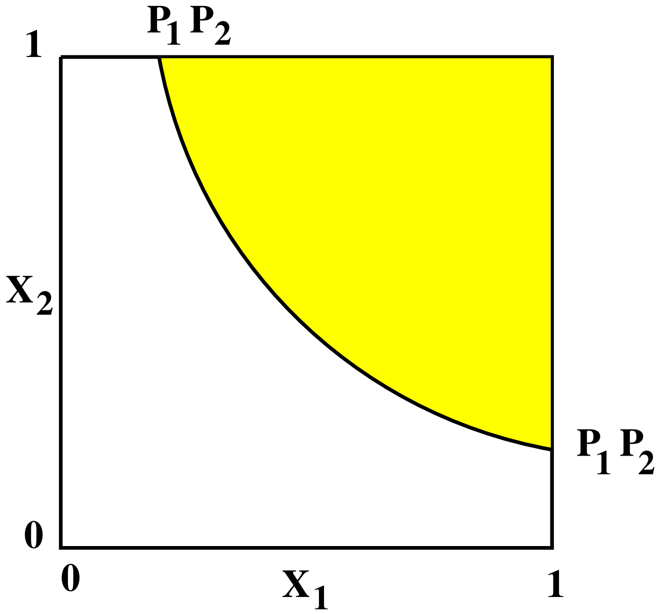

Figure A.1: *Determination of the total probability in the simple two-track case.*

In the confidence level obtained above only tracks with positively signed decay lengths are used. The idea behind this is that tracks with large negatively signed decay lengths cannot be B-decay particles. Low probabilities from the negative side would only add ‘noise’ to the calculation of the event probability. However, knowing the multiplicity can be helpful. This can be seen as follows: If there are more negatively signed tracks, then the confidence level for getting a few tracks with small positive decay lengths is higher. To account for such fluctuations, the probability for negative-decay-length tracks is defined to be unity (negatively-signed tracks come very probably from the primary vertex). In a u,d,s event about half of the tracks should have a negative sign. The confidence level obtained in this way can be written in terms of the previous confidence level obtained in equation A.4:

$$C'_n = \frac{1}{2^n}\sum_{j=1}^{n}\binom{n}{j}C_j = \frac{1}{2^n}\Pi\sum_{j=1}^{n}\binom{n}{j}\sum_{i=0}^{j-1}\frac{-\ln(\Pi)^i}{i!}. \tag{A.5}$$

The efficiency and purity as a function of the event discriminant is plotted in figure A.3. When compared to figure A.2, one can see that the latter confidence level gives better efficiency values for the same purity.

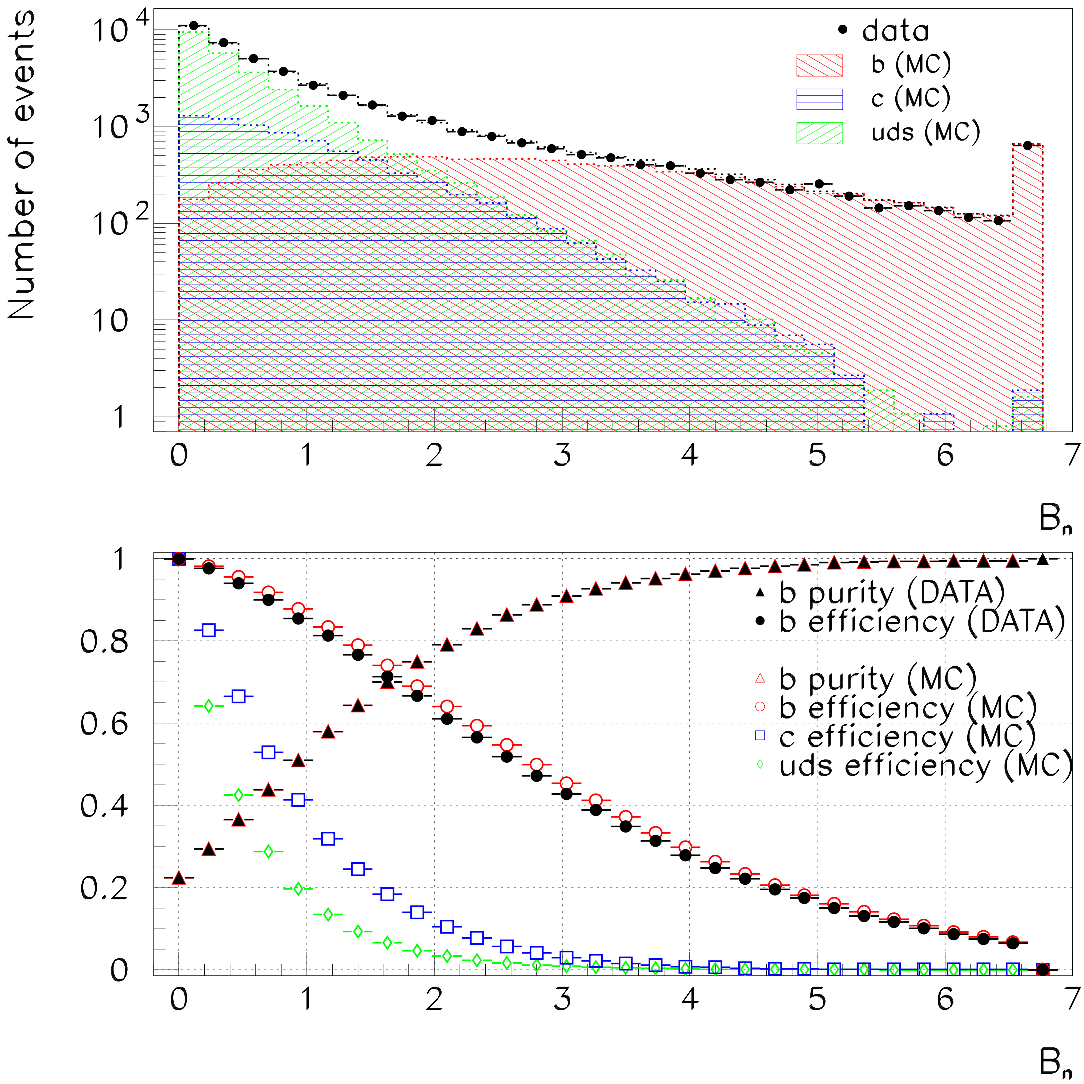

Figure A.2: *The event discriminant distribution is shown in the upper plot for the case that only positively signed tracks were taken into account. The last bin is the overflow bin. The efficiency and purity as function of a cut on the discriminant is shown in the bottom plot.*

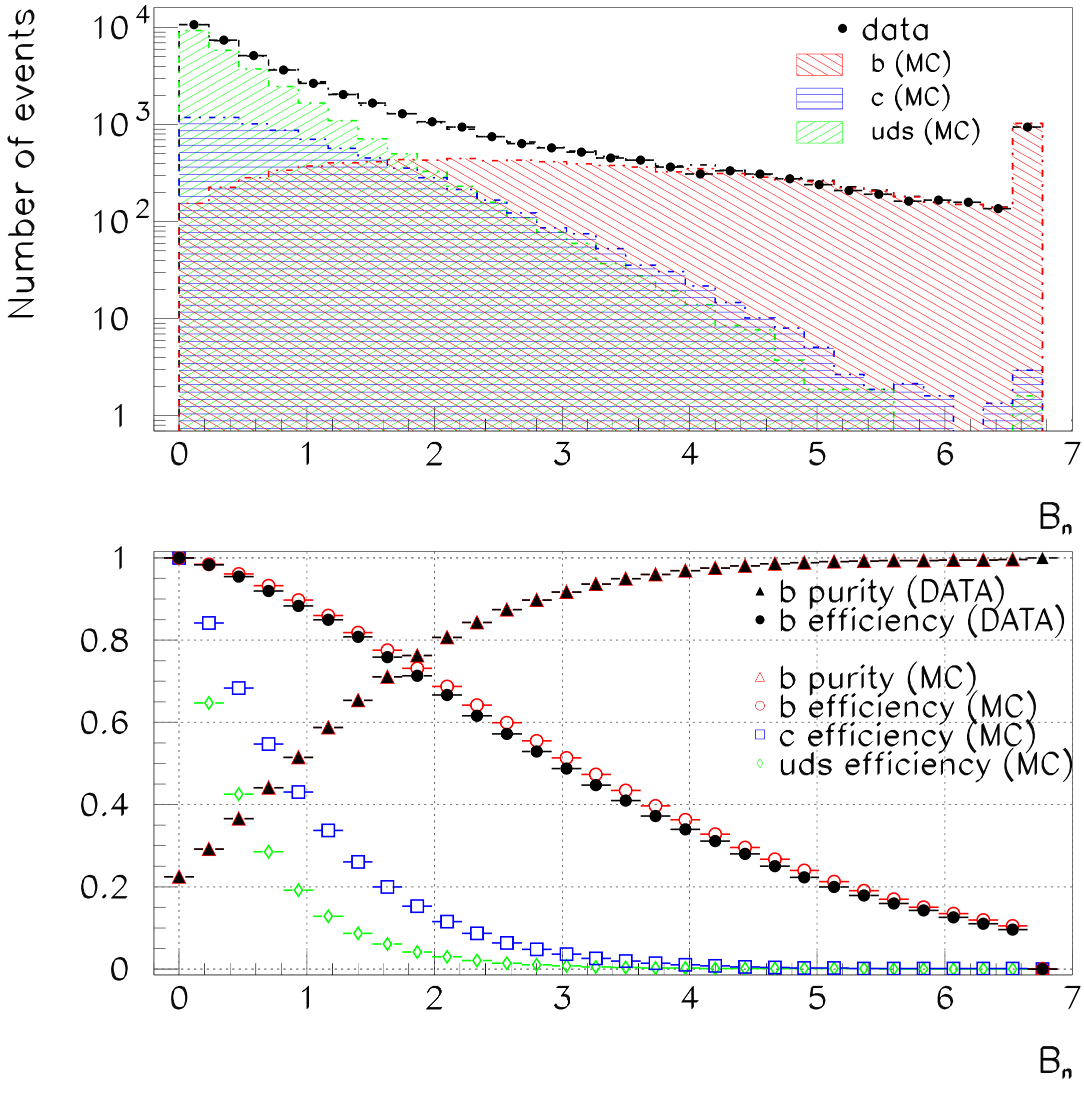

Figure A.3: *The same as figure A.2, but here also negatively signed tracks were taken into account for the calculation of the event discriminant.*

Bibliography

[1] N. Isgur and M.B. Wise, "Heavy Quark Symmetry", pp. 231–282, in B Decays, ed. Sheldon Stone, (World Scientific, Singapore, 1994).

[2] Super-Kamiokande Collab., Y. Fukuda *et al.*, "Study of the atmospheric neutrino flux in the multi-GeV energy range", *Phys. Lett.* **B433** (1998) 9–18.

[3] Super-Kamiokande Collab., Y. Fukuda *et al.*, "Measurement of a small atmospheric ν_μ/ν_e ratio", *Phys. Lett.* **B436** (1998) 3–41.

[4] Particle Data Group: C. Caso *et al.*, *Eur. Phys. J.* **C3** (1998).

[5] D0 Collab., B. Abbott *et al.*, "Direct Measurement of the Top Quark Mass at D0", *Phys. Rev.* **58** (1998) 052001.

[6] CDF Collab., F. Abe *et al.*, "Measurement of the Top Quark Mass", *Phys. Rev. Lett.* **82** (1999) 82–271.

[7] The LEP Collaborations ALEPH, DELPHI, L3, OPAL and the LEP Electroweak Working Group, "A Combination of Preliminary LEP Electroweak Measurements and Constraints on the Standard Model", PPE 95-172, CERN, 1995.

[8] M. Kobayashi and T. Maskawa, "CP-Violation in the Renormalizable Theory of Weak Interactions", *Prog. Theor. Phys.* **Vol. 49** (1973) 652.

[9] M. Neubert, "Heavy Quark Symmetry", *Phys. Rep.* **245** (1994) 259.

[10] Matthias Neubert, in Proc. Effective Theories and Fundamental Interactions, (World Scientific, Singapore, 1997), pp. 98–142.

[11] Jonathan L. Rosner, "P-Wave Mesons with One Heavy Quark", *Comments Nucl. Part. Phys. Comm.* **16** (1986) 109.

[12] Benjamin Grinstein, "Review of Recent Developments in Heavy Quark Theory", HUTP-91/A028, 1991.

[13] Nathan Isgur and Mark B. Wise, "Spectroscopy with Heavy-Quark Symmetry", *Phys. Rev. Lett.* **66** (1991) 1130.

[14] Thomas Mannel, "Review of Heavy Quark Effective Theory", TTP-96-56, 1996, Contribution to the Workshop on Heavy Quarks at Fixed Target, Rheinfals Castle, St. Goar, Germany, October 3-6 1996.

[15] F. Hussain and G. Thompson, "An Introduction to the Heavy Quark Effective Theory", IC/95/15, International Centre for Theoretical Physics, Trieste, Italy, 1995.

[16] Benjamin Grinstein, "Review of Heavy Quark Effective Theory", UCSD/PTH-95-05, 1995, Introductory lectures on heavy quarks and heavy quark effective field theory, August 1995.

[17] Mark B. Wise, "Heavy Flavor Theory: Overview", CALT-68-1901, 1993, Talk given at the Lepton Photon Conference Cornell University, August 1993.

[18] Mark B. Wise, "Combining Chiral and Haevy Quark Symmetries", CALT-68-1860, 1993, Lectures given at CCAST Symposium on Particle Physics at the Fermi Scale, May 27-June 4, 1993.

[19] A.F. Falk, M. Neubert and M.E. Luke, "Strong decays of excited mesons in chiral perturbative theory", *Nucl. Phys.* **B388** (1992) 363.

[20] A.F. Falk and M. Neubert, "Second order power corrections in the heavy quark effective theory.1.Formalism and meson form-factors.2.Baryon form-factors", *Phys. Rev.* **D47** (1993) 2965 and 2982.

[21] P. Ball and V.M. Braun, "Next-to-leading order corrections to meson masses in the heavy quark effective theory", *Phys. Rev.* **D49** (1994) 2472.

[22] V. Eletsky and E. Shuryak, "Dependence of the decay constant of heavy - light pseudoscalar meson on the heavy quark mass", *Phys. Lett.* **B276** (1992) 191.

[23] M. Neubert, "A virial theorem for the kinetic energy of a heavy quark inside hadrons", *Phys. Lett.* **B322** (1994) 419.

[24] Michael Gronau, Alex Nippe and Jonathan L. Rosner, "Method for flavour tagging in neutral B meson decays", *Phys. Rev.* **D47** (1993) 1988.

[25] Estia J. Eichten, Christopher T. Hill and Chris Quigg, "Orbitally Excited Heavy-Light Mesons Revisited", FERMILAB-CONF-94/118-T, 1994.

[26] Estia J. Eichten, Christopher T. Hill and Chris Quigg, "Properties of Orbitally Excited Heavy-Light ($Q\bar{q}$) Mesons", *Phys. Rev. Lett.* **71** (1993) 4116.

[27] Michael Gronau and Jonathan L. Rosner, "Identification of neutral B mesons using correlated hadrons", *Phys. Rev.* **D49** (1993) 255.

[28] D. Elbert, V.O. Galkin and R.N. Faustov, "Mass spectrum of orbitally and radially excited heavy-light mesons in relativistic quark model", *Phys. Rev.* **D57** (1998) 5663.

[29] Nathan Isgur, "Spin-orbit inversion of excited heavy quark mesons", *Phys. Rev.* **D57** (1998) 4041.

[30] CLEO Collab., T. Bergfeld *et al.*, "Observation of D1+(2420) and D2*+(2460)", *Phys. Lett.* **B340** (1994) 194.

[31] CLEO Collab., T. Bergfeld *et al.*, "Production and decay of D0+(2420) and D2*0(2460)", *Phys. Lett.* **B331** (1994) 236.

[32] ARGUS Collab., H. Albrecht *et al.*, "Resonance decomposition of the D*0(2420) through a decay angular analysis", *Phys. Lett.* **B232** (1989) 398.

[33] ARGUS Collab., H. Albrecht *et al.*, "Observation of charged isospin partner of D*0(2459) ", *Phys. Lett.* **B231** (1989) 208.

[34] ARGUS Collab., H. Albrecht *et al.*, "Observation of the D*0(2459) in e+e- annihilation", *Phys. Lett.* **B221** (1988) 422.

[35] DELPHI Collab., P. Abreu *et al.*, "Narrow D^{**} production in c and b jets", Internal Report DELPHI 98-128; CONF 189, 1998, Preliminary results presented at ICHEP'98, Vancouver, BC, Canada, july 23-29 1998.

[36] ALEPH Collab., D. Buskulic *et al.*, "Production of D_1 and D_1^* mesons in hadronic Z decays", Internal Report ALEPH 98-047; CONF 98-021, 1998, Preliminary results presented at ICHEP'98, Vancouver, BC, Canada, july 23-29 1998.

[37] DELPHI Collab., P. Abreu *et al.*, "Observation of Orbitally Excited B Mesons", *Phys. Lett.* **B345** (1995) 598.

[38] OPAL Collab., R. Akers *et al.*, "Observations of $\pi - B$ charge-flavor correlations and resonant $B\pi$ and BK production", *Z. Phys.* **C66** (1995) 19.

[39] ALEPH Collab., D. Buskulic *et al.*, "Production of Excited Beauty States in Z Decays", *Z. Phys.* **C69** (1996) 393.

[40] ALEPH Collab., D. Buskulic *et al.*, "Resonant Structure and Flavour Tagging in the $B\pi^{\pm}$ System Using Fully Reconstructed B Decays", EP 98-017, CERN, 1998.

[41] CDF Collab., "Flavor Tagging, B^{**} Production, and Rare B Decays at CDF ", Internal report, 1998, Preliminary results presented at ICHEP'98, Vancouver, BC, Canada, july 23-29 1998.

[42] DELPHI Collab., P. Abreu *et al.*, "A measurement of D meson production in Z0 hadronic decays", *Z. Phys.* **C59** (1993) 533.

[43] CUSB Collab., Q.W Wu *et al.*, "Measurement of the B^* cross-section at $s^{**}(1/2) = 10.61$ GeV to 10.70 GeV", *Phys. Lett.* **B273** (1991) 177.

[44] CLEO Collab., D.S Akerib *et al.*, "Measurement of the inclusive B^* cross section above the Upsilon(4S)", *Phys. Rev. Lett.* **67** (1991) 1692.

[45] DELPHI Collab., P. Abreu *et al.*, "B^* production in Z decays", *Z. Phys.* **C68** (1995) 353.

[46] OPAL Collab., K. Ackerstoff *et al.*, "B^* production in Z0 decays", *Z. Phys.* **C74** (1997) 413.

[47] ALEPH Collab., D. Buskulic *et al.*, "Production of excited beauty states in Z decays", *Z. Phys.* **C69** (1996) 393.

[48] L3 Collab., M. Acciarri *et al.*, "B^{*} production in Z decays at LEP", *Phys. Lett.* **B345** (1995) 589.

[49] L3 Collab., M. Acciarri *et al.*, (1995), contribution to EPS conference, Brussels EPS95.

[50] Raymond Rosmalen, "A test of QED with $e^{+}e^{-}\rightarrow\gamma\gamma$ at LEP energies", Ph.D. thesis, Univ. of Nijmegen, 1994.

[51] J. Wenniger, "Mesure de paramètres électro-faibles du Z avec la réaction $e^{+}e^{-}\rightarrow e^{+}e^{-}$", Ph.D. thesis, Univ. of Geneva, 1992.

[52] Yu. Galaktionov *et al.*, "The performance of a uranium gas sampling calorimeter", *Nucl. Inst. Meth.* **A251** (1986) 258.

[53] L3 Collab., B. Adeva *et al.*, "Test results of the L3 precision muon detector", *Nucl. Inst. Meth.* **A289** (1990) 335.

[54] L3 Collab., O. Adriani *et al.*, "Results from the L3 experiment at LEP", *Phys. Rep.* **236** (1993) 1.

[55] L3 Collab., M. Acciari *et al.*, "The Silicon Microvertex Detector", *Nucl. Inst. Meth.* **A351** (1994) 300.

[56] L3 SMD Collab., B. Acciari *et al.*, "The Silicon Microvertex Detector", *Nucl. Inst. Meth.* **A360** (1995) 103.

[57] V. Krastev, "Analysis of the spring 1993 SMD metrology data", L3 note 1484, 1993.

[58] L3 -SMD Collaboration, "The L3 Silicon Microvertex Detector", PPE 94-122, CERN, 1994.

[59] Boston University, L3 group, "L3 Radiation Monitor System Data Summary for 1993 and 1994 Runs", L3 note 1709, 1995.

[60] L3 SMD Collab., A. Adam *et al.*, "Test beam results from the prototype L3 silicon microvertex detector", *Nucl. Inst. Meth.* **A344** (1994) 521.

[61] J.Alcaraz, M.I. Josa and J.C. Pinto, "Global Alignment of the L3 Silicon Microvertex Detector", L3 note 1724, 1995.

[62] J.Alcaraz, M.Biasini and M.I. Josa, "The Alignment of the L3 Silicon Microvertex Detector", L3 note, in preperation.

[63] J.Alcaraz, "SZ reconstruction in the L3 detector", L3 note 2318, 1998.

[64] Dimitri Bourilkov, "TEC Calibration with the SMD", L3 note 1870, 1995.

[65] Aaron Dominguez, "Search for Neutral Higgs Bosons in $e^{+}e^{-}$ interactions at cernter-of-mass energies between 130 GeV and 183 GeV", Ph.D. thesis, Univ. of California, San Diego, 1998.

[66] T.Sjöstrand, "PYTHIA 5.6 and JETSET 7.3 Physics and Manual", TH 6488/92, CERN, 1992.

[67] R. Brun *et al.*, "Geant users manual", DD/EE 84-1, CERN, September 1987.

[68] L3 Collab., B. Adeva *et al.*, "Measurement of electroweak parameters from hadronic and leptonic decays of the Z0", *Z. Phys.* **C51** (1991) 179.

[69] R.E. Kalman, *J. Basic Eng.* **83** (1961) 95, K.F. track fit with GEANE was implemented in L3 central tracker by G. Raven.

[70] James G. Branson, Aaron Domingues, Ian Fisk and Gerhard Raven, "The UCSD b tag for 1996", L3 note 2108, 1997.

[71] F. Filthaut, D. Bourilkov and V. Briglevic, "Comparison 1995 L3 vertex data with LEP BOM and QS0 measurements", L3 note 1943, 1996.

[72] J. Sens and P.Vikas, "Reconstruction of the L3 Fill Vertices", L3 note 1027, 1991.

[73] J. Alcaraz, B. Bertuci, M. Chamizo, S. Easo, J. Goldstein, D. Kamrad, M. Maity and J. Rodin., "Measurement of tge Z Branching Fraction into Bottom Quarks Using Double Tag Methods.", L3 note 2114, 1997.

[74] Christopher G. Tully, "Baryon Production in Z Decay", Ph.D. thesis, Princeton University, December 1997.

[75] Yijin Pei, "Photon Identification using a Neural Net", L3 note 1569, 1994.

[76] Scott Stuart Snyder, "Measurement of the Top Quark Mass at D0", Ph.D. thesis, State University of New York at Stony Brook, 1995.

[77] J. Casaus, "Fragmentation Parameter Tuning for JETSET 7.4", L3 note 1946, 1996.

[78] The LEP electroweak Working Group, "Presentaion of LEP Electroweak Heavy Flavour Results for Summer 1994 Conferences", L3 note 1613, 1994.

Summary

Exact predictions are possible in QCD due to the existence of symmetries. An important symmetry is the heavy-quark symmetry. If the quark is sufficiently heavy, its spin and mass (flavour) become irrelevant in the dynamics of the heavy meson containing it. The fact that the spin becomes irrelevant results in degenerate pairs of states that are characterised by the angular momentum of the light degrees of freedom, $j_{\mathrm{q}} = L \pm \frac{1}{2}$, and each state of a degenerate pair is indicated by the total spin of the meson, $\vec{J} = \vec{j}_{\mathrm{q}} + \vec{s}_{\mathrm{Q}}$. In the case of orbitally excited (L=1) heavy mesons, those states are $j_{\mathrm{q}} = \frac{1}{2}$, with total spin J=0:B_0, 1:B_1^*, and $j_{\mathrm{q}} = \frac{3}{2}$, with total spin J=1:B_1, 2:B_2^*. The fact that the mass does not matter is used to make predictions for excited B mesons. Results from the charm and even strange excited systems are used and extrapolated to the beauty system. This results in mass predictions of 5.767 GeV and 5.755 GeV for the $j_{\mathrm{q}} = 3/2$, J_+ and J_- states, respectively. It is not yet possible with this method to predict the mass of the $j_{\mathrm{q}} = 1/2$ states. As the widths the theory predicts 11 MeV for the decay of B_2^* to $\mathrm{B}^*\pi$, 11 MeV for the decay of B_2^* to $\mathrm{B}\pi$ and 17 MeV for the decay of B_1 to $\mathrm{B}^*\pi$. In case the four momenta of the light degrees of freedom are small compared to the heavy-quark mass, it is convenient to adopt an effective theory where the quark mass approaches infinity and the velocity of the quark is fixed. This is the so called Heavy-Quark Effective Theory (HQET).

The analysis described in this thesis 'hunts' for the orbitally excited heavy-quark meson states. Both decay channels $\mathrm{B}_{\mathrm{u,d}}^{**} \to \mathrm{B}^{(*)}\pi^{\pm}$ and $\mathrm{B}_{\mathrm{u,d}}^{**} \to \mathrm{B}^{(*)}\pi^{0}$ are measured. The L3 detector at the electron-positron collider LEP, Geneva, Switzerland, is used. The most important tool for this kind of analysis is good b-tagging. It requires good knowledge of charged particle tracks and their vertices (primary and secondary). The tracking is done in the Time Expansion wire Chamber (TEC) and the Silicon Micro-vertex Detector (SMD), where the SMD provides 4 space points close to the interaction point. The SMD has a point resolution of 10 μm in $r\phi$, $21\mu\mathrm{m} \bigoplus 15\mu\mathrm{m}/\tan\theta$ and $21\mu\mathrm{m} \bigoplus 26\mu\mathrm{m}/\tan\theta$ in rz for the normal and large readout pitch region, respectively. The Distance of Closest Approach (DCA) resolution is 66 μm in hadronic events.

Data taken in 1994 and 1995 are used. The 3D b-tag algorithm of the San Diego group is applied with a cut which gives a b-purity of 82.1 % and an efficiency of 63.8 %. The primary- and secondary-vertex reconstruction takes place in 3D. A cut on the decay-length significance increases the b-purity to 85.5 %.

An estimate of the B-meson direction of flight is obtained by the line connecting the primary vertex to the secondary vertex. With this method, a good resolution is obtained in the $r\phi$ plane, but the sz resolution is rather poor, due to bad tracking performance in that direction. Another estimate for the direction is obtained by a rapidity algorithm, where all particles with a rapidity higher than 1.5 are assumed to be B-decay particles. This algorithm gives also an estimate of the B-meson energy. For the B-meson direction the weighted average is taken of the SV-PV and rapidity method. The angular resolution is fitted with a double Gaussian. The width of the first Gaussian of the θ distribution is 21.4 mrad and that of the ϕ distribution is 16.7 mrad, with around 50 % of the events in the first Gaussian. According to MC studies, about the same numbers are obtained for the signal-to-noise ratio and signal resolution when only the rapidity algorithm is used. The results obtained in this way are used to determine the contribution to the systematic error due to the choice of the reconstruction algorithm. To obtain the B energy the rapidity method is used together with a centre-of-mass constraint. An energy resolution of 2-4 GeV is obtained.

Charged pions with good *sz* information are used, with, furthermore, a probability to come from the primary vertex larger than 15 % and a transverse momentum with respect to the B-meson direction larger than 130 MeV. Only the most energetic pion in the jet is chosen, since most $B^{**}_{u,d}$ pions are the most energetic ones in the jet. The $B\pi$ invariant mass distribution is used to find an enhancement above the background obtained from MC. The enhancement is fitted with a single Gaussian. The $B^{**}_{u,d}$ mass obtained is (5.712 $\pm$ 0.010 + 0.034 -0.023) GeV, the width (0.079 $\pm$ 0.006 + 0.015 - 0.016) GeV and 2926 $\pm$ 213 $B^{**}_{u,d}$ decays are measured above the background. This results in a relative production rate $\frac{B^{**}_{u,d}}{\text{bjet}}$ of (14.8 $\pm$ 1.2 + 3.5 - 3.0) %. The results of the charged-pion channel compare well to the results obtained by the other LEP experiments.

After a photon selection, neutral pions are formed of pairs of photons with a reconstructed mass within 3 σ of the real π^0 mass and a probability to come from the primary vertex larger than 1 %. The reconstructed pions are required to have an energy larger than 1 GeV. The $B\pi^0$ enhancement is fitted with a single Gaussian. The $B^{**}_{u,d}$ mass obtained is (5.604 $\pm$ 0.019 + 0.041 -0.048) GeV, the width (0.082 $\pm$ 0.026 + 0.045 - 0.051) GeV and 527 $\pm$ 156 $B^{**}_{u,d}$ decays are measured above the background. This results in a relative production rate $\frac{B^{**}_{u,d}}{\text{bjet}}$ of (8.9 $\pm$ 2.5 + 5.5 - 5.7) %.

The $B^{**}_{u,d}$-mass result obtained from the neutral-pion channel differs 2.3 standard deviations from the $B^{**}_{u,d}$ mass results obtained from the charged-pion channel. The widths of both channels are compatible. The ratio of the production rates of the neutral- and charged-pion channels of (0.60 $\pm$ 0.18 $\pm$ 0.40) is in good agreement with the isospin-symmetry expectation of 0.5. Combining the neutral and charged pion results, a total $B^{**}_{u,d}$ production rate BR($b \to B^{**}_{u,d} \to B\pi$) of (23.7 $\pm$ 2.8 $\pm$ 6.5) % is obtained. When it is taken into account that about 10 % of the b-events are baryons and about 12 % are B_s, a ratio $\frac{BR(b \to B^{**}_{u,d} \to B\pi)}{BR(b \to B_{u,d})}$ of (29.9 $\pm$ 3.5 $\pm$ 8.2) % is obtained. The result compares well with the results obtained by other experiments.

As a completion of the excited beauty meson analysis and a check of the B meson reconstruction, the B^* signal is measured. A mass splitting of (46.5 $\pm$ 0.7) MeV and a relative production rate of (72.7 $\pm$ 3.3) % is obtained. This is consistent with former results of L3 and other experiments.

Samenvatting

In QCD zijn nauwkeurige voorspellingen mogelijk dankzij het bestaan van symmetrieen. Een belangrijke symmetrie is de zware-quark symmetrie. Als het quark voldoende zwaar is, zijn de spin en de massa (soort) van het quark niet meer van belang voor de dynamica van het zware meson dat dit quark bevat. Het feit dat de spin er niet meer toedoet resulteert in een gedegenereerd paar van toestanden dat gekarakteriseerd wordt door het hoek momentum van de lichte quarks, $j_{\rm q} = L \pm \frac{1}{2}$, en elke afzonderlijke toestand van het gedegenereerde paar kan aangeduid worden met de totale spin van die toestand, $\vec{J} = \vec{j}_{\rm q} + \vec{s}_{\rm Q}$. In het geval van baan aangeslagen (L=1) zware mesonen zijn deze toestanden, $j_{\rm q} = \frac{1}{2}$, met totale spin J=0:$\rm B_0$, 1:$\rm B_1^*$, en $j_{\rm q} = \frac{3}{2}$, met totale spin J=1:$\rm B_1$, 2:$\rm B_2^*$. Het feit dat de massa niet van belang is, wordt gebruikt om voorspellingen te doen voor aangeslagen B mesonen. Resultaten van het (aangeslagen) 'charm' syteem en zelfs van het (aangeslagen) 'strange' systeem worden geëxtrapoleerd naar het 'beauty' systeem. Dit resulteert in een massa voorspelling van 5.767 GeV and 5.755 GeV voor de $j_{\rm q} = 3/2$, J_+ en J_- toestanden, respectievelijk. Het is (nog) niet mogelijk om op deze manier de massa van de $j_{\rm q} = 1/2$ toestanden te voorspellen. Voor de breedte voorspelt de theorie 11 MeV voor het verval van $\rm B_2^*$ naar $\rm B^*\pi$, 11 MeV voor het verval van $\rm B_2^*$ naar $\rm B\pi$ en 17 MeV voor het verval van $\rm B_1$ naar $\rm B^*\pi$. Als de momenta van de lichte quarks klein zijn vergeleken met de zware-quark massa, is het gemakkelijker om over te gaan naar een effectieve theorie waarin de quark massa naar oneindig gaat en de snelheid van het quark een vast gegeven is. Dit is dan de zogenaamde zware-quark effectieve theorie (HQET).

De analyse die in dit proefschrift wordt beschreven, 'jaagt' op baan aangeslagen zware-quark meson toestanden. De L3 detector, gelegen bij de electron-positron versneller LEP, Geneve, Zwitserland, wordt gebruikt om beide vervals kanalen $\rm B_{u,d}^{**} \to B^{(*)}\pi^{\pm}$ en $\rm B_{u,d}^{**} \to B^{(*)}\pi^{0}$ te meten. Het belangrijkste gereedschap voor dit soort analyses is de b-identificatie. Dit vraagt goede kennis van sporen van geladen deeltjes en hun (primaire en secundaire) vertices. De reconstructie van de sporen is gedaan met de 'Time Expansion wire Chamber' (TEC) en de 'Silicon Micro-vertex Detector' (SMD), waarbij de SMD 4 3D punten dicht bij het electron-positron interactie punt levert. De SMD heeft een punt resolutie van 10 μm in $r\phi$, $21\mu{\rm m} \bigoplus 15\mu{\rm m}/\tan\theta$ en $21\mu{\rm m} \bigoplus 26\mu{\rm m}/\tan\theta$ in rz voor de gebieden met de normale en de grote uitlees afstand, respectievelijk. De 'Distance of Closest Approach' (DCA) resolutie is 66 μm voor hadronische events.

Dat genomen in 1994 en 1995 is gebruikt. Het 3D b-identificatie algoritme van de San Diego groep is toegepast met een snede die een b-puurheid geeft van 82.6 % en een efficiëntie van 63.8 %. De reconstructie van de primaire en secondaire vertex vindt ook plaats in 3D. Door een snede op de vervals lengte significantie neemt de b-puurheid toe tot 85.5 %.

Een schatting van de B-meson richting wordt verkregen door een lijn die het interactie punt (PV) en het b-vervalspunt (SV) met elkaar verbindt. Op deze manier wordt er een goede resolutie verkregen in het $r\phi$ vlak, maar de sz resolutie is slecht doordat de reconstructie van sporen in die richting slecht is. Een andere schatting voor de richting wordt verkregen door het rapiditeits algoritme, waarbij wordt aangenomen dat deeltjes met een rapiditeit groter dan 1.5 b-vervals deeltjes zijn. Dit algoritme geeft ook een schatting van de B meson energie. Voor de richting van het B meson wordt het gewogen gemiddelde genomen van de SV-PV en de rapiditeits methode. De hoek resolutie wordt gefit met een dubbele Gaussische functie. De breedte van de eerste Gauss van de θ verdeling is 21.4 mrad en dat van de ϕ verdeling is 16.7 mrad, waarbij rond de 50% van de events zich in de eerste Gauss bevinden. Volgens Monte-Carlo studies levert het gebruik van alleen het rapiditeits algoritme ongeveer dezelfde waardes voor de signaal-over-ruis verhuiding en de signaal resolutie. De resultaten die op deze manier verkregen worden dienen als schatting voor de systematische fout ten gevolge van de keuze van de B-reconstructie methode. Het rapiditeits algorithme wordt samen met een massa centrum beperking gebruikt om de B energie te bepalen. Hiermee wordt een energie resolutie van 2-4 GeV verkregen.

Geladen pionen met goede sz informatie worden gebruikt, die verder een waarschijnlijkheid hebben die groter is dan 15% om van de PV te komen en een momentum component loodrecht op de B-meson richting groter dan 130 MeV. Alleen het meest energetisch pion in de jet wordt gekozen, omdat de meeste $B^{**}_{u,d}$ pionen de meest energetische pionen zijn in de jet. De $B\pi$ invariante massa verdeling wordt gebruikt om een overschot van events boven de MC achtergrond te vinden. Dit overschot wordt gefit met een enkele Gauss. De verkregen $B^{**}_{u,d}$ massa is (5.712 $\pm$ 0.010 + 0.034 -0.023) GeV, de breedte (0.079 $\pm$ 0.006 + 0.015 - 0.016) GeV en 2926 $\pm$ 213 $B^{**}_{u,d}$ vervallen worden gemeten boven de achtergrond. Dit resulteert in een relatieve productie verhouding $\frac{B^{**}_{u,d}}{bjet}$ van (14.8 $\pm$ 1.2 + 3.5 - 3.0) %. De resultaten van het geladen pion kanaal komen goed overeen met de resultaten die door de andere LEP experimenten behaald zijn.

Na een foton selectie, worden neutrale pionen gevormd van paren fotonen die een gereconstrueerde massa opleveren die binnen 3 σ gelijk is aan de π^0 massa en die een waarschijnlijkheid hebben groter da 1% om van de PV af te komen. De gereconstrueerde pionen moeten een energie groter dan 1 GeV bezitten. De verkregen $B^{**}_{u,d}$ massa is (5.604 $\pm$ 0.019 + 0.041 -0.048) GeV, de breedte (0.082 $\pm$ 0.026 + 0.045 - 0.051) GeV en 527 $\pm$ 156 $B^{**}_{u,d}$ vervallen worden gemeten boven de achtergrond. Dit resulteert in een relatieve productie verhouding $\frac{B^{**}_{u,d}}{bjet}$ van (8.9 $\pm$ 2.5 + 5.5 - 5.7) %.

Het $B^{**}_{u,d}$-massa resultaat dat is verkregen in het neutrale-pion kanaal verschilt 2.3 standaard afwijkingen van de $B^{**}_{u,d}$-mass resultaat dat is verkregen in het geladen-pion kanaal. De breedtes van beide kanalen komen goed overeen. De verhouding van de productie verhoudingen van het neutrale- en geladen kanaal van (0.60 $\pm$ 0.18 $\pm$ 0.40) komt goed overeen met de isospin symmetrie verwachting van 0.5. Wanneer de geladen en neutrale pion resultaten gecombineerd worden, wordt een totale productie verhouding BR($b \rightarrow B\pi$) van (23.7 $\pm$ 2.8 $\pm$ 6.5) % verkregen. Als wordt aangenomen dat ongeveer 10% van de b-events baryons zijn en 12% B_s dan wordt een verhouding $\frac{BR(b\rightarrow B^{**}_{u,d}\rightarrow B\pi)}{BR(b\rightarrow B_{u,d})}$ van (29.9 $\pm$ 3.5 $\pm$ 8.2) % verkregen. Dit resultaat komt goed overeen met de resultaten die door andere experimenten behaald zijn.

Als voltooing van de aangeslagen 'beauty' meson analyse en controle van de B-meson reconstructie, wordt het B^* signaal gemeten. Een massa verschil van (46.5 $\pm$ 0.7) MeV en een relatieve productie verhouding van (72.2 $\pm$ 3.3) % wordt verkregen. Dit komt overeen met eerdere resultaten van L3 en andere experimenten.

Dankwoord

Zonder de medewerking van veel mensen, zowel op persoonlijk vlak als ook op het vakgebied, zou dit proefschrift niet geschreven zijn. Ik zou bij deze graag iedereen willen bedanken en de hieronder genoemde personen in het bijzonder.
Allereerst wil ik mijn promotor prof. E.W. Kittel bedanken zonder wiens kritische blik dit proefschrift niet tot stand was gekomen. I want to thank the whole SMD group, among others Martin Pohl, Juan Alcaraz, Valeri Andreev, Giovanni Passaleva, Rudi Leiste, Hans Tuchscherer and Nicolas Produit, without whose work on the hardware and software this thesis could not have been written, for their pleasant cooperation. Also my thanks to the San Diego group for their btag stuff that considerably improved the results described in this thesis. I also like to thank Chris Tully for his work on the BGO and especailly the photon selection. This made it also possible to study the neutral pion channel. Many thanks to Steve Goldfarb for his discussions and advise on this subject.
De tijd die ik op CERN heb doorgebracht was zeer aangenaam. Hiervoor wil ik allereerst Marcel en Esther Merk bedanken die mij vanaf de eerste dag helemaal thuis hebben laten voelen in St. Genis Pouilly. Verder zorgden de Nederlandse AIO's en OIO's die op hetzelfde moment op CERN waren, Alex Buytenhuijs, Wim van Rossum en later ook Albert van Mil en Erik Visser, alsmede ook Frank Filthaut en Gerhard Raven, voor gezellige lunchpauzes en (veel) bioscoop bezoek. In the lunch and cinema group also Aaron Domingues, Ian Fisk, Chris Tully and Joel Goldstein, thanks to whom I already knew every scene of the 'Holy grail' before I saw it on video, and Jayant Shukla and Wenwen Lu, participated. Special thanks to Wenwen and Jay for their friendship and introduction to real Chinese and Indian food.
Tasja wil ik graag bedanken voor haar vriendschap tijdens mijn verblijf op en later bezoeken aan CERN en de noodzakelijke afleiding van het werk. Mijn bezoeken aan CERN waren ook gezellig dankzij de aanwezigheid van Sandra Muijs, Daniel van Dierendonck, Ann van Lysbetten, Ivo van Vulpen en Martijn Mulders, met wie ik ook voor het eerst (en laatst?) heb wildwater gevaren.
Je voudrais remerçier l'equipe de volley 'Paquis' pour les lundi soirs sportifs. Cela offrait la possibilité de se relaxer et d' étre loin du CERN et de la physique des particules elementaires pour un moment. Aussi mon français s'est amélioré. Maintenant que je suis revenu aux Pays-Bas et la langue de Française est malheureusement vite oubliée. Special thanks to Matthias Schroder and Andreas Morsch for giving me rides to the trainingevenings and tournaments.
Terug in Nijmegen zijn er veel mensen die gezorgd hebben voor de broodnodige gezelligheid op en naast het werk. Annelies Oosterhof, Marjo van Wees, Erna Dikmans en Martine Schout wil ik bedanken voor de gezelligheid op de afdeling en de dagelijkse thee met (minder dagelijkse) koekjes en snoepjes. Herve Kuyten, Rob Bergman , Michiel Sanders, Jorn van Dalen, Miranda van Iersel, Bert Petersen, Henric Wilkens, Dominique Mangeol, Wes Metzger, Jaap Schotanus, Peter 'taart!' Klok, Charles Timmermans en de rest van de afdeling bedankt voor

de gezellige vrijdagmiddagen die soms gepaard gingen met taart en veel lol en niet te vergeten de zeer gedenkwaardige ‘dagjes uit’ met de afdeling.
Natuurlijk wil ik trouwe vrienden niet vergeten. Marianne Houbiers, Jeike Wallinga en Renee Heller wil ik bedanken voor hun vriendschap, de gezellige etentjes samen en (natuurkundige en maatschappelijke) discussies.
En niet te vergeten de IBB 81 meiden, Manuela de Laat, Ingrid Pieters, Lydia Pelt en Yvonne Wijnbergen die altijd in waren voor gezellig kwebbelen, het spuien van (goede/wijze) raad en de laatste ook voor het ‘koppelen’.
Mijn ouders en oma, Rosa en Matthé wil ik bedanken voor hun continue steun tijdens mijn promotie onderzoek.
En tot slot wil ik Gerhard bedanken, mijn steun en toeverlaat, voor zijn liefde en geduld.

Cirriculum Vitae

De schrijfster van dit proefschrift werd geboren op 25 maart 1971 te Den Helder. Gedurende de periode 1983 tot 1989 volgde zij de middelare school opleiding aan het Nieuwe Diep te Den Helder, welke zij afronde met het behalen van het VWO diploma.

In 1989 begon ze haar studie natuurkunde aan de Rijksuniversiteit Utrecht. Het propedeutisch examen werd behaald in 1991. Tijdens de eindfase was ze werkzaam op de afdeling SubAtomaire Fysica, waar een bijdrage geleverd werd aan het G_m^n onderzoek. Dit resulteerde in een scriptie getiteld: ’ Absolute Neutron Detection Efficiency Calibration’.

In 1994 begon ze, in dienst van de stichting Fundamenteel Onderzoek der Materie (FOM) en verbonden aan de Katholieke Universiteit Nijmegen, haar aanstelling als onderzoeker in opleiding. In het kader daarvan was zij een jaar en negen maanden werkzaam in de European Organisation for Nuclear Research (CERN) te Genève. Ze leverde daar een bijdrage aan de studie van het *b* quark, met name de aangeslagen toestand, in het L3 experiment opgesteld aan de Large Electron Positron collider (LEP). Dat onderzoek heeft geleid tot dit proefschrift onder begeleiding van prof. E.W. Kittel.